

# **Safety in Mines Research Advisory Committee**

## **Final Report (Revised)**

# **Mine layout, geological features and seismic hazard**

**Main Authors: G van Aswegen and A J Mendecki**

**Main Co-authors:** R Lachenicht  
A H Dzhafarov  
G Hofmann  
S Radu, *ISS Pacific*  
M Eneva, *University of Toronto, Canada*  
M Sciocatti  
G Kotze

**Research agency** : ISS International Limited  
**Project number** : GAP 303  
**Project duration** : 1 January 1996 – 31 December 1998  
**Report date** : January 1999

# Executive summary

**Introduction:** There are a number of factors that correlate positively with the potential for large(r) dynamic rockmass instability in response to deep level mining, e.g.:

- tectonic stresses, depth, mechanical strength of intact rock,
- the existence and the frequency of intermediate and larger geological features, specifically when parallel to the excavation faces and/or when their shear strength is comparable to shear stresses close to excavations,
- longwall type mine layout (as opposed to scatter mining layouts) without regional support (stabilising pillars, backfill) and with straight face shapes,
- concentrated mining, i.e. the proximity of a number of active faces excavating a large volume of rock,
- volume mined to date,
- mining remnants against seismically active structures,
- rate of face advance, etc.

Such observations, if correct, provide important guidelines for the design process but, since the influence of the particular factors cannot be quantified, it does not constitute the design methodology.

**Stiffness and hazard:** The following unique observations made during this project contributed towards the development of an improved mine layout design methodology and the new interpretation of seismic data to confirm the design as mining progresses.

1. The d-value, determining the slope of the log E vs log M, called here E-M relation, tends to increase with the system stiffness. The E-M plot for the stiff system does not extend far into the large(r) events range until the stiffness is degraded and the d-value drops - Figure 1. For a given slope an increase in c-value of the E-M relation reflects an increase in stress.
2. The power exponent of the size distribution of seismic events, called also the b-value of the Gutenberg-Richter relation, positively correlates with the stiffness of the system, i.e. the stiffer the system the higher the b-value and the lower the size distribution hazard - Figure 1. This observation does not contradict reports on decreasing b-value with increasing stress, since there is a general loss of stiffness with increasing stress during a strain hardening regime. In the absence of a significant tectonic stress, intermediate and large seismic events usually occur after considerable mining has taken place in the area, degrading the stiffness of the system.
3. In general stiffer systems/layouts are characterised by lower  $m_{max}$  but by a time-of-day distribution with larger statistical dispersion in relation to the time of blasting, thus they are less time-predictable, while softer systems have larger  $m_{max}$  but they trigger or induce most events during the few hours after blasting - Figure 1.

**Stiffness and stability:** A system is defined as a volume of rockmass with its geological features, mining excavations and associated damage due to inelastic deformation. Stiffness, being stress and strain related, as opposed to stress based ESS, measures the ability of a system to resist deformation with increasing stresses. An instability will occur when the overall stiffness of the damaged zones(s), including excavations, exceeds the unloading stiffness of the surrounding rockmass or when the damage zone(s) hardens at a lower rate than the ambient rock, i.e. relative softening.

**Stiffness and layout:** It is the link: stiffness - potential for instability - the nature of instability - size distribution hazard - time distribution hazard, that make the stiffness based design methodology an attractive proposition. In general for the same extraction ratio, the higher the stiffness and the lower its spatial and temporal variance within the system, the better the layout.

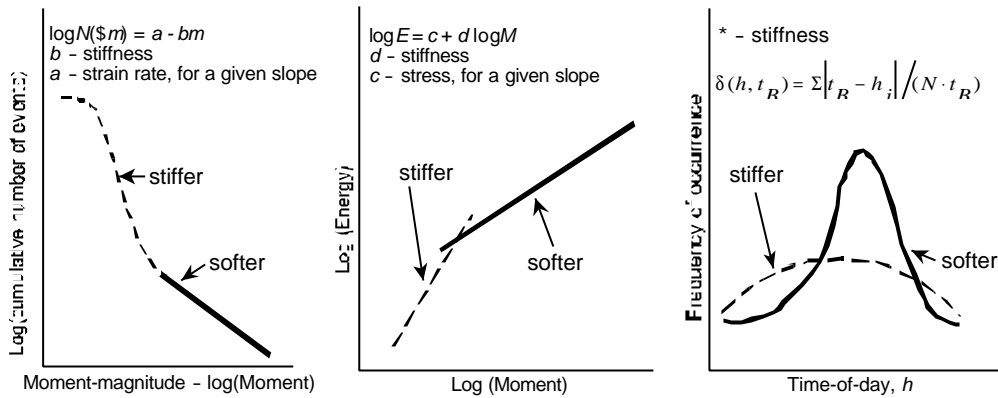


**Figure 1** An illustration of a cumulative frequency-magnitude plot of a mixed data set over a limited period of time (left). Events associated with a stiffer system (broken line) and with a softer system (solid line) frequently have different slopes. On a log Energy vs log Moment plot (centre) the same applies. Intermediate and larger events associated with softer systems tend to occur within a few hours of blasting time,  $t_b$ , while a stiffer system responds moderately but with larger statistical dispersion, as measured by the normalised standard deviation  $d$ , (right).

**Stiffness monitoring:** As mining progresses the overall stiffness of the system is being degraded, increasing the potential for larger instabilities specifically those associated with geological structures. New parameters are offered to monitor the rate of stiffness degradation:

1. A sum of Lyapunov exponents,  $E_8$ , of the embedded time series of seismic radiated energies or seismic moments. It is considered the most comprehensive measure, since it reconstructs the dimension, i.e. a number of degrees of freedom, and the divergence of motion trajectories in those directions. The more negative the  $E_8$ , the higher the rate of relaxation or drop in system stiffness.
2. Seismic stiffness modulus,  $K_s$ , that correlates positively with the system stiffness.

New ways of spatio-temporal presentation of data, conducive to integration with results of numerical modelling are also proposed:

1. Differential maps - 2D contour lines or 3D surfaces of equal percentage difference in a given observed parameter between two periods of time overlaid on a similar map of a respective modelled parameter.
2. Local clustering,  $C$ , of a given seismic parameter,  $S$ , in space of an average distance between consecutive events,  $\bar{X}$ , and in time of an average time between events,  $\bar{t}$ :  

$$C(\Omega, \bar{X}, \bar{t}) = \Omega / (\bar{X})(\bar{t})$$
, for stiffness degradation monitoring recommended  $\Omega = K_s$  or  $D_s$ .

**Seismic hazard:** It is a practice in South African gold mines to measure seismic hazard by the average recurrence time of larger events derived directly from observations or from the extrapolation of the Gutenberg-Richter relation. However it has been shown that seismic hazard derived from the size distribution of seismic events may not be adequate to quantify and to manage the exposure to seismicity, due to the differences in time of day distribution of intermediate and large events associated with different mining scenarios. Seismic safety exposure at a given hour of day can then be estimated by the product of the average frequency of potentially damaging events and the average number of people exposed at that time.

The highest threat to safety and mine infrastructure however comes from strong ground motion caused by the largest seismic events, the frequency and the location of which can not be determined by statistics. A procedure has been developed to produce iso-surfaces of the maximum near and intermediate field ground velocities from large seismic events (Figure 2), originating at locations determined by

1. the delineation of loaded asperities through the analysis of seismicity and

II. numerical modelling taking into account historical seismic deformation.

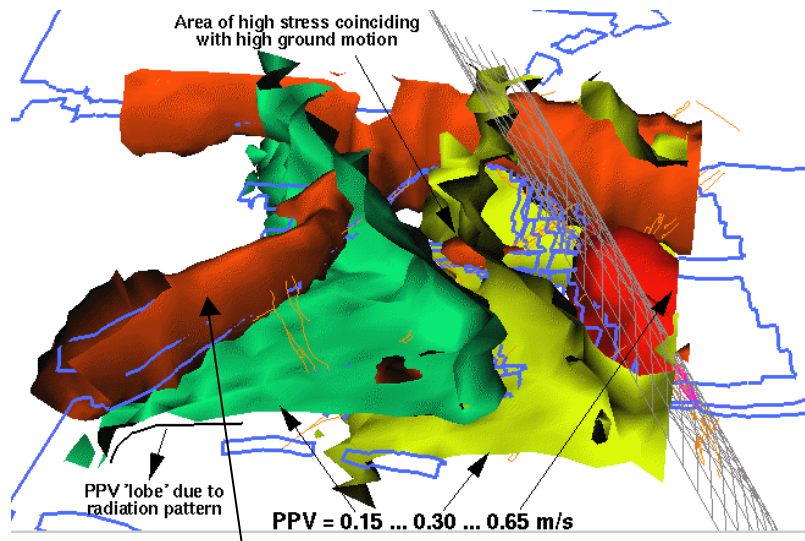


**Figure 2** Example of a 3D ground motion hazard map (iso-surfaces of different values of PPV) combined with modelled stress values. The modelled stress contours is also shown in the form of iso-surfaces.

**Other Outputs:** During the course of this project a number of useful procedures and research tools have been developed in pursuit of the objectives:

1. Apparent stress level – This is a convenient measure of the level of stress, and found to increase with depth.
2. VGM – Volume of ground motion, i.e. the probability of having damaging events expressed as an integrated number, namely the volume of rock likely to be sheared at a damaging velocity.
3. Hazard magnitude – Another simplification of the expression of seismic hazard, hazard magnitude is the sum of seismic moment and/or energy derived from the Gutenberg-Richter relation and expressed as a single number.
4. Test for spatial localisation of seismic activity quantified by its obliqueness.
5. Test for stochastic bifurcation by calculating statistical dispersion of histogrammed data in a sliding window.
6. An algorithm to discriminate seismicity associated with production blasts and to calculate the daily blast ratios.

## **Acknowledgements**

The contents of the report is, for most part, the result of research sponsored by SIMRAC – this financial support is highly appreciated. The research done at ISS INTERNATIONAL on mine seismicity would not be possible without the co-operation of rock engineering staff and mine seismologists at the different mines. We are especially grateful to Rock Engineering and Mine Seismology staff at AngloGold and Goldfields as well as staff from the Geology Departments of the Free State and Vaal River Operations of AngloGold. We were kindly assisted and encouraged during many informal discussions.

# Table of contents

Executive summary.....	ii
Acknowledgements .....	v
Table of contents .....	vi
List of figures .....	viii
List of tables.....	xi
Glossary of seismic terms .....	xii
<b>1. The geological structure .....</b>	<b>1</b>
<b>1.1. Structural fabric of rock.....</b>	<b>1</b>
<b>1.2. The size distribution of discontinuities .....</b>	<b>1</b>
1.2.1. Application to fault size distribution.....	2
1.2.2. Application to fault populations in mines .....	2
1.2.3. Comparison with seismic hazard related parameters .....	3
<b>2. Rockmass stability and system stiffness.....</b>	<b>6</b>
<b>2.1. Stability of deformation and stability of a system – static considerations .....</b>	<b>6</b>
<b>2.2. Dynamic analysis of stability – phase space .....</b>	<b>8</b>
<b>2.3. Phase space reconstruction and Lyapunov exponents .....</b>	<b>11</b>
<b>2.4. Spatial and temporal gradients.....</b>	<b>12</b>
<b>2.5. Differential maps .....</b>	<b>13</b>
<b>3. System stiffness and seismic hazard .....</b>	<b>13</b>
<b>3.1. Size distribution hazard.....</b>	<b>13</b>
<b>3.2. Seismic hazard and system stiffness.....</b>	<b>16</b>
<b>3.3. Time of day distribution hazard .....</b>	<b>22</b>
<b>3.4. System stiffness, <i>E-M</i> relations and seismic hazard.....</b>	<b>22</b>
<b>4. Modelled system stiffness – Theoretical concepts .....</b>	<b>24</b>
<b>4.1. Seismic Monitoring and System Stiffness.....</b>	<b>24</b>
4.1.1. Observations .....	24
4.1.2. Interpretation.....	24
4.1.3. Hypotheses .....	25
4.1.3.1. Hypothesis 1 - Energy-Moment Ratio.....	25
4.1.3.2. Hypothesis 2 - Energy-Moment Relation Slope .....	26
4.1.4. Applied Analysis - Structure Stiffness .....	27
4.1.5. Hypothesis 3 – Applied Structure Stability Analysis .....	27
<b>4.2. Modelled System Stiffness .....</b>	<b>28</b>
4.2.1. Instability and System Stiffness – Theoretical Overview.....	28
4.2.2. Applied System Stiffness – Large Geological Discontinuities .....	29
4.2.3. Numerical Methods .....	32
<b>4.3. Applied Modelled System Stiffness - Numerical Experiments .....</b>	<b>33</b>
4.3.1. Energy-Moment Ratio and Energy-Moment Relation Slope .....	33
4.3.1.1. Experiment 1 .....	33
4.3.1.2. Experiment 2 .....	36
4.3.1.3. Experiment 3 .....	39
4.3.2. Structure Stability Analysis .....	43
4.3.2.1. Experiment 1 .....	43
4.3.2.2. Experiment 2 .....	45
4.3.2.3. Experiment 3 .....	46
<b>4.4. Conclusions.....</b>	<b>47</b>
<b>5. Mine layout design methodology .....</b>	<b>48</b>
<b>6. Strong ground motion hazard modelling .....</b>	<b>53</b>
<b>6.1. Introduction .....</b>	<b>53</b>
<b>6.2. Slip velocity in a seismic source .....</b>	<b>54</b>
6.2.1. Distribution of displacement in a source.....	54
6.2.2. Static circular-crack model.....	55
6.2.3. Asperity model.....	55
6.2.4. Asperity model vs. circular crack.....	58

<b>6.3.</b>	<b>Analysis of recorded seismic events .....</b>	<b>58</b>
6.3.1.	Slip velocity databases.....	58
6.3.2.	Relationship between stress drop and slip velocity.....	59
<b>6.4.</b>	<b>VMAP event simulations .....</b>	<b>63</b>
6.4.1.	Simulation of PPV of a large event on a fault.....	63
6.4.2.	Simulation of event in an actual mining situation.....	64
<b>6.5.</b>	<b>Ground motion hazard modelling: The isochron method .....</b>	<b>67</b>
6.5.1.	Algorithm for synthetic seismograms calculations using isochron method.....	67
6.5.1.1.	Input information.....	67
6.5.1.2.	Ray theoretical strong ground motion modelling.....	68
<b>6.6.</b>	<b>Conclusions.....</b>	<b>70</b>
<b>7.</b>	<b>Case studies .....</b>	<b>71</b>
<b>7.1.</b>	<b>Aspects of the seismic response to shaft pillar mining - case studies in the Welkom Gold Field.....</b>	<b>71</b>
7.1.1.	Introduction.....	71
7.1.2.	Mining environment.....	71
7.1.3.	Seismic time histories .....	72
7.1.4.	Seismic hazard.....	75
7.1.5.	Discussion and conclusions.....	78
<b>7.2.</b>	<b>System stiffness and source parameters, <i>E-M</i> relation.....</b>	<b>79</b>
7.2.1.	Variable slopes in <i>E-M</i> relation: Observations.....	79
7.2.2.	Variable slopes in <i>E-M</i> relations: Interpretation.....	83
<b>7.3.</b>	<b>Back analysis of a magnitude 4 event .....</b>	<b>83</b>
<b>7.4.</b>	<b>The Seismic Response to Production.....</b>	<b>86</b>
<b>8.</b>	<b>References.....</b>	<b>88</b>
	<b>Appendix .....</b>	<b>91</b>

**Appendix:**

**Amidzic, D., Murphy, S.K. and van Aswegen G. 1999.** Case study of a large seismic event at a South African gold mine. To be presented at ISRM 9<sup>th</sup> International Congress on Rock Mechanics, Paris, France, September 1999.

**Refer to:**

- GAP 303 – Mid-year Report 1996
- GAP 303 – Year-end Report 1996
- GAP 303 – Mid-year Report 1997
- GAP 303 – Year-end Report 1997
- GAP 303 – Mid-year Report 1998
- GAP 303 – Year-end Report 1998

# List of figures

Figure 1.1 Typical size distribution of a fault population as presented by Fractal (van Berkel, 1998).....	3
Figure 1.2 Distribution of mine raise lines for which fault size distribution data was collected ....	4
Figure 1.3 The variation in fault frequency, a-value, and the slope of the fault frequency/size relation, b-value, for the raise line groups shown in Figure 1.2.....	4
Figure 1.4 Comparison between fault frequency and apparent stiffness for the same set of data shown in Figure 1.3.....	5
Figure 1.5 Comparison between fault frequency and seismic stiffness for the same data set shown in Figure 1.3.....	5
Figure 2.1 Interaction of the inelastic behaviour of the damaged zone with the stiffness of the ambient rockmass: $\epsilon$ , $\sigma$ , $F$ are the strain and stress drops during the instability, $E$ is the energy released during the instability. ....	7
Figure 2.2 Load displacement diagrams with step loading $P$ and dynamic impulse of kinetic energy $E_k$ . The system will become unstable if energy = area ABC > CDE for step loading or if $E_k > ADE$ in case of dynamic loading .....	7
Figure 2.3 Stable (a, b) and unstable (c) responses in the phase space.....	9
Figure 2.4 Trajectories in phase space for plastic deformations .....	9
Figure 2.5 Phase space volume contraction experienced by dissipative system; $X_1$ and $X_2$ are macroscopic state variables.....	10
Figure 2.6 In the top figure contours of $\log D_s$ of one month's data of seismic response to longwall mining in a South African gold mine are shown. One can distinguish at least four areas of high gradient with $D_s$ as high as 0.5 to 1 m <sup>2</sup> /s. One of these areas attracted two larger seismic events, marked by the hourglass symbols, a day later. The bottom figure shows contours of $C(D_s; \bar{t}) = D_s / \bar{t}$ in [m <sup>2</sup> /s/s], where seismic diffusivity is divided by the local average time (over grid size) between seismic events $\bar{t}$ the two larger events which subsequently occurred located in the area of the maximum $D_s / \bar{t}$ .....	12
Figure 3.1 An illustrative plot of cumulative frequency-magnitude with $m_{\min} = -2$ , $a = 4$ and $b = 1$ for the volume $V$ over the time period $t = 1000$ days. Open dots below $m_{\min} = -2$ denote data points below the network's sensitivity that should not be used in parameter estimation. ....	14
Figure 3.2 Time history of cumulative apparent volume, $V_A$ , and energy index, EI, for the seismicity associated with pillar mining within the volume $V = 5.12E7m^3$ . Note that all large seismic events, $\log E > 7.5$ , occurred after the pillar had lost the ability to maintain stress. Note also the differences in d-value (slope of E-M relation) and in the b-value between two six-month periods, indicated by shading, of similar average energy index EI but considerable difference in stiffness.....	17
Figure 3.3 The cumulative frequency-magnitude distributions for the period of January '92 to May '93 (hardening) and June '93 to December '94 (softening); note the characteristic misfit, i.e. the lack of larger events, between the data and the model during the overall hardening regime; note also a considerably higher hazard associated with larger seismic events during the softening period.....	17
Figure 3.4 As 3.3 but for two six-month periods, indicated by shading, at similar average EI but considerable difference in stiffness.....	18
Figure 3.5 The E-M plots for two six-month periods, indicated by shading on Figure 3.2, of similar EI but considerable difference in stiffness; note the higher d-value and lower range of moments domain during May-October 1992. ....	18
Figure 3.6a .....	19
Figure 3.6b .....	19
Figure 3.6c .....	20
Figure 3.6d .....	20
Figure 3.6e .....	21



Figures 3.6a-e Time distribution of seismicity by magnitudes during 36 months of mining WH#6 pillar (right). Magnitude histograms within overlapping windows, as indicated on the time plot, are shown on the left. ....	21
Figure 3.7 The time-of-day distributions of seismic events with $m \geq 1.0$ for the hardening and softening periods; note that hazard for $m \geq 1.0$ at 23h00 until 01h00 and at 10h00 and 12h00 is higher during hardening. ....	22
Figure 3.8 An illustration of a cumulative frequency-magnitude plot of a mixed data set over a limited period of time (left). Events associated with a stiffer system (broken line) and with a softer system (solid line) frequently have different slopes. On a log Energy vs log Moment plot (centre) the same applies. Intermediate and larger events associated with softer systems tend to occur within a few hours of blasting time, $t_b$ , while a stiffer system responds moderately but with larger statistical dispersion, as measured by the normalised standard deviation $\sigma$ , (right).....	23
Figure 4.1 E-M Relations Derived from Seismic Data .....	24
Figure 4.2 Idealistic E-M relation – E-M Ratio Hypothesis.....	26
Figure 4.3 Idealistic E-M relation – E-M Relation Slope Hypothesis.....	26
Figure 4.4 Stable and Unstable System Response.....	28
Figure 4.5 Comparative degree of softening present within two systems.....	29
Figure 4.6 Stable asperity failure with high loading stiffness of surrounding rock.....	30
Figure 4.7 Unstable asperity failure resulting from low loading stiffness of the surrounding rock. ....	30
Figure 4.8 Comparative Resultant Instability Stiffness.....	31
Figure 4.9 Comparative Modelled Instability Stiffness Results .....	35
Figure 4.10 Comparative Inferred E-M Relations.....	36
Figure 4.11 E-M Relation derived from the asperity model.....	39
Figure 4.12 Asperity strength distribution .....	41
Figure 4.13 E-M Relation derived from the asperity model with multiple asperities.....	43
Figure 4.14 Average Stress-Strain Relation derived from a small analysis window .....	44
Figure 4.15 Average Stress-Strain Relation versus average cumulative energy released through time.....	44
Figure 4.16 Average Stress-Strain Relation derived from a small spatial window .....	45
Figure 4.17 Average Stress-Strain Relation derived from a large spatial window .....	45
Figure 4.18 Average instability stiffness modulus analysis .....	46
Figure 4.19 E-M Relation derived from cumulative events .....	47
Figure 6.1 Displacement profiles of the two models tested, shown with the weighted average displacements.....	56
Figure 6.2 UDEC modelling results. The displacement, due to coseismic slip, is shown along the fault plane. Note that the maximum displacement is only 0.5mm, over a fault length of 35m. However, the excavation is only 20m long, and at a horizontal distance of 12m from the fault. Of note here is the shape of the profile, which may be represented by a graph with the x-axis normalised to the source radius, and y-axis normalised to the maximum displacement. ....	57
Figure 6.3 Data from the Welkom Area (Table & Database 6.1). The gradient of the linear regression line is 10.5. ....	62
Figure 6.4 Data from far West Rand (Table & Database 6.2). The gradient of the linear regression fit is 20.7. ....	62
Figure 6.5 Data from Welkom area (Database & Table 6.3). The gradient of the linear fit is 12. ....	62
Figure 6.6 Illustration of modelled source, showing grid points where PPVs were calculated relative to source plane.....	63
Figure 6.7 Graph showing VMAP PPVs at distances from the source. Note: The maximum slip velocity represents the worst possible case. In terms of the model, the smallest value would be 3m/s and the rest of the graph would adapt accordingly.....	64
Figure 6.8 General layout of area. An event of moment magnitude 3.5 was simulated at the position indicated by “Source”, to approximate an event caused by failure to the entire longwall. The isosurface of $\sigma_1$ stress was obtained from an elastic MAP3D model....	66

Figure 6.9	Isosurface of PPVs as indicated. Areas of high damage potential can be identified where high stress coincides with high ground motion. The radiation pattern causes high ground motion in the footwall development area.....	66
Figure 6.10	Fault geometry and source parameterisation .....	68
Figure 7.1	Mining faces of a largely mined out part of Western Holdings Mine depict two major fault loss areas and six shaft pillars. Data for this study were selected from the three polygons shown around Shafts No. 2, 4 and 6.....	71
Figure 7.2	Time history of $GV_a$ and moving median EI for the period 1/1/90 to 28/5/95, WH6#.	73
Figure 7.3	Time history of $GV_a$ and moving median EI for the period 1/1/92 to 28/5/97, WH2#.	73
Figure 7.4	Time history of $GV_a$ and moving median EI for the period 1/1/92 to 28/5/97, WH4#.	73
Figure 7.5	Time history of cumulative production and cum. $V_a$ for the No. 2 shaft pillar. The broken lines accentuate production rates for particular periods.....	74
Figure 7.6	Time history of cum. $V_a$ and cumulative monthly production for WH4# during the period 1/1/92 to 28/5/97.....	74
Figure 7.7	Example of a $\log(E)$ vs. $\log(m)$ plot used to establish an empirical relation for the purpose of calculating Energy Index (EI) and Apparent Stress Level ( $\bar{\sigma}_A < M^{10} >$ ). The broken line connecting a given $\log(m)$ value to an appropriate $\log(E)$ value through the empirical fit, demonstrates the latter concept.....	75
Figure 7.8 (left)	Important geological features, event selection polygons and some of the larger events recorded at WH6#. The mining faces are as they were prior to mining in the pillar.	76
Figure 7.9 (middle)	Important geological features (schematic), event selection polygons and some of the larger events recorded at WH2#. The mining faces are as they were prior to mining the pillar.....	76
Figure 7.10 (right)	Important geological features, event selection polygons and some of the larger events recorded at WH4#. The mining faces are as they were at the approx. 60% extraction stage.....	76
Figure 7.11 (left)	Frequency-magnitude plot for seismic data from WH6 for the period Jan '90 – Mar. '95.....	77
Figure 7.12 (right)	Cumulative frequency-magnitude plot for WH2# for the period 1/1/90 till 28/2/95.....	77
Figure 7.13 (left)	Cumulative frequency-magnitude plot for WH2# for the period 1/11/96 – 30/6/97.....	77
Figure 7.14 (right)	Cumulative frequency-magnitude plot for WH4# for the period 1/1/90 – 31/12/95.....	77
Figure 7.15	Cumulative frequency-magnitude plot for WH4# for the period 1/11/96 – 30/6/97.	78
Figure 7.16	.....	80
Figure 7.17	.....	80
Figure 7.18	.....	81
Figure 7.19	.....	82
Figure 7.20	.....	82
Figure 7.21	The mining situation for the back analysis described in the text. Also shown is the polygon for event selection used for the analysis.....	84
Figure 7.22	An example Gutenberg-Richter plot for one of the 27 four month time periods (forward stepping by one month) analysed.....	84
Figure 7.23	An E-M plot for the same dataset reflected in Figure 3, except that all events $< \log(M)9.0$ are filtered out – this was done for all the datasets analysed.....	85
Figure 7.24	The variation of the Gutenberg-Richter b value and the E-M d value over the 27 months prior to the large event. The b value varies between 0.62 and 0.84 while the d value varies between 1.46 and 1.55.....	85
Figure 7.25	The variation of apparent stress level (30 to 90 KPa) and apparent stiffness (40 to 110 MPa) for the 27 months prior to the large event. The arrows indicate the occurrence of events larger than $\log(E)10$ , the last arrow reflecting the occurrence of the main event of interest here.....	86

## List of tables

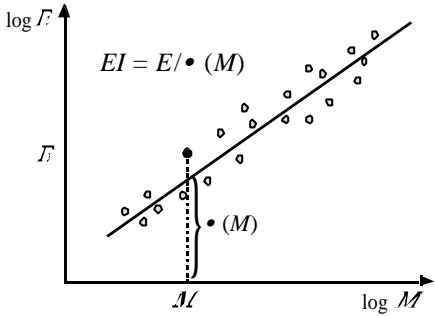
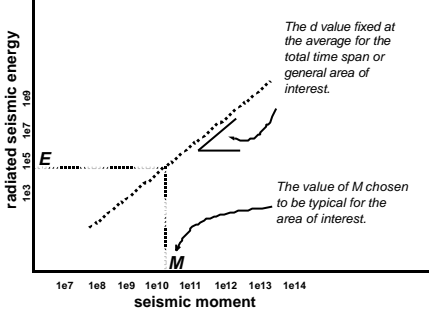
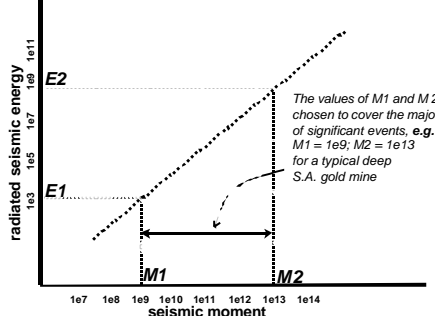
Table 4.1 Experiment 1 Model Parameter Assumptions .....	34
Table 4.2 Comparative Modelled Instability Stiffness Results.....	35
Table 4.3 Inferred E-M Relation Parameters .....	36
Table 4.4 Experiment 2 Model Parameter Assumptions .....	37
Table 4.5 Calculated E-M Parameters derived from the Asperity Model.....	38
Table 4.6 Comparative quantitative E-M Ratio and Gradient between systems.....	39
Table 4.7 Experiment 3 Model Parameter Assumptions. ....	40
Table 4.8 Asperity strength distribution parameter assumptions .....	41
Table 4.9 Calculated E-M Parameters derived from the asperity model. ....	42
Table 6.1: Seismic database 1 (Welkom area), large events during 1992. The rise time was obtained from the duration of the first swing of the acceleration waveform, and the average displacement was obtained from the source area and seismic moment. The average displacement is multiplied with a factor according to the displacement profiles used, to obtain an estimate of the maximum slip velocity in the source.....	60
Table 6.2: Seismic database 2 (Far west rand), large events during 1998 and 1999. See Table 6.1 for more information. ....	60
Table 6.3: Seismic database 3 (Welkom area), events during 1997 and 1998. See Table 6.1 for more information. ....	61
Table 7.1 Some characteristics of the pillars of Shafts Number. 2, 4 and 6, Western Holdings Mine.....	72
Table 7.2 Apparent Stress Level, i.e. average apparent stress for $\text{Log}(M)=10$ ( $\bar{s}_A < M^{10} >$ ) for different stages of mining at WH Numbers 2 and 4 Shafts. The units are KPa.....	75
Table 7.3: b-values, recurrence times (Rt, in months) and probability of occurrence (within 1 month) for mag.m or larger events for stages: before main pillar mining stage (-B), late/final stage (-F) and total period (-T). F1 and F2 refer to the two populations of events at WH2#. ....	78

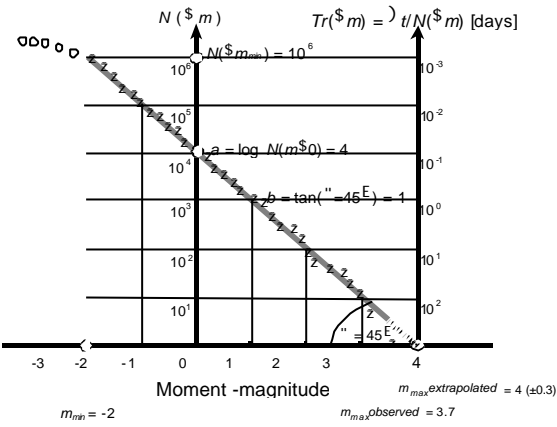
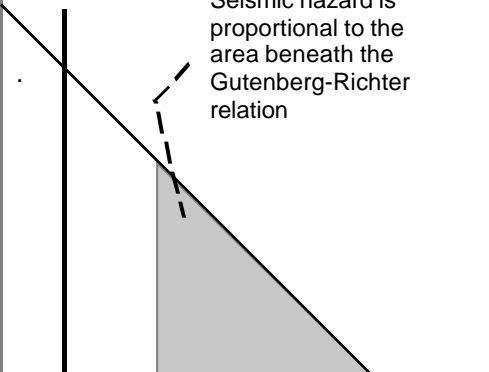
# Glossary of seismic terms

Parameter, relevant formula	Description
<b>Magnitude, <math>m</math></b> $m = \log(A/T) + C$ $A/T$ - the maximum displacement over associated period in the P- or S- wave group $C$ - corrections for path effects, site response and source region	Magnitude is a relative measure of the strength of a seismic event based on measurements of maximum ground displacement at a given frequency at multiple seismic sites. A unit increase in magnitude corresponds to a 10-fold increase in amplitude of ground displacement. Gutenberg and Richter related seismic energy and magnitude derived from P-waves recorded at large distances from the source at 1sec period as $\log E(\text{ergs}) = 2.4m + 5.8$
<b>Seismic moment, <math>M</math>, [Nm]</b> and <b>Moment-magnitude, <math>m</math></b> $m = 2/3 \log M - 6.1$	A scalar that measures the coseismic inelastic deformation at the source. Since seismic moment is proportional to the integral of the far field displacement pulse it can easily be derived from recorded waveforms. A relation that scales seismic moment into magnitude of a seismic event is called moment-magnitude.
<b>Seismic moment tensor</b> $M_{ij} = \int_V c_{ijkl} \Delta \epsilon_{kl} dV = \int_V \Delta s_{ij} dV, \text{ where}$ $\Delta q = \text{tr}(M_{ij}) / (3I + 2G), \text{ where}$ $I = \int_V s_{kk} dV$ $G = \int_V s_{ij} s_{ij} dV$ <p> <math>c_{ijkl}</math> - elastic constants  <math>\Delta \epsilon_{kl}</math> - strain change at the source  <math>\Delta s_{ij}</math> - stress change or change in moment per unit volume  <math>I</math> - the second Lamé constant  <math>G</math> - rigidity         </p>	The most general description of the processes at the seismic source $V$ is by the distribution of forces or moments equivalent to the inelastic deformation. One can describe the inelastic processes at the source as the stress-free change of size and shape of an elastic body without alteration of the elastic properties of the region. If change in size and shape can be expressed as a change in strain $\Delta \epsilon_{kl}$ , then the equivalent stress change, or change in moment per unit volume is proportional to the strain change. The total moment integrated over the source volume is the seismic moment tensor, $M_{ij}$ . For long waves compared to the source size, the whole source volume $V$ can be considered to be a system of couples located at, say, the centre of $V$ , and the moment tensor components can be defined by the equation at left. The moment tensor measures the inelastic deformation at the source during the seismic event and its value at the end of the source process measures the permanent inelastic strain produced by the event. The seismic moment tensor can be decomposed into isotropic (or volume change) and deviatoric components providing an additional insight into the nature of the coseismic strain drop. For a homogeneous body, the coseismic volumetric change, $\Delta V/V$ , can be calculated from the second equation at left. The eigenvalues and corresponding eigenvectors of the deviatoric component of the seismic moment tensor describe the magnitude and orientation, respectively, of the principal moment axes (neglecting gravity) acting at the source. These principal moment axes are uniquely determined by moment tensor inversion. Principal moment orientation data can provide sufficient information to find the best stress tensor.
<b>Radiated seismic energy, <math>E</math>, [J]</b>	The portion of the energy released or work done at the source that is radiated as seismic waves. Seismic energy is proportional to the integral of the squared velocity spectrum in the far field and can be derived from recorded waveforms. Radiated seismic energy increases with stress drop, seismic moment and with the traction rate i.e., stress oscillations at the source.

Parameter, relevant formula	Description
<b>Corner frequency, <math>f_0</math>, [Hz]</b> and <b>Source size, <math>l</math>, [m]</b> $l = c_1 / f_0$ $c_1 = 2500$ for S-wave in hard rock	The frequency at which a source radiates the most seismic energy observed as the maximum on the source velocity spectrum or as the point at which a constant low frequency trend and a high frequency asymptote on the recorded source displacement spectrum intersect. The corner frequency is inversely proportional to the characteristic size of the source.
<b>Stress drop, <math>\Delta\sigma</math>, [Pa]</b> $\Delta\sigma = c_2 M f_0^3$ $c_2 = 1.8 \times 10^{-10}$ for S-waves in hard rock $\Delta\sigma = G \Delta\epsilon$ , and $\Delta\epsilon$ - strain drop	Stress drop estimates the stress release at the seismic source. Although it is model dependent it provides reasonable estimates and a fair comparison amongst different sources from the same region recorded by the same seismic system.
<b>Source area, [m<sup>2</sup>]</b> $A = M / (Gu)$ $u$ - average displacement at the source.	The area of coseismic inelastic deformation over the planar source.
<b>Source volume, [m<sup>3</sup>]</b> $V = M / \Delta\sigma$	The volume of coseismic inelastic deformation of the order of $M / \Delta\sigma$ .
<b>Apparent stress, [Pa]</b> $s_A = GE / M = E / (\Delta\epsilon V)$ or $s_A = E / (uA)$ .	Apparent stress is recognised as a model independent measure of the stress change at the seismic source.
<b>Apparent volume, [m<sup>3</sup>]</b> $V_A = M / (c_3 s_A) = M^2 / (c_3 GE)$ $c_3$ - scaling factor $\approx 2$ .	The apparent volume scales the volume of rock with coseismic inelastic strain of an order of apparent stress over rigidity. The apparent volume $V_A$ is less model dependent than the source volume $V$ .
<b>Seismic strain, <math>\epsilon_S</math></b> $(\Delta V, \Delta t) = \Sigma M / (2G\Delta V)$ and <b>Seismic strain rate, [s<sup>-1</sup>]</b> $\dot{\epsilon}_S (\Delta V, \Delta t) = \epsilon_S / \Delta t$	Seismic strain measures strain due to cumulative coseismic deformations within the volume $V$ over the period $t$ . Its rate is measured by $\dot{\epsilon}_S$ .
<b>Seismic stress, <math>\sigma_S</math> [Pa]</b> $s_S (\Delta V, \Delta t) = 2G\Sigma E / \Sigma M$	Seismic stress measures stress changes due to seismicity.
<b>Seismic stiffness modulus, <math>K_S</math> [Pa]</b> $K_S (\Delta V, \Delta t) = s_S / \epsilon_S = 4G^2 \Delta V \Sigma E / (EM)^2$	Seismic stiffness measures the ability of the system to resist seismic deformation with increasing stress. The stiffer systems limit both the frequency and the magnitude of intermediate and large events but have time-of-day distribution with larger statistical dispersion, thus are less time predictable.
<b>Seismic viscosity, [Pa @s]</b> $h_S (\Delta V, \Delta t) = s_S / \dot{\epsilon}_S$	Seismic viscosity characterises the statistical properties of the seismic deformation process. Lower seismic viscosity implies easier flow of seismic inelastic deformation or greater stress transfer due to seismicity.
<b>Seismic relaxation time, [s]</b> $t_S (\Delta V, \Delta t) = h_S / G$	Seismic relaxation time quantifies the rate of change of seismic stress during seismic deformation processes and it separates the low frequency response from the high frequency response of the system under consideration. It also defines the usefulness of past data and the predictability of the flow of rock. The lower the relaxation time, the shorter the time span of useful past data and the less predictable the process of seismic deformation.

Parameter, relevant formula	Description
<b>Seismic diffusivity, [m<sup>2</sup>/s]</b> $D_S(\Delta V, \Delta t) = (\Delta V)^{\frac{2}{3}} / t_S$ , or in a statistical sense $d_S = (\bar{X})^2 / \bar{t}$ .	Seismic diffusivity can be used to quantify the magnitude, direction, velocity and acceleration of the migration of seismic activity and associated transfer of stresses in space and time. There is an inverse relationship between the diffusivity $D_S$ and the friction parameters.
<b>Seismic Deborah number</b> $De_S(\Delta V, \Delta t) = t_S / \text{flowtime}$ , where <i>flowtime</i> is a design parameter not necessarily equal to $t$ .	Seismic Deborah number measures the ratio of elastic to viscous forces in the process of seismic deformation and has successfully been used as a criterion to delineate volumes of rockmass softened by seismic activity (soft clusters). The lower the Deborah number the less stable is the process or the structure over the design <i>flowtime</i> - what may be stable over a short period of time (large $De_S$ ) may not be stable over a longer time (lower $De_S$ ).
<b>Seismic Schmidt number</b> $Sc_{sD}(\Delta V, \Delta t) = h_S / (rD_S)$ or $Sc_{sd} = h_S / (r d_S)$ where D is rock density.	Seismic Schmidt number measures the degree of complexity in space and time (the degree of turbulence) of the seismic flow of rock. Note that seismic Schmidt number $Sc_{sD}$ , encompasses all four independent parameters describing seismicity: $\bar{t}, \bar{X}, \Sigma M, \Sigma E$
<b>Time to failure, (<math>t_f - t</math>)</b> $d\Omega / dt = k(t_f - t)^a$ S - measurable quantity t - current time $t_f$ - time of failure k, " - constants 	This concept describes the behaviour of materials in the terminal stages of failure. It views instability as a critical point, then precursors should follow characteristic power laws in which the rate of strain or other observable, measurable, quantity S is proportional to the inverse power of remaining time to failure. Observed oscillations in S of an increasing frequency as the failure approaches are part of the solution to time-to-failure equation with a complex exponent, where the imaginary part relates to discrete scale transformation and introduces log-periodic oscillations decorating the asymptotic power law. The observations S can be a combination of different seismic parameters that would exhibit power law type increase before failure. For well behaved data sets the time at failure $t_f$ can be estimated from the times of three successive maxima ( $t_1, t_2, t_3$ ) of the observed process $t_f = (t_2^2 - t_1 t_3) / (2t_2 - t_1 - t_3)$ . Note that, in theory, $t_3 - t_2 < t_2 - t_1$ .

Parameter, relevant formula	Description
<p><b>Energy index, EI</b></p>  <p><math>EI = E / \bar{E}(M)</math></p>	<p>The notion of comparing the radiated energies of seismic events of similar moments can be translated into a practical tool called Energy Index (<math>EI</math>) – the ratio of the radiated energy of a given event (<math>E</math>) to the energy <math>\bar{E}(M)</math> derived from the regional <math>\log E</math> vs <math>\log M</math> relation for a given moment <math>M</math>. Since <math>\log \bar{E}(M) = c + d \log M</math>, then <math>\bar{E}(M) = 10^{c+d \log M}</math> where <math>c</math> and <math>d</math> are constant for a given <math>\Delta V</math> and <math>\Delta t</math>. In general <math>d</math>-value increases with the system's stiffness and <math>c</math> increases with stress. A small or moderate event with <math>EI &gt; 1</math> suggests a higher than average shear stress at its location. The opposite applies to the <math>EI &lt; 1</math> case.</p>
<p><b>Apparent stress level, <math>\sigma_{AL}</math> [Pa]</b>  <math>[\sigma_{AL}(c)]_{d,M \text{ constant}} = (G/M)10^{(c + d \log M)}</math></p>  <p>The <math>d</math> value fixed at the average for the total time span or general area of interest.</p> <p>The value of <math>M</math> chosen to be typical for the area of interest.</p>	<p>For a given slope <math>d</math> of the E-M relation, the constant <math>c</math> would indicate the level of stress (from all events in the data set) in the same way as the <math>EI</math> does for a single event. It is a useful engineering parameter for the comparison of stress variation in space or time. By choosing the fixed <math>M</math> as the average for the data set, <math>\sigma_{AL}</math> would be equivalent to the average apparent stress.</p>
<p><b>Apparent stiffness, <math>K_{AS}</math> [Pa]</b>  <math>K_{AS}(d,c) = G(E_2 - E_1)/(M_2 - M_1)</math></p>  <p>The values of <math>M_1</math> and <math>M_2</math> chosen to cover the majority of significant events, e.g. <math>M_1 = 1e9</math>; <math>M_2 = 1e13</math> for a typical deep S.A. gold mine</p>	<p>The <math>d</math> value of the E-M relation is considered to reflect local seismic stiffness. Apparent stiffness is defined as <math>K_{AS}(d,c) = G(E_2 - E_1)/(M_2 - M_1)</math> where <math>E_2</math> and <math>E_1</math> are the typical values of <math>E</math> for the two values of <math>M</math>, <math>M_2</math> and <math>M_1</math>. For <math>K_{AS}</math> a moment range <math>M_2</math>, <math>M_1</math> is chosen which spans the bulk of the data. Since <math>K_{AS}</math> depends on both <math>d</math> and <math>c</math>, it is more informative than considering <math>d</math> only. While the seismic stiffness modulus is based on quantitative seismicity, apparent stiffness is based on the model E-M relation, thus being less sensitive to the effect of single large events.</p>

Parameter, relevant formula	Description
<p><b>Gutenberg-Richter relation</b>  <math>\log N(\\$m) = a - bm</math>,</p> 	<p>Gutenberg-Richter relation describes the frequency-magnitude distribution of small and intermediate size earthquakes,  <math>\log N(\\$m) = a - bm</math>,  where <math>N(\\$m)</math> is the expected number of events not smaller than magnitude <math>m</math>, and <math>a</math>, <math>b</math> are constant  The schematic illustrates the cumulative frequency-magnitude distribution with <math>m_{\min} = -2</math>, <math>a = 4</math> and <math>b = 1</math> for the volume <math>V</math> over the time period <math>t = 1000</math> days. Open dots below <math>m_{\min} = -2</math> denote data points below the network's sensitivity that should not be used in parameter estimation.</p>
<p><b>Hazard magnitude</b></p>  <p>Seismic hazard is proportional to the area beneath the Gutenberg-Richter relation</p>	<p>The estimated number of seismic events within the magnitude range <math>m_1</math> and <math>m_2</math>, where <math>m_1 &lt; m_2 \neq m_{\max}</math>, is  <math>N(m_1 \neq m_2) = N(\\$m_1) - N(\\$m_2)</math>.</p> <p>Where the Gutenberg-Richter relation is based on moment magnitude, the cumulative moment release, EM, by all these events can be estimated from  <math>\Sigma M = 0.43 \cdot 10^{a+9.1} (10^{m_2(1.5-b)} - 10^{m_1(1.5-b)}) / (1.5 - b)</math>  for <math>b &lt; 1.5</math>.  With <math>m_1</math> is the minimum magnitude that can cause damage, the hazard magnitude <math>Hm</math> can be defined as  <math>Hm = (2/3) \log \Sigma M - 6.1</math></p> <p>Similar relations can be derived for cases where the local magnitude is calculated from radiated seismic energy or from combinations of energy and moment.</p>
<p><b>Volume of Ground motion.</b></p> $VGM = \frac{An^c bN}{Q} \frac{e^{-Qm_0} - e^{QX_{\max}}}{e^{-bm_{\min}} - e^{-b_{\max}}}$ <p>where</p> <ul style="list-style-type: none"> <li><math>A = (4p/3) \exp(-3A_3/A_2)</math></li> <li><math>c = 3/A_2</math></li> <li><math>Q = b + (3A_1/A_2)</math></li> <li><math>A_1 = a_1 \ln 10</math>, <math>A_2 = a_2</math>; and <math>A_3 = a_3 \ln 10</math> in the formula: <math>r \log_{10} (n [mm/s]) = a_1 m + a_2 \log_{10} [m] + a_3</math>, where <math>n</math> is peak ground velocity in [mm/s], <math>r</math> is distance from the source in [m], and <math>m</math> is magnitude measured from the seismic energy using the formula <math>m = d \log_{10} E [J] + f</math> (frequently used values for the coefficients are <math>a_1 = 0.8</math>, <math>a_2 = -1.9</math> or <math>-1.8</math>, <math>a_3 = 3.4</math>, <math>d = 0.526</math> and <math>f = -1.16</math>)</li> <li><math>b = b \ln 10</math>, where <math>b</math> is the <math>b</math>-value in the magnitude-frequency relationship <math>\log_{10} n = a - bm</math> (or <math>n = e^{a-bm}</math>, <math>a = a \ln 10</math>), with <math>n</math> being the number of events with magnitudes larger than <math>m</math></li> <li><math>m_{\min}</math> is the minimum magnitude above which the magnitude-frequency relationship of a straight line in a log-log scale whose slope provides the values for <math>b</math> (or <math>b</math>)</li> <li><math>m_{\max}</math> is the maximum magnitude, either calculated as <math>m_{\max} = 2X_{\max-1} - X_{\max}</math>, where <math>X_{\max}</math> and <math>X_{\max-1}</math> are the maximum observed magnitude and the last but one maximum observed magnitude, respectively; or <math>X_{\max}</math> is used instead of <math>m_{\max}</math></li> <li><math>m_0</math> is the minimum magnitude of damage</li> <li><math>N = n(m_{\min})</math> is activity rate, ie., the number of events with magnitudes exceeding <math>m_{\min}</math>; it is either taken from the observed data for the study period or time, or is calculated from the magnitude-frequency relationship as <math>N = \exp(a - bm_{\min})</math></li> </ul>	<p>The volume of ground motion defines the total volume of the rock mass affected by peak velocities of ground motion exceeding a given value. It is a single number representing several parameters, namely <math>a</math>, <math>b</math>, <math>m_{\max}</math>, minimum magnitude at which to expect damage and an empirical relation between PPV, magnitude and distance.</p>



Parameter, relevant formula	Description
<p><b>Seismic moments, volume mined and relative stress</b></p> <p>Title: /loc/iss/iss/WorkSpace/volmined.eps Creator:</p> <p>Preview: This EPS picture was not saved with a preview included in it.</p> <p>Comment: This EPS picture will print to a PostScript printer, but not to other types of printers.</p>	<p>If a volume of rock, <math>V_m</math> is mined out at time <math>t_0</math> and if the altered stress and strain field can readjust to an equilibrium state through seismic movements only, the sum of seismic moments released within a given period of time would be proportional to the excavation closure and in the long term at <math>t = t_4</math></p> $\sum_{t_0}^{\infty} M = GV_m$ <p>where <math>M</math> is the scalar seismic moment. The relative stress level at the time, <math>t</math>, in a given volume of rock <math>V</math> surrounding the excavation, can be calculated from the difference between <math>GV_m</math> and the cumulative moments released to date:</p> $s_r(t) = (GV_m - \sum_{t_0}^t M) / \Delta V .$
<p><b>Seismic moments and volume of elastic convergence</b></p> <p><math>GM = (GV_e</math></p>	<p>The amount of strain energy stored when mining in elastic rock is directly proportional to the volume of elastic convergence, <math>V_e</math>. It has been found that the total amount of seismic moment resulting from mining within a large area and time period is related to the change in elastic convergence <math>V_e</math>. The proportional constant gamma, <math>\zeta</math>, has been found to vary between about 0.03 and 1.0. There is some evidence that <math>\zeta</math> is a function of the geotechnical area being mined.</p>

# Introduction

The main objective of the project was to develop methodologies to quantify and compare the seismic hazard associated with different mining layouts, rates of mining and/or different geological structures. A second objective was to develop a method to average and analyse complex spatio-temporal patterns in mining induced seismicity. This final report describes the methodologies and results that contributed to the main research findings described in the executive summary. More comprehensive descriptions of the research activities undertaken under the GAP 303 are reported in interim progress reports.

## 1. The geological structure

### 1.1. Structural fabric of rock

There is little doubt that most larger seismic events are associated with geological discontinuities. To the rock engineering practitioners on South African gold mines, the available information about these structures is limited to the best estimate of where the largest structures are, with some reasonable estimates of the strike orientations and limited information about the dip orientations. Methods and procedures for the analysis of individual structures have been developed and are described in the GAP 303 1996 reports. These are methods to utilise minimal information about individual structures and to do optimised interpretation of the 3D geometries for purposes of evaluating stability.

A more general description is required, however, to quantify the structural fabric of the rockmass. The term 'fabric' is generally used by structural geologists referring to the density, orientation and mechanical nature of cleavages, foliations, lineations etc. observable on meso-scale (hand specimens, rock outcrops). In the description of the rock fabric on this scale, joints are usually ignored by geologists.

Still at the meso-scale, albeit at the higher end, rock mass classifications (RMR, RQD, etc.) are attempts to qualify and/or quantify the effects of the rock fabric on the rock strength - observations are made in drill core and in mine tunnels and stopes. These classifications are mainly based on the density and mechanical nature of the joint system(s), since these structures are the most important in general strata control. The small seismic events close to the mine openings are a simple extension of the fracturing process induced by the high stress in the immediate vicinity of the mine openings - the frequency and size distribution of these events will mainly be controlled by the stress conditions and the rock mass character at the meso scale.

The larger seismic events are associated mainly with the structural fabric at the macro scale, about which information is limited. While rock mechanics practitioners do rock mass classification for strata control purposes and, in some South African gold mines limit seismicity by controlling mining faces so as not to be parallel to the most prominent joint sets, no systematic attempt is made to describe or quantify the macro scale rock fabric, namely the fault/dyke system. A method is described below which could serve as the basis for quantifying this macro-fabric.

### 1.2. The size distribution of discontinuities

The size distribution of many natural phenomena obey a simple power law:

$$N = cM^D \tag{1.1}$$

where  $N$  is the cumulative number of observations and  $M$  the feature size (say fault displacement), with  $a$  and  $D$  parameters characteristic of a particular situation. It can be shown that critical phenomena obey such power law size distribution - whether the fact that a power

law is obeyed necessarily reflects criticality is, however, debatable (see 1998 mid-year report on GAP409).

The usual way to state this law is in the logarithmic form

$$\log(M) = \log(c) - D \log(M) = A - D \log M, \quad (1.2)$$

where  $A$  measures the overall occurrence rate and  $D$  is controlled by the distribution of faults between the higher and the lower size range.

### 1.2.1. Application to fault size distribution

The size distribution of faults can also be measured and quantified through power laws. The question, of course, immediately arises as to how one measures the size of a fault. From aerial or satellite photographs the length of fault traces can be measured, assuming that the fault throw increases proportionally with the strike length of the structure (*Ouillon and Sornette (1996)*). Three dimensional seismic reflection surveys can be used to measure the vertical displacements over faults (e.g. *Walsh and Watterson, 1992*). Where the population of faults analysed are of the same origin, a simple power law size distribution is expected. Where more than one, and dissimilar tectonic cycles contributed to the faulting, a breakdown of the power law distribution can be expected - in such a case the deviation from perfect power law distribution could be used to indicate the complexity of the tectonic history.

The applications of the power law size distributions of features in rock is growing and finding its way into rock engineering (e.g. *Carr (1997), Pelletier et al. (1997)*).

To analyse the size distribution of faults on mines could be considered relatively simple since geological mapping of most excavations are generally kept up to date and the required information is readily available. For most part, however, only the vertical component of displacement is recorded because (a) in general, that is all that is important from a mining point of view, and (b) it is very difficult to establish the actual finite slip vector on each fault. One could, for example, note the vertical component of displacement as well as the slip striations on the fault surface, allowing the actual slip vector to be established through simple trigonometry. The problem is that the striations are neither readily observed nor do they necessarily represent the most significant part of the displacement history along the structure. In practice, the best way would be to simply take the vertical displacement as a measure of the fault size - if the slip mechanism was consistent, e.g. if all the faults actually show oblique slip in the same direction, the vertical displacement would be a constant fraction of the actual displacement.

### 1.2.2. Application to fault populations in mines

Excellent work has lately been done on Anglogold mines applying the principles described above to quantitatively describe variation in the nature of fault populations (*Brown, 1995; Birch, 1996; Van Berkel, 1998*). Procedures are now in place in their geology departments to do fault size distribution analyses in a standardised way. One purpose of these analyses is to classify mining areas in terms of expected mining difficulty, the experience being that a high density of small faults (both the parameters in the power law being high) limit production rate.

The procedure involves collection of data from reef raise line mapping and the transfer of the data to a spreadsheet program via a standard pro-forma. A spreadsheet program, Fractal, does a line fit to automatically derive  $A$  and  $D$  parameters with an option to correct these based on the visual inspection of a graphical representation (*van Berkel, 1998*). Where  $a$  in the Gutenberg-Richter analysis is  $\text{LOG}(\text{total number of events greater than magnitude } 0 \text{ for the data set analysed})$ , which can be normalised to represent this event frequency over say, a one year period, the  $a$  value from Fractal is already normalised, namely (total number of faults/km

with throws > 1 metre). Note the equivalence - the 1 metre represents the 0 axis on the log-log plot (Figure 1.1).

The fault size distribution plot in Figure 1.1 shows exactly the same features as the Gutenberg-Richter plot, with a minimum value below which the recording system (geological mapping in this case) is not sensitive. Towards the large size end the size/frequency scaling relation becomes less obvious because of a lack of data.

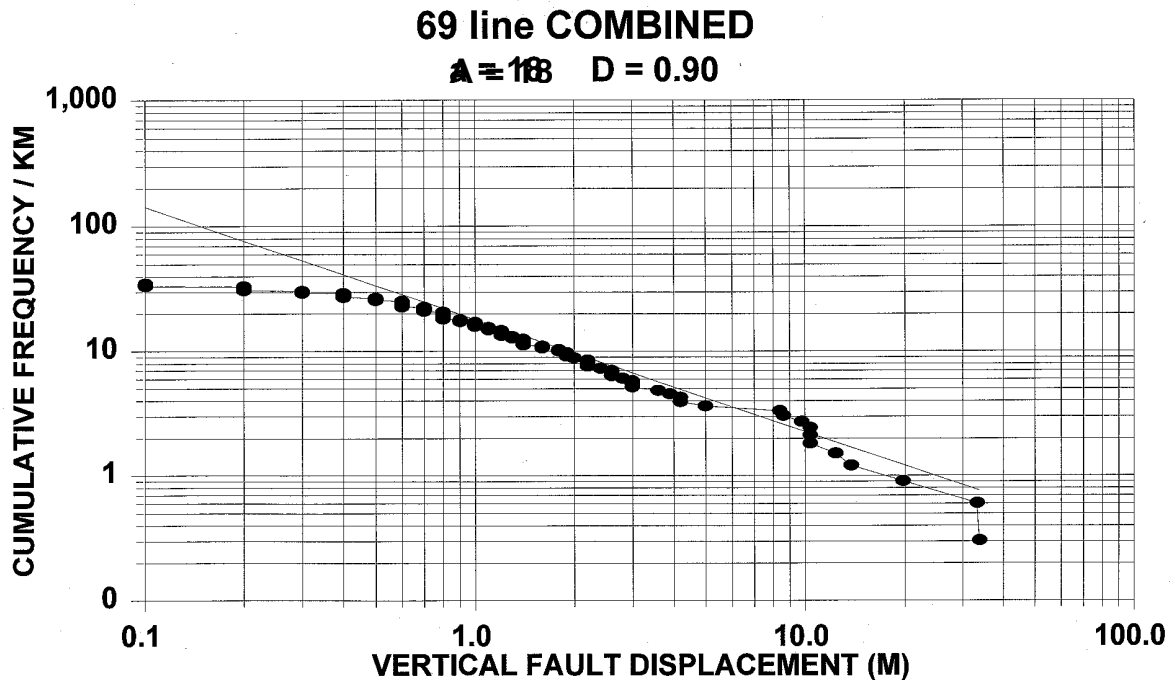


**Figure 1.1 Typical size distribution of a fault population as presented by Fractal (van Berkel, 1998)**

A mixed population of structures (from different tectonic cycles) would most probably cause the scaling relation to break down, or, at least, cause scatter around the best-fit line. Such a mixed population of structures may represent a larger variation in fault strength characteristics with implications for seismic hazard.

### 1.2.3. Comparison with seismic hazard related parameters

Data should be analysed to compare the size distribution of faults with the seismic hazard related parameters for places where fault population studies were done and where sufficient seismic data is available. Results described here come from one of the study sites.

Figure 1.2 shows the distribution of raise lines for which fault population data was available. The initial data collection was done by mine geology staff and made available for further processing. The processing involved the grouping of data into a series of overlapping polygons acting as a moving average window from the one end of the study area to the other. The fault size distribution in each polygon was then evaluated.

For the same polygons, seismic events were selected and seismic hazard related parameters were calculated. Figure 1.3 shows the variation in the  $A$  and  $D$  values along the length of the study area, indicating greater fault frequencies in the northern, central and southern parts with lower densities in between. In Figure 1.4 a good correlation between the fault frequency and the apparent stiffness, derived from the seismic data, is shown. Figure 1.5, however, shows a poor correlation with seismic stiffness, being low where production rate is high and vice versa.

Seismic stiffness is dominated by the contribution of the larger events associated with higher mining rates. It appears that apparent stiffness reflects the inherent properties of the rockmass independent of the seismic strain rate. This could be useful since apparent stiffness could be used during the early stages of mining to validate assumptions about the rock mass stiffness at design stage.

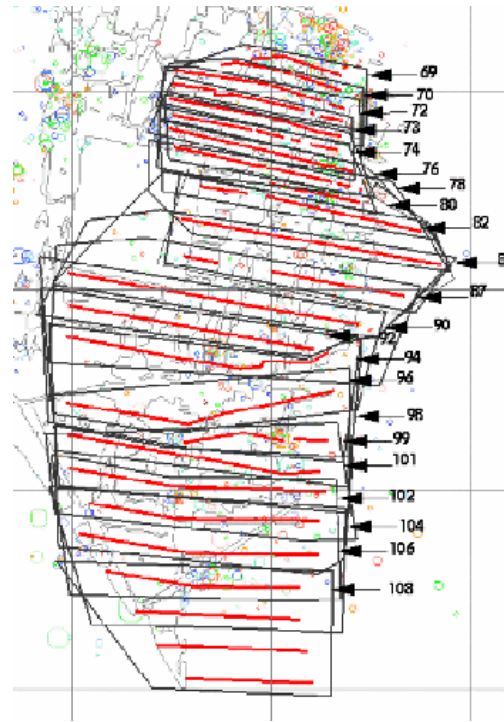


**Figure 1.2** Distribution of mine raise lines for which fault size distribution data was collected

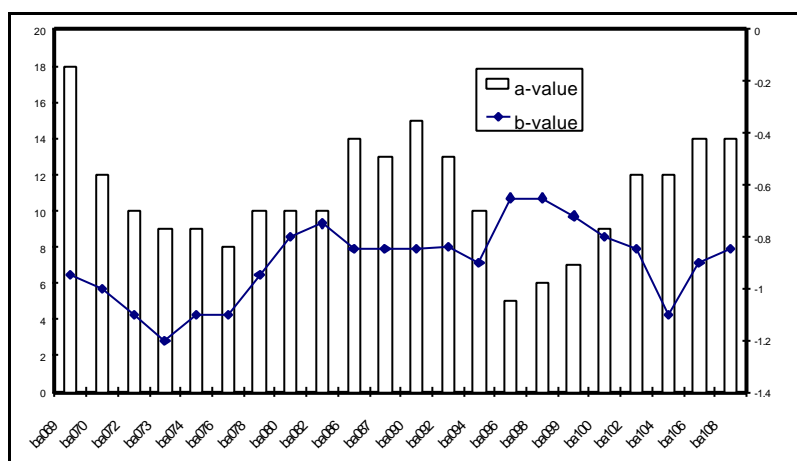


**Figure 1.3** The variation in fault frequency, a-value, and the slope of the fault frequency/size relation, b-value, for the raise line groups shown in Figure 1.2

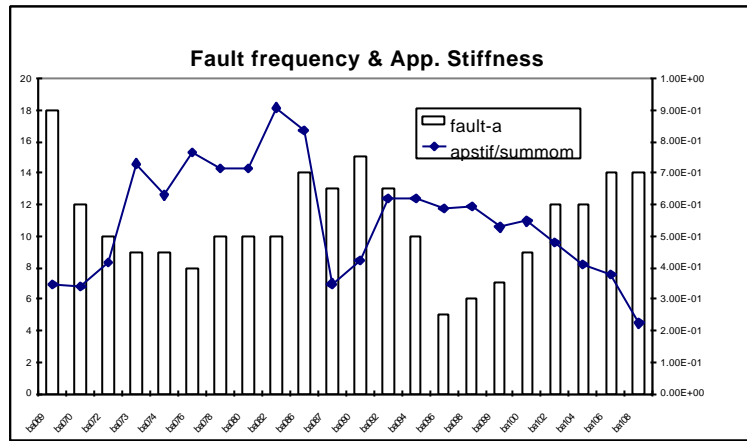


**Figure 1.4 Comparison between fault frequency and apparent stiffness for the same set of data shown in Figure 1.3**

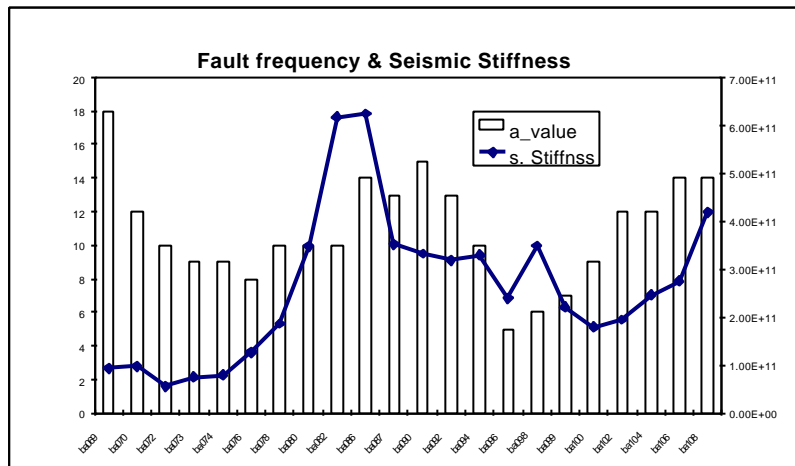


**Figure 1.5 Comparison between fault frequency and seismic stiffness for the same data set shown in Figure 1.3**

The macro-fabric is obviously an important component of seismic hazard, but the effects in variation in characteristics thereof may not necessarily be so straightforward. Consider, for example two cases where the same mining method is used at the same depth within the same stratigraphy (the primary geotechnical area classification would be the same), but for area A the fault *a* and *b* values are both high while in area B both these values are low. One may consider area A more hazardous because of the higher frequency of faults, each of which could potentially become unstable. On the other hand, this greater frequency of weaknesses could render the rockmass softer, making it yield more easily and not allowing stress to accumulate to extreme values. Furthermore, and possibly most importantly, the increase in mining difficulty could slow down mining rate, limiting seismic hazard.

### 1.3 Geological structures: geometric modelling

Methods for the analysis of individual structures include special fault/dyke surface fitting procedures, utilising not only the positions in space of data points but also the orientation (strike and dip). The latter allows an expansion of the data, in principle providing the first derivative to the surface at different points. In practice the orientation data is used to simply expand the original data points to whatever the confidence level of the orientation data is. Fitting Bezier

surfaces through the expanded data is a convenient method for surface fitting for geological discontinuities (1997 mid year report, Appendix 2). Such surfaces are used for seismic event selection for purposes of evaluating fault stability. Furthermore surface grids are used in numerical models for the same purpose (see chapter 6 below).

## 2. Rockmass stability and system stiffness

A system, in this report, is defined as a volume of rockmass )  $V$  with its geological features, mine layout and the inelastic deformation caused by mining. The physical progressive process associated with the development of inelastic deformation is called damage. The physical cause of damage is the initiation, growth, propagation and coalescence of cracks and voids at different scales. Mine layout and the damage influence the system's stiffness i.e. its ability to resist deformation with increasing loads and/or with time, and degrades the system's strength. As it happens the system is losing the ability to contain its response to perturbations and an unstable deformation can be triggered with time by the next mining step and/or by the transient dynamics associated with a distant event or blasting.

### 2.1. Stability of deformation and stability of a system – static considerations

The deformation is considered to be stable, or unstable, if the inner product of the next increment of stress  $dF$  with the next increment of strain  $d$ , is positive, or negative, respectively, thus

$$dsd\epsilon = dsd\epsilon_e + dsd\epsilon_{in} \begin{cases} > 0 \text{ stability} \\ < 0 \text{ instability} \end{cases} \quad (2.1)$$

where  $d_e$ ,  $d_{in}$  are elastic and inelastic strain increments. Since for the elastic strain increments, usually  $dFd_e > 0$ , the deformation will be unstable only if the inelastic term balances the elastic one, so that there is a net strain softening. As stress and strain are tensors, there are many different components that may be influential in causing the instability. However the possibility of localisation i.e. an unstable mode of deformation, arises even if one stress component is able to decrease with increasing strain.

The increments  $dF$  and  $d$ , are interrelated by the constitutive relation

$$ds = Kd\epsilon \Rightarrow d\epsilon = K^{-1}ds, \quad (2.2)$$

where  $K$  is the incremental stiffness matrix that, in general, depends on the stress state and the loading history.

The growth of the unstable deformation processes within the system up to the point of instability is called damage evolution. Breakdown instability will only take place once sufficient damage, including excavations, has occurred within the critical volume(s) of the system. Stress drop within the damaged zone(s) induces some elastic unstraining and redistribution of stresses in the ambient rock. The size, shape, the degree and the distribution of the damage zones prior to system instability depends mainly on mine layout, and it will influence the stress, strain drops and the energy release during instability. One can then consider an interpretation of instability in terms of the relative stiffness of the components of the system – an instability will occur when the overall stiffness of the damaged zone(s), including excavations, is equal or exceeds the unloading stiffness of the surrounding, mostly elastic, rockmass – see Figure 2.1. Alternatively, an instability can be caused by relative strain softening of the components of the system where rock within the damaged zone(s) hardens at a lower rate than the ambient rock.

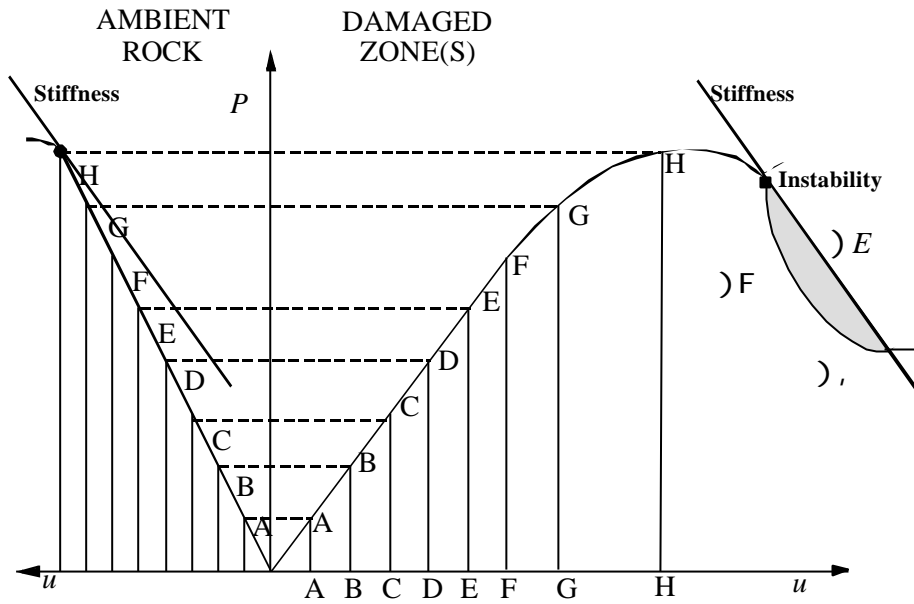


**Figure 2.1** Interaction of the inelastic behaviour of the damaged zone with the stiffness of the ambient rockmass:  $\Delta$ ,  $\Delta$ ,  $\Delta$  F are the strain and stress drops during the instability,  $\Delta$  E is the energy released during the instability.

As the system gets close to the instability point, it is sensitive to small perturbations, e.g. to sudden removal of small stressed portions of rock or to the velocity field of kinetic energy imparted by transient waves.

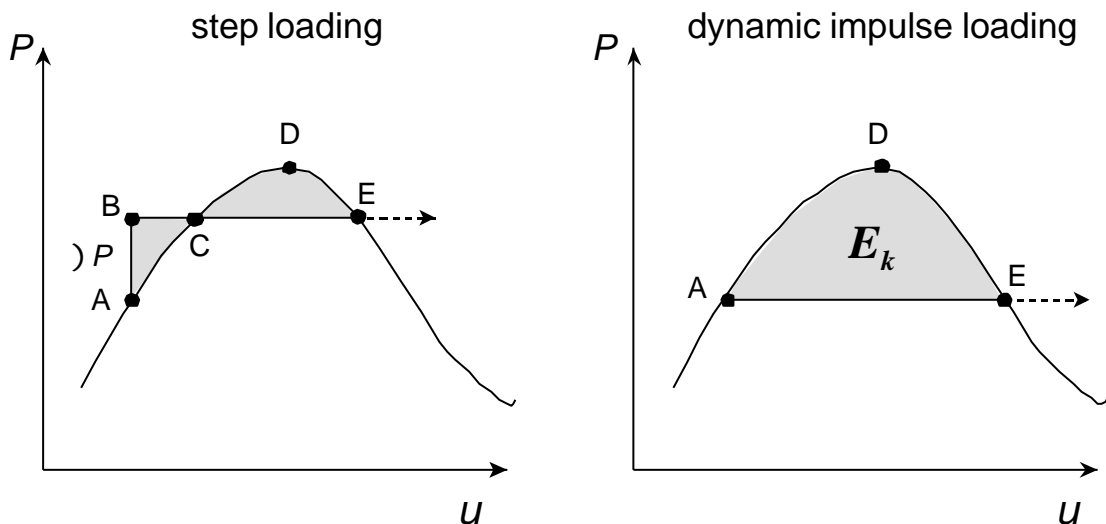


**Figure 2.2** Load displacement diagrams with step loading  $\Delta$  P and dynamic impulse of kinetic energy  $E_k$ . The system will become unstable if energy = area ABC > CDE for step loading or if  $E_k > ADE$  in case of dynamic loading



At each mining and/or time step a new incremental solution is sought,

$$Kdu = dP, \quad (2.3)$$

where  $K$  is global stiffness matrix,  $*u$  and  $*P$  are the increments of nodal displacements and forces, respectively. The instability point is specified by

$$\det(K) = 0 \quad \text{or} \quad \int dsd \in dV = 0. \quad (2.4)$$

Note that close to instability point variations in stiffness are large. Such static approach stops at the point of instability and offers no insight into the failure mode.

This approach is conducive to integration of numerical modelling with seismic monitoring since one can compare the expected changes in system stiffness predicated by the model with the observed change in seismic stiffness – see Chapter 6 for examples.

## 2.2. Dynamic analysis of stability – phase space

To gain insight into post critical behaviour of the system and its modes of failure it is more natural to undertake the dynamic analysis of stability. Instead of static equilibrium conditions one needs to consider equations of motion

$$M_{ij}\ddot{u}_j + C_{ij}\dot{u}_j + K_{ij}u_j = P_i(t) \quad (2.5)$$

where  $M_{ij}$ ,  $C_{ij}$  and  $K_{ij}$  are mass, damping and stiffness matrices respectively.  $P_i$  is a column matrix of applied forces and  $u_j$  are generalised displacements,  $i, j = 1, 2, \dots, n$ . By introducing new variables  $Y_1, Y_2, \dots, Y_n$ ,  $N = 2n$ , such that  $Y_{2i-1} = u_i$ ,  $Y_{2i} = \dot{u}_i$  one can convert the equations of motion into a system of first order differential equations,

$$M_{ij}\dot{Y}_{2j} + C_{ij}Y_{2j} + K_{ij}Y_{2j-1} = P_i(t) \quad (2.6)$$

Multiplying by the inverse  $M_{ij}^{-1}$  one can obtain a system of  $2n$  first-order differentiated equations in the canonical form

$$\dot{Y}_k = F_k(Y_1, Y_2, \dots, Y_N, t), \quad k = 1, 2, \dots, N \quad (2.7)$$

Since the stiffness and damping coefficients may depend on displacements, functions  $F_k$  may, in general, be nonlinear. The  $N$ -dimensioned space of variables  $Y_1, Y_2, \dots, Y_N$  is called the phase space.

The stability of a nonlinear system is defined by its response to change in the initial conditions, e.g. when the initial values  $Y_k^0$  are slightly changed to  $Y_k^0 + v_k^0$ . The solution may then be written as

$$Y_k^0(t) = Y_k^0(t) + v_k^0(t) \quad (2.8)$$

If for an arbitrary positive number  $\epsilon$  there exists a positive number  $\delta$  such that every solution with initial values  $|v_k^0| \leq \delta$  satisfies the  $|v_k(t)| < \epsilon$  for all times  $t > t_0$  the solution  $Y_k^0(t)$  is said to be stable. In other words a system is stable if a small change to the initial conditions leads to a small change in the response Figure 2.3 demonstrates the behaviour of a linear system, an oscillator, for which  $u$  = deviation from the static equilibrium position, and  $\dot{u}$  is velocity.

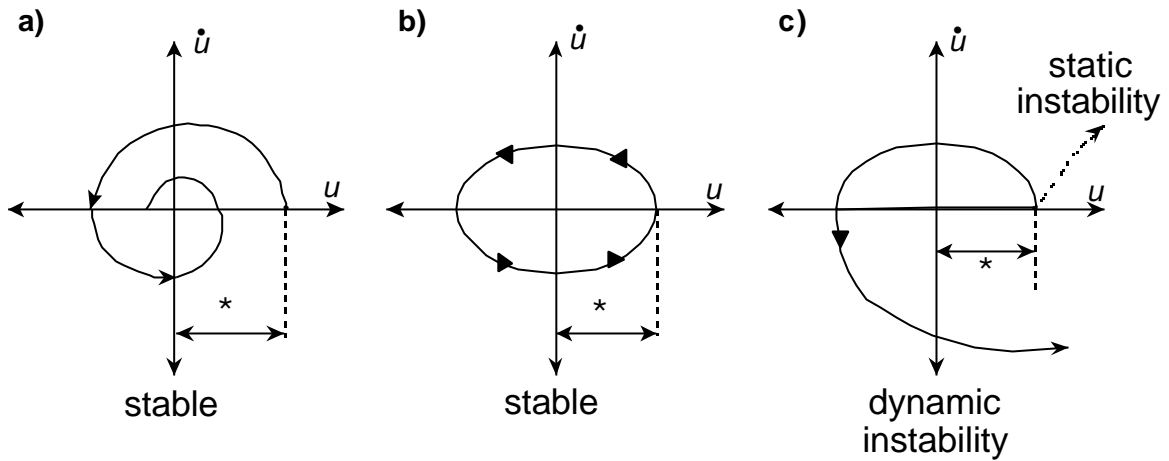


**Figure 2.3 Stable (a, b) and unstable (c) responses in the phase space.**

If the system is damped, the motion after the imposed displacement  $*$  brings it back to the original position of equilibrium. If the system is not damped the motion ensures with  $u$  and  $\dot{u}$  being always limited. If the stiffness of the system becomes negative, a static instability is produced and if the damping becomes negative a dynamic instability is generated.

The phase space trajectories associated with different types of stress-strain behaviour is shown in Figure 2.4 (Radu and Mendecki, 1997). An unstable modes i.e. divergent trajectories are induced by the negative stiffness or softening of deformation. In general the more phase space the system's trajectory can explore within a given time the more unstable it is.

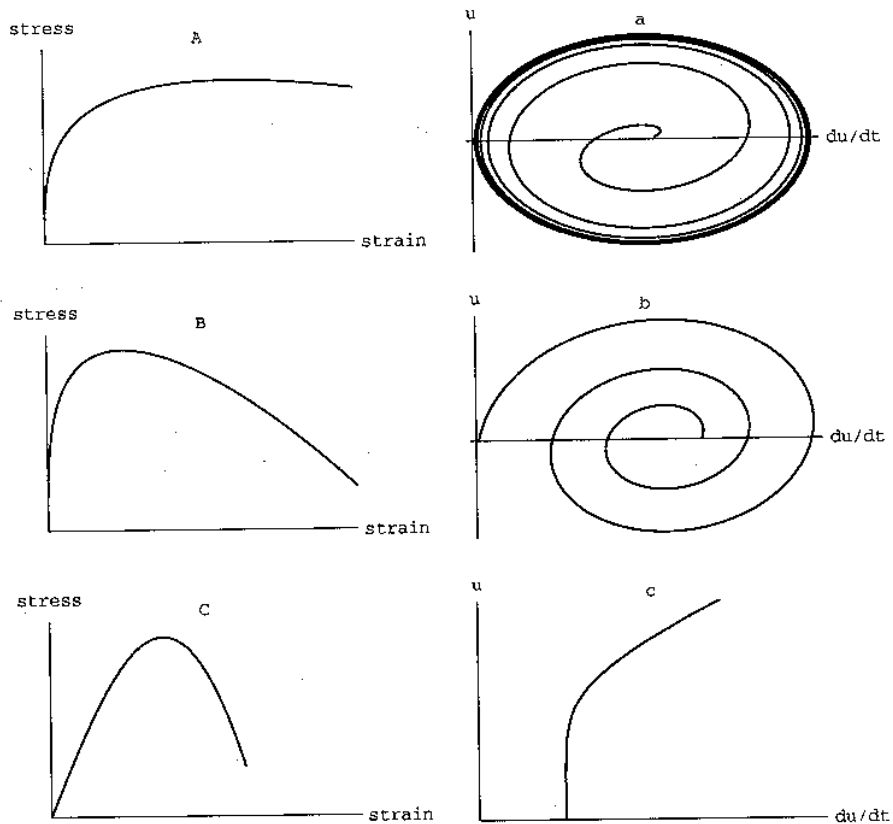


**Figure 2.4 Trajectories in phase space for plastic deformations**

The average rate of divergence of phase space trajectories is measured by the Lyapunov exponent,  $\lambda$ ,

$$\lambda = \lim_{t \rightarrow \infty} \left( \frac{1}{t} \right) \ln \left( \frac{d(t)}{d(0)} \right), \quad (2.9)$$

where  $d(0)$  and  $d(t)$  represent initial and current distances, respectively, between two neighbouring trajectories in certain directions. There are as many real Lyapunov exponents as there are degrees of freedom.

The change of energy in dynamical systems can be measured by the change of volume occupied by motion trajectories, corresponding to different initial conditions, in phase space.

$$\text{div } Y(t) = \lim_{t \rightarrow \infty} \left( \frac{1}{t} \right) \ln \left| \frac{\Delta v(t)}{\Delta v(0)} \right| = \sum_i \lambda_i \quad (2.10)$$

where  $v$  is the volume in the phase space. In conservative systems  $\sum \lambda_i = 0$ .

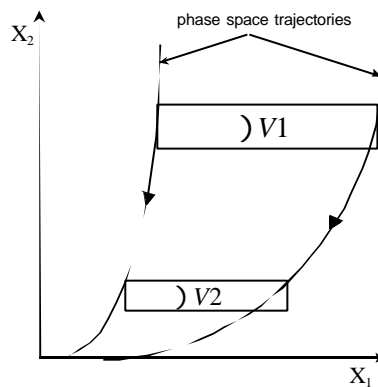


**Figure 2.5 Phase space volume contraction experienced by dissipative system;  $X_1$  and  $X_2$  are macroscopic state variables.**

In the three dimensional phase space a small rectangular volume  $l_1, l_2, l_3$  of initial conditions would evolve in time as

$$\Delta V(t) = l_1 l_2 l_3 \cdot \exp[t \cdot (\lambda_1 + \lambda_2 + \lambda_3)] \quad (2.11)$$

A dynamical system will be dissipative if  $\sum \lambda_i < 0$ . The dissipativity of a dynamical system with  $n \geq 3$  does not exclude the possibility that some of the Lyapunov exponents are positive. The complexity of the system behaviour is driven by the coexistence of two conflicting phenomena: dissipation,  $\lambda_i < 0$ , which contracts the volume occupied by the motion trajectories, and instability,  $\lambda_{n-i} > 0$ , which diverges these trajectories in certain directions. Thus the positive Lyapunov exponents severely limit the predictability of the motion along the expanding directions, whereas it is recovered along the contracting directions.

It is postulated here that the rate of phase space volume contraction is a measure of the relative softening of the system.

## 2.3. Phase space reconstruction and Lyapunov exponents

The Lyapunov exponents, in general cannot be analytically expressed via the parameters of the dynamical system. It is however, possible to estimate them from the time series generated by the system. To gain insight into the nature of the dynamics of seismic rockmass response to mining, the methodologies and procedures were adopted to reconstruct its phase space from data provided by the existing seismic networks in mines.

A time series can be thought of as a sequence of observations  $s(t)$  of a dynamical system, say  $s(t) = M(t)$ , where  $M(t)$  is a scalar moment of a seismic event that occurred within the volume of interest  $V$  at the time  $t$ . The volume  $V$  should not be much larger than the  $L^3$  where the  $L$  is the characteristic size of the larger event analysed. Given a delay time  $J$  and the embedding dimension  $d_E$  one can unfold a multidimensional effective phase space in time delayed co-ordinates

$$S(t) = [s(t), s(t - J), \dots, s(t - (d - 1)J)].$$

The delay vectors of sufficient length can recover the full geometrical structure of the underlying dynamics of the process including its Lyapunov exponents. The time delays were estimated from the minimum of the mutual information – it measures the deviation of the process from an uncorrelated one (*Fraser and Swinney, 1986*). The embedding dimension was estimated using false nearest strands approach (*Kennel and Abarbanel, 1995*).

Since the results of the embedding are frequently polluted by noise the following noise reduction algorithm has been applied:

- Find a low-dimension approximation of the attractor-phase space trajectories  $s(t)$ ,
- Project each point  $s(t)$  on the trajectory orthogonally onto the approximation to the attractor to produce a cleaner vector  $\bar{s}(t)$ ,
- Convert the sequence of cleaned vectors back into the scalar time domain to produce a cleaned time series.

The detail of the denoising procedure can be found in *Grossberger et al. (1993)*, or in *Schreiber and Richter (1998)*.

The following table presents the data sets selected for phase space embedding and results of the Lyapunov exponent calculations reflecting the rate of change of phase space volume.

Site	Average $\Sigma I$ and $(\mathbf{8}_{max})$
<ul style="list-style-type: none"> <li>• 7 polygons at WH4#, which due to the shallow depth presents of weak geological structures, lack of stabilising pillars and extensive mined-out areas, were considered as being of lower stiffness</li> </ul>	-2.84 (2.84)
<ul style="list-style-type: none"> <li>• 11 polygons at WDL, mainly Carbon Leader West, which, due to great depth, lack of larger faulting, the presence of stabilising pillars were considered as being the stiffer system than that of WH4#</li> </ul>	-0.15 (0.14)
<ul style="list-style-type: none"> <li>• Large portions of Deelkraal (DKL) and Elandsrand (ELD), both with similar geology but different mining layouts; longwalls without stabilising pillars at DKL thus considered a softer system than that of ELD with sequential grid mining.</li> </ul>	-1.09 (0.12) -0.59 (0.11)

In general the more homogenous and stronger the rock, the higher is its stiffness when subjected to external loads and the lower its dissipation rate as measured by the sum of Lyapunov exponents. In addition the predictability of an unstable behaviour seems to be limited by the system stiffness. Softer systems spending more time beyond the bifurcation phase, have a tendency to develop coherent, easier recognisable spatio and/or temporal structures and thus render themselves more predictable, e.g. the highest success rate in predicting rockmass

instabilities has been experienced in the Free State gold mines which are relatively “soft” compared to those on the Far West Rand.

## 2.4. Spatial and temporal gradients

The contouring of seismic event and seismicity parameters is a practical tool to delineate a variety of seismicity patterns (GAP017). During the GAP303 research we investigated the addition of spatial and temporal gradients to the contouring of particular seismicity parameters (1996 reports). High temporal and spatial gradients in seismicity parameters are important indicators of seismic hazard. A relatively simple procedure to capture such gradients in contour maps of seismicity parameters requires the normalisation by the average time or the average distance between consecutive events. This often highlights particular anomalies as being more significant than others. Results of extensive analyses were given in the 1996 year end report. As an example, we note that local clustering of seismic activity in time and/or in space can relatively easily be accounted for when computing average values of different parameters quantifying seismicity. Let  $S$  represent the parameter of interest, say:

$\Omega = \epsilon_S, s_S, K_S, h_S, D_S(\Delta V, \Delta t)$ , then the local space and/or time clustering of  $S$  can be expressed as

$$C(\Omega; \bar{X}, \bar{t}) = \Omega / (\bar{X} \cdot \bar{t}),$$

where  $\bar{X}$  and/or  $\bar{t}$  would cater for the local spatial and/or temporal clustering of seismic activity - see Figure 2.6 as an example.

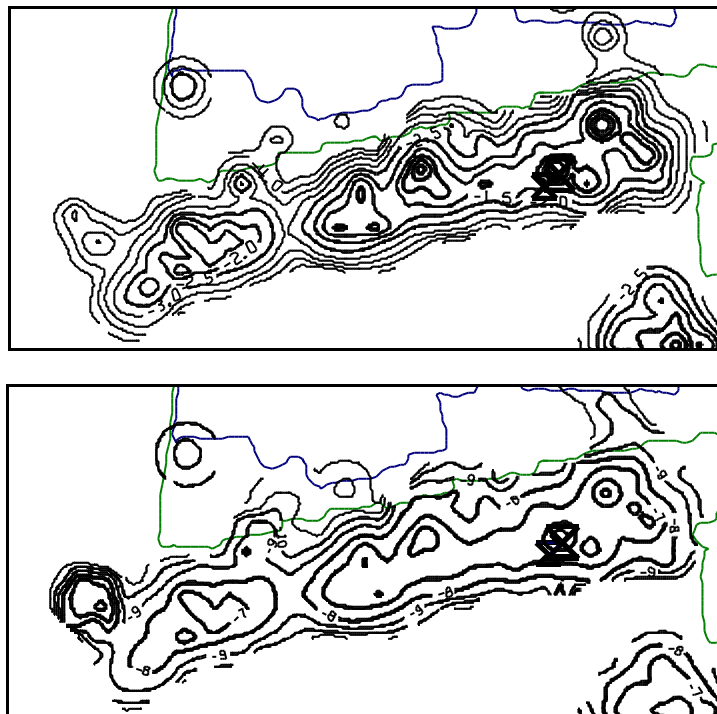


**Figure 2.6** In the top figure contours of  $\log D_S$  of one month's data of seismic response to longwall mining in a South African gold mine are shown. One can distinguish at least four areas of high gradient with  $D_S$  as high as  $0.5$  to  $1 \text{ m}^2/\text{s}$ . One of these areas attracted two larger seismic events, marked by the hourglass symbols, a day later. The bottom figure shows contours of  $C(D_S; \bar{t}) = D_S / \bar{t}$  in  $[\text{m}^2\text{s}/\text{s}]$ , where seismic diffusivity is divided by the local average time (over grid size) between seismic events  $\bar{t}$  the two larger events which subsequently occurred located in the area of the maximum  $D_S / \bar{t}$ .

## 2.5. Differential maps

The objective of differential maps is to delineate the areas or volumes of significant changes in the parameter of interest over time. It may help to identify hot spots, i.e. areas/volumes of undesirable rock mass response to mining, for more detailed time domain stability analysis.

Differential maps are presented as contour lines in 2D or surfaces in 3D of equal difference in a given parameter between two periods of time, say  $\Delta t_2$  and  $\Delta t_1$ , over the same area or volume of interest. For routine analysis it is advisable that  $\Delta t_2$  and  $\Delta t_1$  be equal and consecutive. The grid spacing, hence the spatial resolution of the map, is a function of location accuracy and the network's sensitivity - the lower  $m_{min}$  the better the spatial coverage by small events.

Differential maps may be used to reconcile the results of numerical modelling with those of quantitative seismic monitoring, i.e. the expected percentage changes in stress and/or strain related parameters predicted by time step modelling can be compared qualitatively and quantitatively with percentage change in the relevant observed seismic parameters. Back-analysis of stable and unstable cases would generally assist in validating the procedure before routine use.

## 3. System stiffness and seismic hazard

### 3.1. Size distribution hazard

In general seismic hazard relates to the potential for strong ground motion resulting from the occurrence of seismic events. Seismic hazard is defined as the probability of occurrence of an input, i.e. seismic event or ground motion, equal to or exceeding a specified level, within a given period of time.

The general procedure followed in evaluating hazard includes the determination of the volumes that produce seismicity, estimating the recurrence times of seismic events of different magnitudes and, taking into account the local attenuation of ground motion, computing the probability of exceeding a given level of ground motion for different time intervals. The results may be presented as a table of probability of each level of ground motion for a given site or as contours of different levels of ground motion at a given level of probability. Seismic hazard estimates in mines are frequently limited to probabilities of occurrence, or recurrence times, of seismic events above certain magnitudes  $Tr(\geq m)$ , so the relative exposure to seismicity and seismic risk could be quantified.

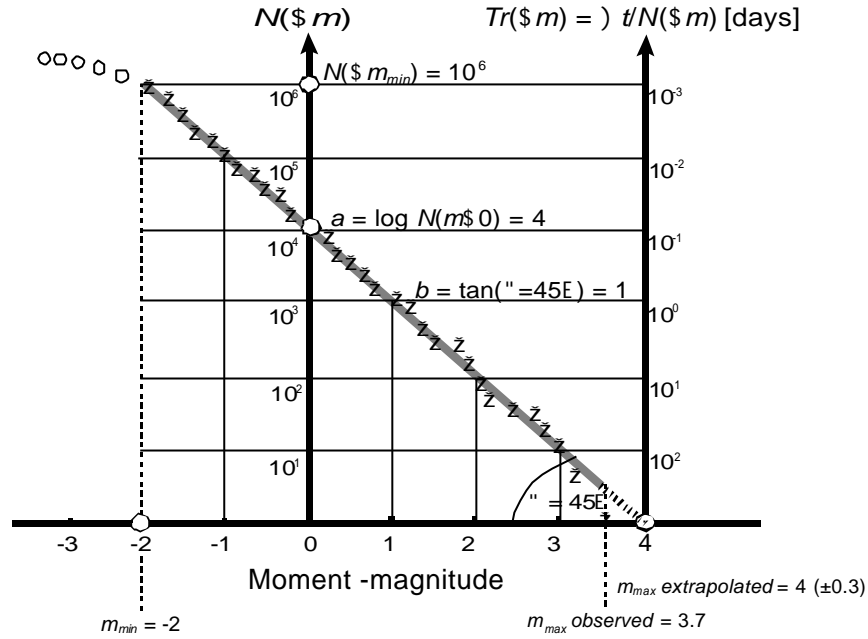


**Figure 3.1** An illustrative plot of cumulative frequency-magnitude with  $m_{min} = -2$ ,  $a = 4$  and  $b = 1$  for the volume  $V$  over the time period  $t = 1000$  days. Open dots below  $m_{min} = -2$  denote data points below the network's sensitivity that should not be used in parameter estimation.

The probabilistic recurrence times can be derived from different modifications of the empirical Gutenberg-Richter relation describing the frequency-magnitude distribution of small and intermediate size earthquakes,

$$\log N(\$m) = a - bm, \quad (3.1)$$

where  $N(\$m)$  is the expected number of events not smaller than magnitude  $m$ , and  $a$ ,  $b$  are constant - see Figure 3.1. The Gutenberg-Richter relation implies a power law distribution i.e. the absence of a characteristic size, and as a consequence, puts no limit on the maximum earthquake size. Thus if the distribution of large earthquakes is also a power law, then it must have an exponent that is larger than that for smaller ones.

The mean recurrence times can be calculated as  $Tr(\geq m) = \Delta t / N(\geq m)$ , where  $t$  is the period of observation. The one largest seismic event, called here  $m_{max}$ , would have a magnitude that corresponds to  $N(\$m_{max}) = 1$ , or  $\log 1 = a - bm_{max} = 0$ , thus  $m_{max} = a/b$ , or

$$m_{max} = m_{min} + (1/b)\log N(\geq m_{min}), \text{ with uncertainty } dm_{max} = \pm 0.3 / b. \quad (3.2)$$

Parameter  $a$  measures the overall occurrence rate and scales with the rate of rockmass deformation  $\dot{\epsilon}$  as  $a = \log \dot{\epsilon} + \text{constant}$ . The parameter  $b$  is controlled by the distribution of events between the higher- and lower-magnitude ranges and, for large and well distributed data sets, can be estimated from  $b = 0.43(\bar{m} - m_{min})^{-1}$  with uncertainty  $db = \pm b\sqrt{n}$ , where  $\bar{m}$  is the mean of the observed magnitudes and  $n$  is the number of observations. Both parameters influence derived recurrence times, therefore it is essential that their values and variances be determined accurately. The basic assumptions made when calculating the probabilistic

recurrence times are that  $N(m_{max}) = 1$  and the parameters  $a$  and  $b$  do not change significantly with time and within the selected volume  $V$ .

The quantification of seismic hazard based on the Gutenberg-Richter relation would require at least two parameters since the relation itself is defined by two: the  $a$  and  $b$  values. One way to capture the full seismic hazard in a single number is by way of the volume of ground motion (end 1997 report). The volume of ground motion defines the total volume of the rock mass affected by peak velocities of ground motion exceeding a given value. It is a single number representing several parameters, namely  $a$ ,  $b$ ,  $m_{max}$ , minimum magnitude at which to expect damage and an empirical relation between PPV, magnitude and distance:

$$VGM = \frac{A n^c b N}{Q} \frac{e^{-Qm_0} - e^{QX_{max}}}{e^{-bm_{min}} - e^{-bm_{max}}} \quad (3.3)$$

where

- $A = (4p/3) \exp(-3A_3/A_2)$
- $c = 3/A_2$
- $Q = b + (3A_1/A_2)$
- $A_1 = a_1 \ln 10$ ,  $A_2 = a_2$ ; and  $A_3 = a_3 \ln 10$  in the formula:  
 $r \log_{10}(n [mm/s]) = a_1 m + a_2 \log_{10} r [m] + a_3$ , where  $n$  is peak ground velocity in [mm/s],  $r$  is distance from the source in [m], and  $m$  is magnitude measured from the seismic energy using the formula  $m = d \log_{10} E [J] + f$  (frequently used values for the coefficients are  $a_1 = 0.8$ ,  $a_2 = -1.9$  or  $-1.8$ ,  $a_3 = 3.4$ ,  $d = 0.526$  and  $f = -1.16$ )
- $b = b \ln 10$ , where  $b$  is the  $b$ -value in the magnitude-frequency relationship  $\log_{10} n = a - bm$  (or  $n = e^{a-bm}$ ,  $a = a \ln 10$ ), with  $n$  being the number of events with magnitudes larger than  $m$
- $m_{min}$  is the minimum magnitude above which the magnitude-frequency relationship of a straight line in a log-log scale whose slope provides the values for  $b$  (or  $a$ )
- $m_{max}$  is the maximum magnitude, either calculated as  $m_{max} = 2X_{max-1} - X_{max}$ , where  $X_{max}$  and  $X_{max-1}$  are the maximum observed magnitude and the last but one maximum observed magnitude, respectively; or  $X_{max}$  is used instead of  $m_{max}$
- $m_0$  is the minimum magnitude of damage
- $N = n(m_{min})$  is activity rate, ie., the number of events with magnitudes exceeding  $m_{min}$ ; it is either taken from the observed data for the study period or time, or is calculated from the magnitude-frequency relationship as  $N = \exp(a - bm_{min})$

Another way of expressing seismic hazard in a single number is to estimate the total number of events in the different magnitude ranges and summing their moments (or energies). The estimated number of seismic events within the magnitude range  $m_1$  and  $m_2$ , where  $m_1 < m_2 \leq m_{max}$ , is  $N(m_1 \leq m \leq m_2) = N(m_1) - N(m_2)$ , and the cumulative moment release, EM, by all these events can be estimated from

$$\Sigma M = 0.43 \cdot 10^{a+9.1} \left( 10^{m_2(1.5-b)} - 10^{m_1(1.5-b)} \right) / (1.5 - b), \text{ for } b < 1.5. \quad (3.4)$$

In the long term the sum of seismic moments is proportional to the volume mined,  $V_m \cdot EM \cdot GV_m$ . Thus, for a given  $V_m$  the higher the values  $a$  and  $b$  of the Gutenberg-Richter relation the lower the  $m_{max}$ . The hazard magnitude  $Hm$  is then defined by  $Hm = (2/3) \log \Sigma M - 6.1$ , where  $GM$  is estimated by equation (3.4).

The specific model of the frequency-magnitude relation and the numerical procedures used in its parameter estimation should account for the upper limit of possible maximum magnitude in the area of interest, slow temporal changes in  $b$ , and for the fact that magnitudes are not continuous but discrete grouped quantities determined, in mines, with accuracy of 0.2 units on average. For more details see GAP 303, 1996 Report.



If one assumes that the time of rupture of larger events is controlled by strong and highly stressed areas within the volume  $V$ , the recurrence time  $T_r$  should then be calculated on the basis of frequency - magnitude data selected from these areas only, as determined by the contours of energy index or seismic stress and/or modelled stress, instead of from the entire volume.

The most significant deviations of observations from the frequency-magnitude relation are those at the largest observed magnitudes, since they may influence the expected recurrence time for the maximum magnitude event. In general, recurrence times beyond the time span of the data set  $t$  should be treated with caution.

In addition, it is useful to know the distribution of actual recurrence times about the estimated mean. Given the mean, the type of distribution, the standard deviation of the observations and the time of occurrence of the last event, either cumulative probability, i.e. the probability that an event would already have happened, or future conditional probability may be estimated. Failing that, one can evaluate the best estimate of the empirical probability  $P_T$  that a given volume  $V$  will produce an event of magnitude greater than  $m$  within a specific time  $T$  after the preceding event of this size (Savage, 1994). Given the latest  $n$  observed recurrence intervals  $Tr(\$m)$ , of which  $n_T$  are smaller than or equal to  $T$ ,

$$P_t = (n_T + 1)/(n + 2), \text{ with uncertainty } dP_T = \pm 2\sqrt{P_T(1 - P_T)/(n + 3)} \quad (3.5)$$

For larger data sets,  $dP_T$  approximates the 95% confidence interval. For example, consider a sequence of the last 15 recurrence intervals in days, for events with  $m$  \$ 3.0 in one of the mining areas in South Africa: 86, 33, 118, 58, 31, 107, 61, 77, 10, 17, 8, 13, 4, 26, 4. Then, the empirical probability that this area will produce an event with  $m$  \$ 3.0 within, say,  $T = 90$  days of the preceding one is  $P_{90} = 0.82$  with  $dP_{90} = \pm 0.18$ , which could be considered reasonably significant. For the same data set,  $P_{30} = 0.47$  with  $dP_{30} = \pm 0.23$  would not be considered significant.

### 3.2. Seismic hazard and system stiffness

In general the  $b$ -value is influenced by the following characteristics of the geomechanical system under consideration:

- the stiffness, i.e. the ability to resist deformation with increasing stress
- the level of stress
- the rockmass heterogeneity.

The stiffer the system the higher the  $b$ -value. This observation does not contradict reports on decreasing  $b$ -value with increasing stress, since there is a general loss of stiffness with increasing stress during a strain hardening regime. In the absence of a significant tectonic stress, intermediate and large seismic events usually occur after considerable mining has taken place in the area, degrading the stiffness of the system.

The rock mass heterogeneity is defined by the spatial distribution of sizes and distances between strong and/or stressed and weak and/or destressed patches of rock where seismic sources may nucleate and be stopped. In general, for the same stiffness, an increase in rock heterogeneity results in a higher  $b$ -value, since it is more likely that an initiated rupture be stopped by a soft or hard patch before growing into a larger event.

The observed data sets of mining related seismicity frequently exhibit fairly complex behaviour. The frequency-magnitude distributions of seismic events associated directly with tunnel development, or mining excavations and those related to geological features of different sizes may have different forms, and when superimposed may affect the estimated recurrence times of larger events. In addition, the relatively subjective choice of volume(s) of interest, the range of

spatial and the degree of temporal correlation of seismic activity and the availability and quality of data may also influence the results. Therefore many data sets could be considered anomalous, having either a peculiar b-value, i.e. outside  $0.5 < b < 1.5$ , and/or strongly deviating from the Gutenberg-Richter model. In such case it is important to determine the physical factors affecting the distribution and ensure that the interpretation is offered in the context of the specifics of the data set.

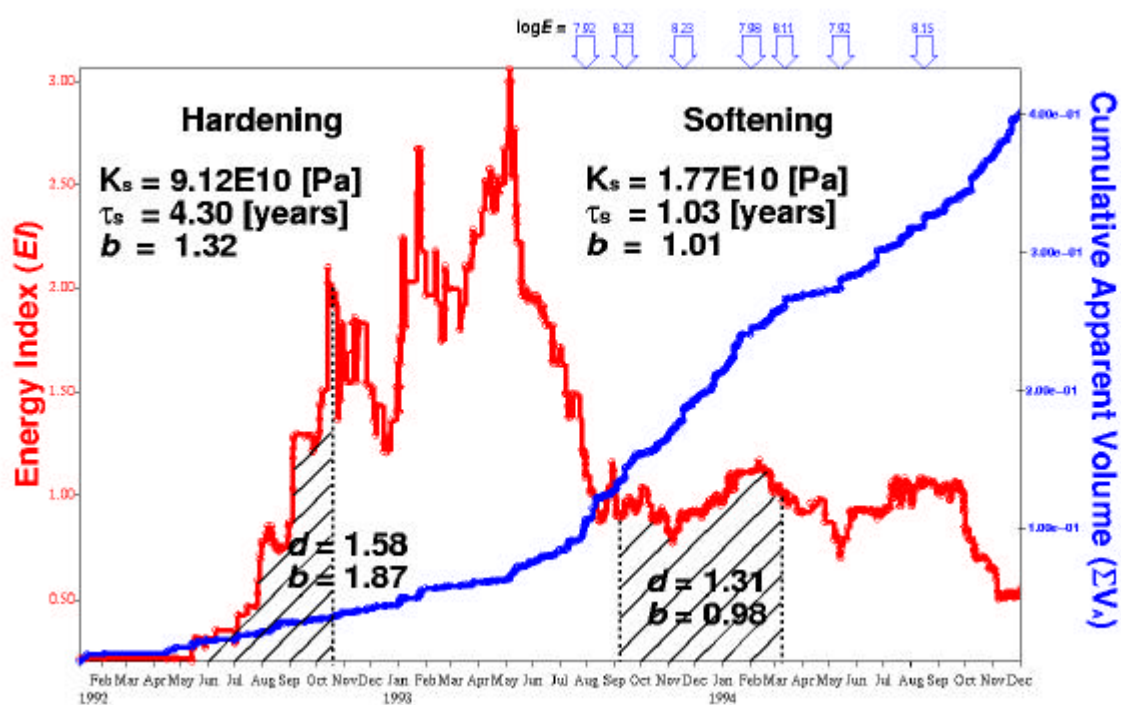


**Figure 3.2** Time history of cumulative apparent volume,  $\Sigma V_A$ , and energy index,  $E_I$ , for the seismicity associated with pillar mining within the volume  $V = 5.12E7m^3$ . Note that all large seismic events,  $\log E > 7.5$ , occurred after the pillar had lost the ability to maintain stress. Note also the differences in d-value (slope of E-M relation) and in the b-value between two six-month periods, indicated by shading, of similar average energy index  $E_I$  but considerable difference in stiffness.

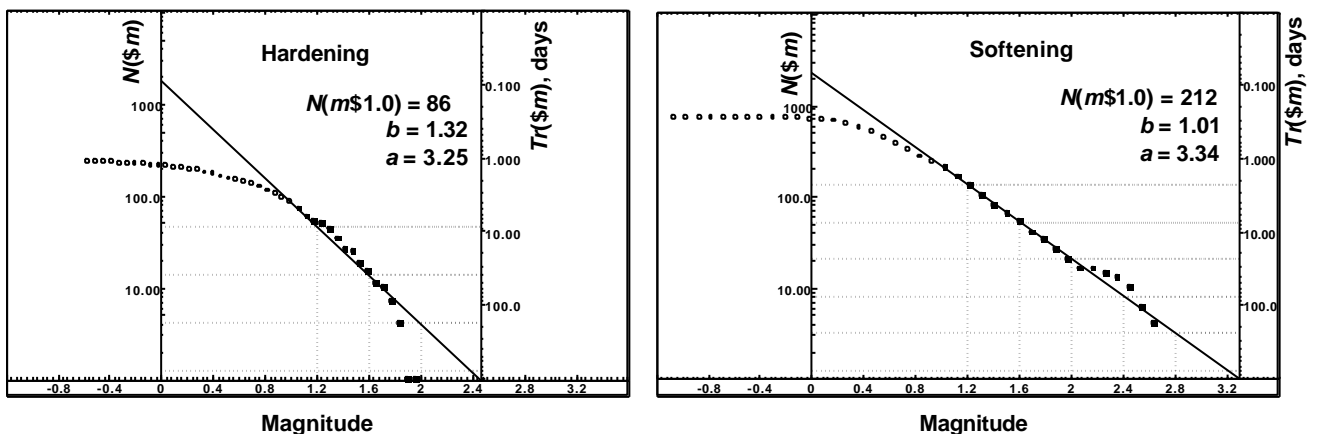


**Figure 3.3** The cumulative frequency-magnitude distributions for the period of January '92 to May '93 (hardening) and June '93 to December '94 (softening); note the characteristic misfit, i.e. the lack of larger events, between the data and the model during the overall hardening regime; note also a considerably higher hazard associated with larger seismic events during the softening period.

Rockmass subjected to mining is strongly influenced by excavations, pillars, induced fracture zones, and associated changes in stress. These induced heterogeneities influence the stiffness and the stress regimes of the system and thus the activity rate, size of the larger observed events and the  $b$ -value. For example, an introduction of strike stabilising pillars in the West Rand Region in 1980 and, recently, the sequential grid layout, both reduced the size of the largest events experienced compared to the traditional longwall mining. Figure 3.2 shows cumulative apparent volume vs energy index, size and the time-of-day distributions derived from seismic data recorded during shaft pillar extraction. Note the softening of the pillar during May 1993 manifested by persistent decrease in energy index  $EI$  associated with an increase in the rate of seismic deformation and associated changes in the size and time distributions.

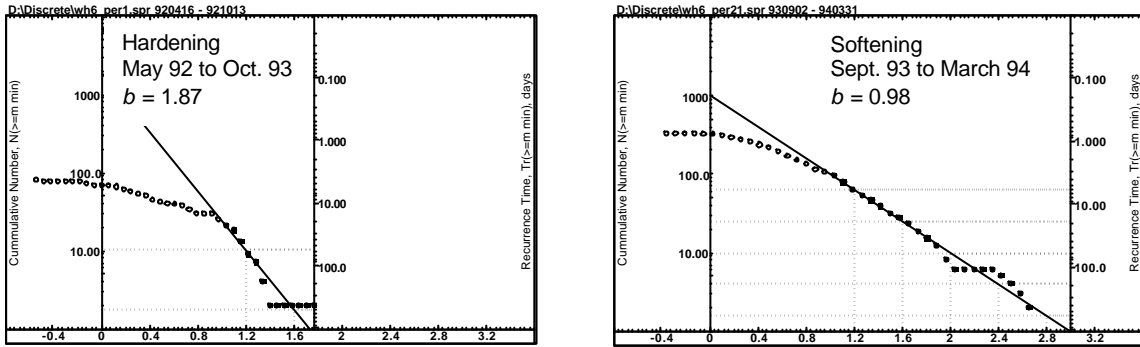


**Figure 3.4** As 3.3 but for two six-month periods, indicated by shading, at similar average  $EI$  but considerable difference in stiffness.

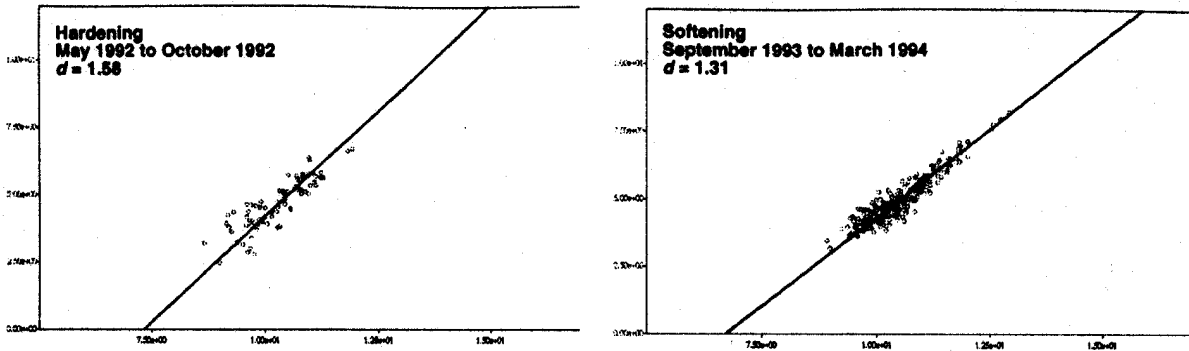


**Figure 3.5** The  $E$ - $M$  plots for two six-month periods, indicated by shading on Figure 3.2, of similar  $EI$  but considerable difference in stiffness; note the higher  $d$ -value and lower range of moments domain during May-October 1992.

Figures 3.2 to 3.6 illustrate the influence of system stiffness on size distribution hazard and on the nature of energy and moment release.

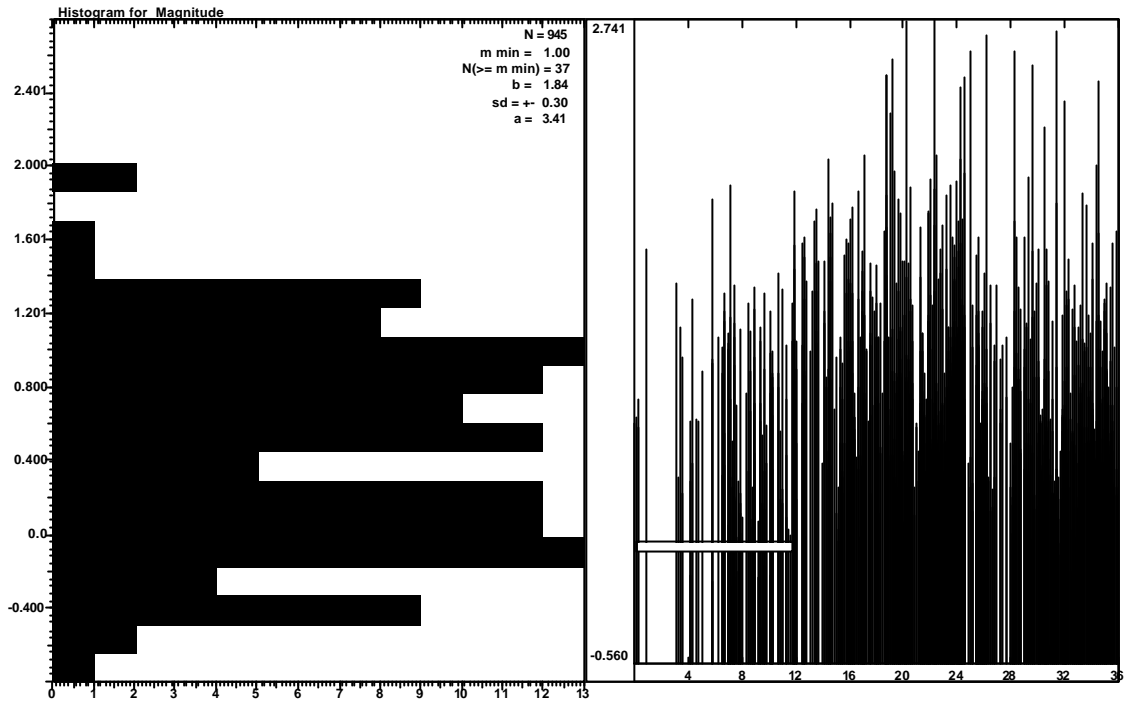


Figure 3.6a

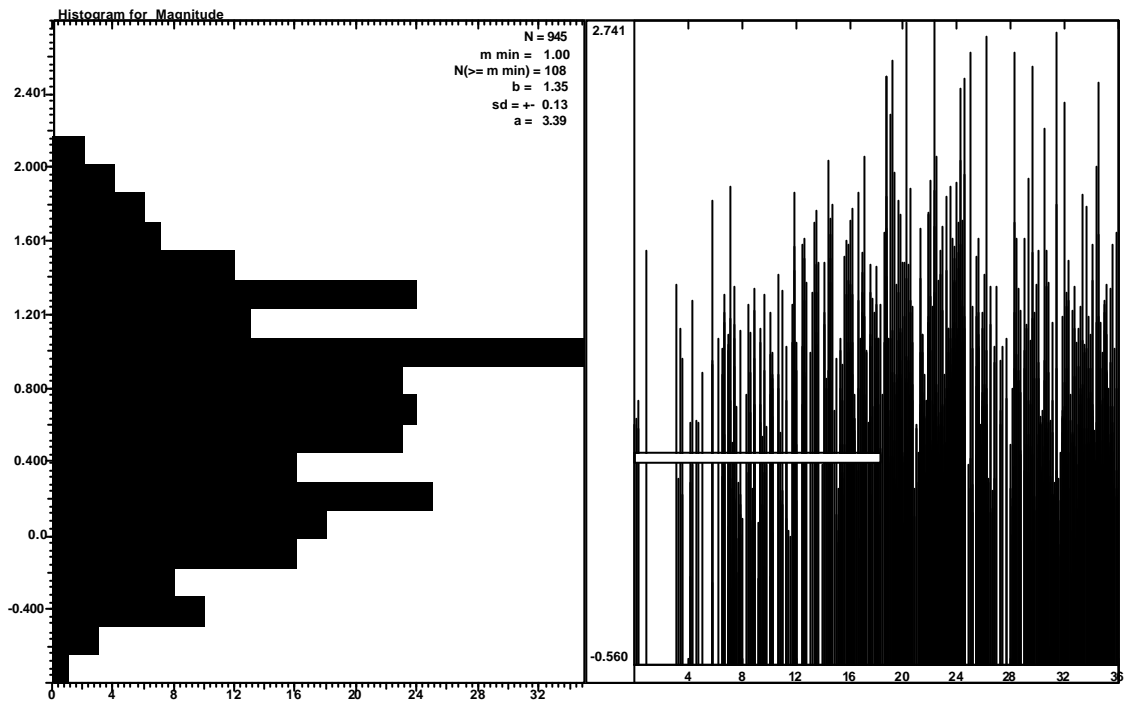


Figure 3.6b

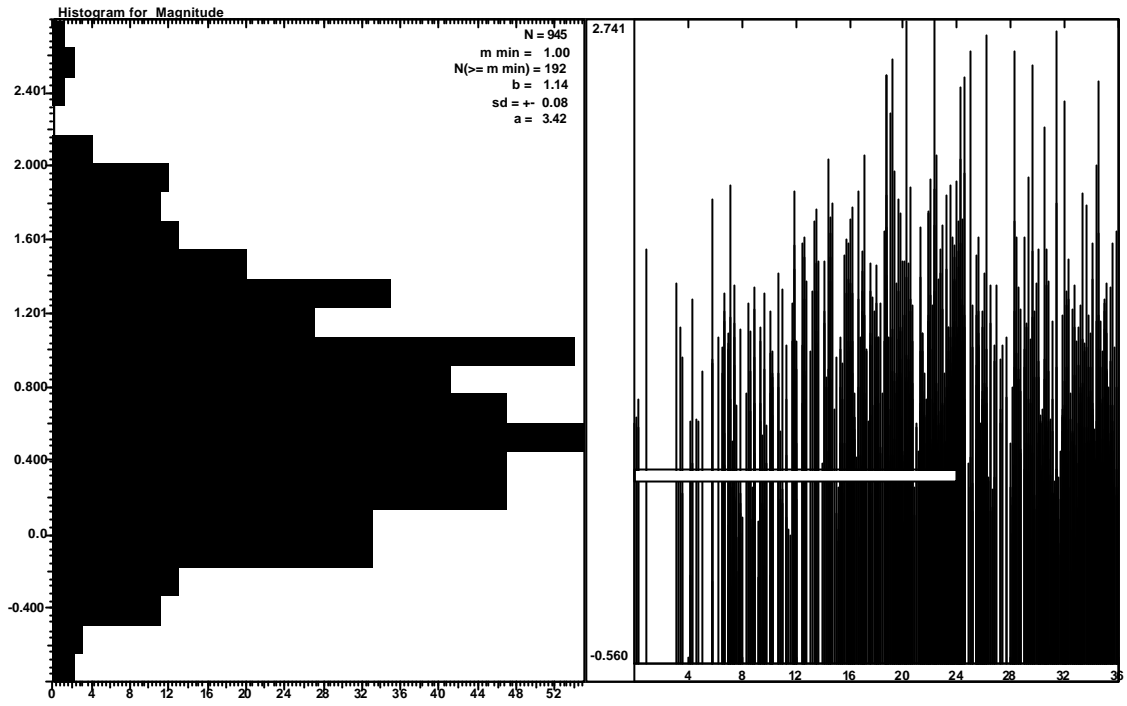


Figure 3.6c

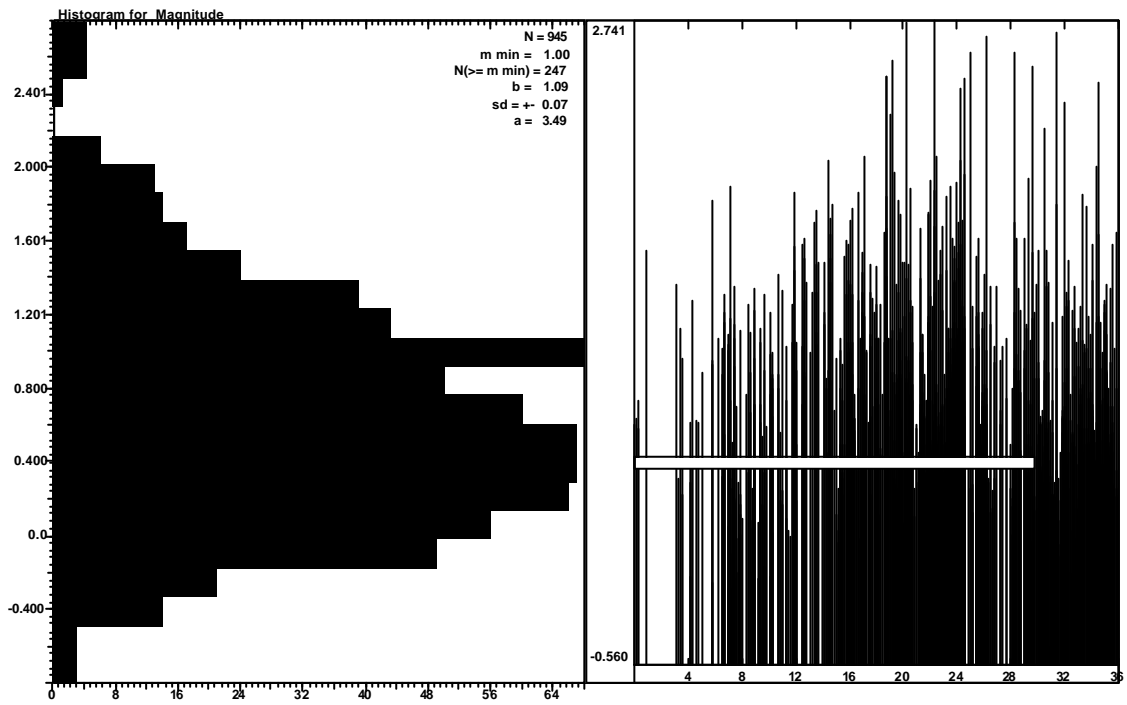
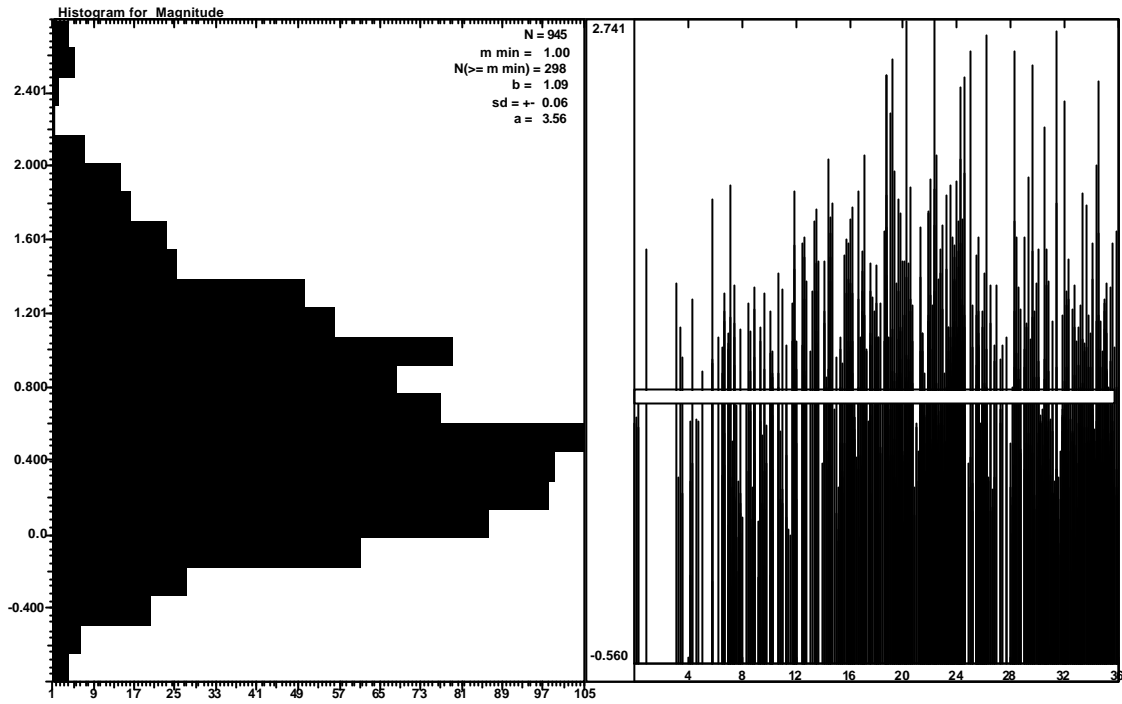


Figure 3.6d



**Figure 3.6e**

**Figures 3.6a-e Time distribution of seismicity by magnitudes during 36 months of mining WH#6 pillar (right). Magnitude histograms within overlapping windows, as indicated on the time plot, are shown on the left.**

### 3.3. Time of day distribution hazard

Seismic hazard derived from the size distribution of seismic events may not be adequate to quantify and to manage the exposure to seismicity, due to the differences in time of day distribution of intermediate and large events associated with different mining scenarios, Figure 3.7 as an example. In general stiffer systems/layouts are characterised by the lower  $m_{max}$  but by the time-of-day distribution with larger statistical dispersion,  $d(h, t_B) = (\sum |h_j - t_B|) / (t_B \cdot N)$ , thus they are less time-predictable, while softer systems have larger  $m_{max}$  but they trigger or induce most events during the few hours after blasting.

If  $\bar{t}(\geq m, t - t_B) = (t - t_B) / N(\geq m, t - t_B)$  is the average time between events with magnitude not smaller than  $m$  at the time  $t$  after the time of blasting  $t_B$ , then the probability of having an event of that size in a small time interval  $t + \Delta t$  is approximately  $P(\geq m, t - \Delta t) = \Delta t / \bar{t}(\geq m, t - t_B)$ .

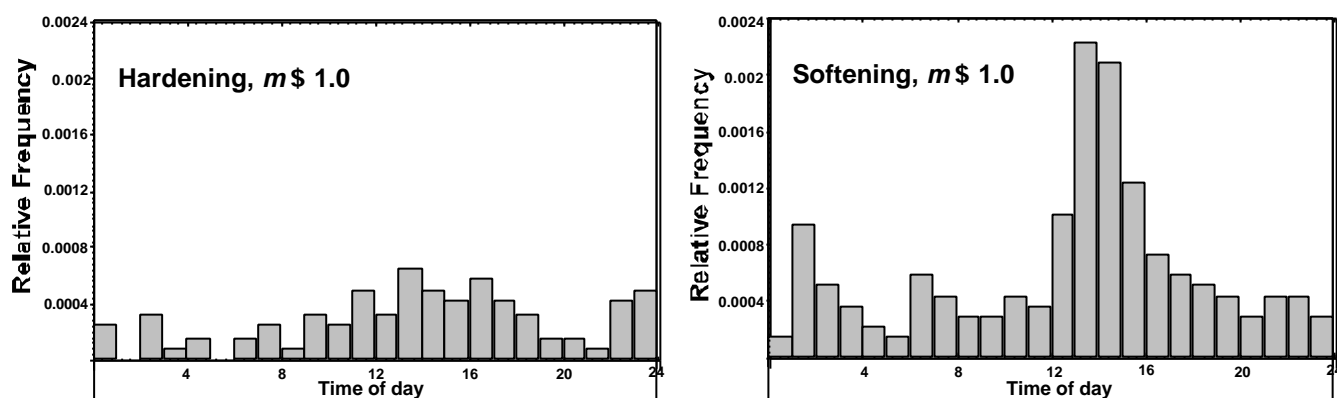


**Figure 3.7 The time-of-day distributions of seismic events with  $m = 1.0$  for the hardening and softening periods; note that hazard for  $m = 1.0$  at 23h00 until 01h00 and at 10h00 and 12h00 is higher during hardening.**

Seismic safety exposure at a given hour of day can be estimated by the product of the average frequency of potentially damaging events and the average number of people exposed at that time.

### 3.4. System stiffness, $E-M$ relations and seismic hazard

To describe the characteristics of a particular mine design in a single word, the term 'stiffness' is probably a good choice. By reducing closure, e.g. by leaving pillars or adding backfill, the 'system', comprising the mine openings plus the surrounding rockmass, is stiffened compared to the case with no support. By analogy to rock strength testing devices, a soft system can store energy and release it dynamically when the rock fails. A completely stiff system will crush the rock without violent failure. Seismically, a very stiff system will prevent large dynamic instabilities and the local crushing of rock will yield many small seismic events.

The notion here is that the Gutenberg-Richter b-value will increase and  $m_{max}$  will decrease with increasing stiffness. The results of the comparison of the 'stiff' mine layout of sequential grid mining with the 'soft' layout of longwall mining confirms this (Mendecki and van Aswegen, 1997).

Similarly the d-value defining the slope of the logE vs logM straight line fit, called the E-M relation, tends to correlate with the system stiffness - the stiffer the system the steeper the line and the higher the d-values. The E-M relation for the stiff system does not extend far into the large moment domain since it does not produce large events until its stiffness is degraded and

the d-value drops. For a given slope an increase in the c-value of the E-M relation reflects an increase in stress - the apparent stress of a typical event with  $M = 1\text{Nm}$ , or  $m = -6$ , would be  $s_A(M = 1) = \text{rigidity} * 10^c$ .

Figure 3.8 schematically illustrates the proposed interpretation. The evolution of mining induced seismic hazard could be seen as follows: Small events are associated with the initial development of the mining infrastructure and they define steep b and d slopes. As mine spans enlarge and the system softens, these slopes will decrease, the magnitude range will increase and so the general seismic hazard. By limiting the process of softening by means of stiff regional support systems, the size distribution seismic hazard can be lowered.

However, time of day distribution of seismicity associated with stiffer systems is less favourable than that of softer ones limiting the gain.

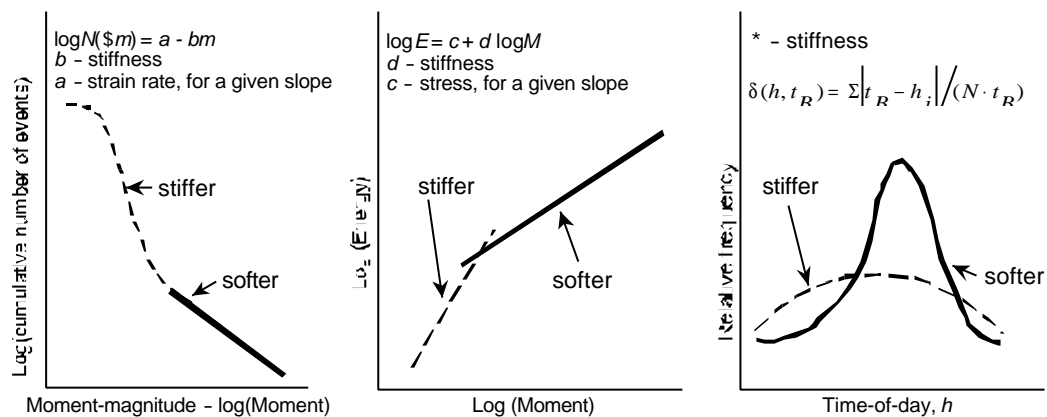


**Figure 3.8 An illustration of a cumulative frequency-magnitude plot of a mixed data set over a limited period of time (left). Events associated with a stiffer system (broken line) and with a softer system (solid line) frequently have different slopes. On a log Energy vs log Moment plot (centre) the same applies. Intermediate and larger events associated with softer systems tend to occur within a few hours of blasting time,  $t_B$ , while a stiffer system responds moderately but with larger statistical dispersion, as measured by the normalised standard deviation  $*$ , (right).**

In general, for the same extraction ratio, the higher the stiffness and the lower its spatial variance within the system, the better the layout. The  $d$ -value and seismic stiffness  $K_{s,,}$  could be used to monitor the effectiveness of such design. The challenge now is to develop numerical modelling methods which would allow the quantitative comparison of the overall system stiffness as well as the stiffness of specific volumes/ structures for the optimal design of mine layouts.



## 4. Modelled system stiffness – Theoretical concepts

### 4.1. Seismic Monitoring and System Stiffness

#### 4.1.1. Observations

Back analyses undertaken from the results of seismic monitoring yielded the comparative E-M plots shown in Figure 4.1.

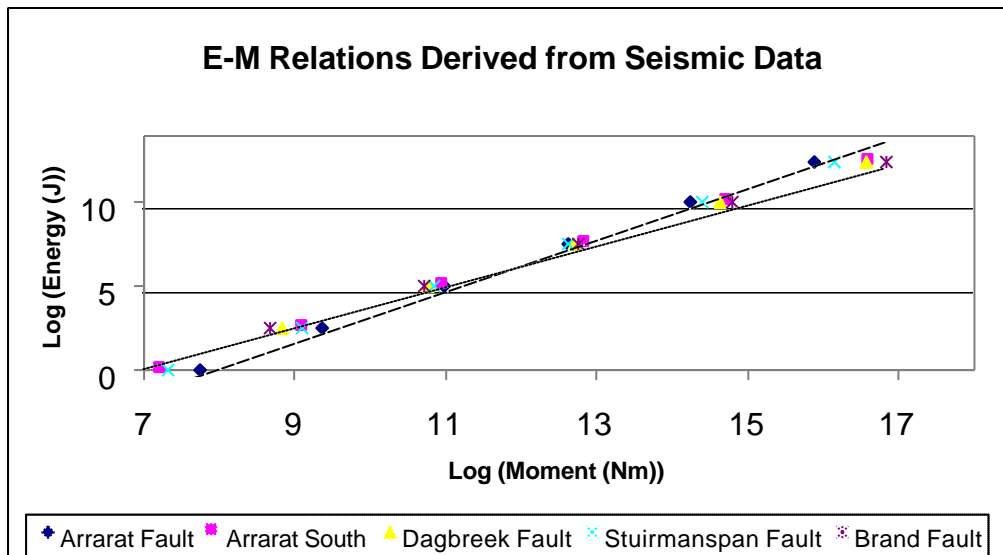


**Figure 4.1 E-M Relations Derived from Seismic Data**

In the above plot, the E-M Relations shown vary from the Arrarat fault to the Brand fault. It is noticeable that the comparative E-M plots shown in Figure 4.1 all define different E-M Relations, i.e. E-M Relations with varying slopes, levels and intercepts.

#### 4.1.2. Interpretation

The comparative change in slope and level of the E-M Relations shown in Figure 4.1 indicate that the individual events formulating the relations belong to different populations. A physical explanation for this variation is that the E-M Relation is a measure of system stiffness. A system is defined as a volume  $\Delta V$  of the rockmass. The volume  $\Delta V$  is inclusive of any geological structures and rock strength heterogeneity present, the geometrical mine layout within the volume, and any rock failure, strength reduction and subsequent inelastic deformation resulting within the rockmass or along the geological structures. System stiffness can be broadly defined as a measure of the system to resist deformation with increasing load. The system stiffness modulus will be defined by the slope of the stress versus strain plot of the system (where strain will consist of both its elastic and inelastic components).

Seismic stiffness is defined by *Mendecki et al (1999, pg 30)* as a measure of the system to resist seismic deformation with increasing stress. From quantitative seismology the seismic stiffness modulus for a given volume  $\Delta V$  and over a given time  $\Delta t$  is defined as (*Mendecki et al, 1999, pg 30*):

$$K_s (\Delta V, \Delta t) = \sigma_s / \epsilon_s = 4G^2 \Delta V \Sigma E / (\Sigma M)^2$$

Where:

$K_s$  = seismic stiffness modulus (Pa)

$\sigma_s$  = seismic stress (Pa)

$\epsilon_s$	= seismic strain	
G	= rigidity	(Pa)
E	= radiated seismic energy	(J)
M	= seismic moment	(Nm)

Thus, as per *van Aswegen and Mendecki (1998, pg 6)*, since the seismic moment generally represents the amount of co-seismic strain at the source, and the ratio E/M indicates the stress level at the source, the slope of the E-M Relation could be compared to the slope of a stress strain curve. This slope should correlate to  $K_s$  (seismic stiffness modulus) and be representative of the system stiffness.

A simplistic physical explanation of the occurrence of the E-M Relation variation along geological structures can be provided in terms of a seismic event mechanism. The fundamental mechanism of a seismic event is that of simple shear. This results from the boundary conditions of the event preventing volume change – the event occurs within the solid rockmass. As a result of this mechanism, seismic events occurring along a geological structure in a stiffer environment will be clamped through an increased normal stress. The stiffer environment is created through the reduction of closure across the mine layout, e.g. introducing backfill. This will result in events occurring along the structure at comparatively increased stress levels but with reduced associated co-seismic deformation. In addition, as a result of the clamping, large seismic events will be restricted. Reducing the system stiffness, and hence unclamping the structure will cause seismic events to occur at lower stress levels and be associated with larger co-seismic deformation.

Extending the concept of system stiffness, when increasing the stiffness of the system the Gutenberg-Richter b-value will increase and  $M_{max}$  (maximum magnitude seismic event) will decrease (*van Aswegen and Mendecki, 1998, pg. 7*).

In seismology the Gutenberg-Richter law is defined as  $\log N(m) = a - b_m$ . The increase in the b-value as a result of stiffening the system can be attributed to the fact that a stiff system will prevent large seismic events, but will yield many small seismic events as a result of localised crushing of rock.

In summary, the theory, behind the observed change in slope of the E-M Relations is that through the combined effect of the source parameters (energy and moment) derived from the individual instabilities occurring and hence monitored within a system, an indication of the system stiffness can be extracted.

### 4.1.3. Hypotheses

From Sections 4.1.1 and 4.1.2 the following hypotheses are formulated to describe the physical mechanisms outlined. The hypotheses and hence the validity of the proposed mechanisms are tested through ‘well constrained’ numerical experiments in Section 4.3.

#### 4.1.3.1. Hypothesis 1 - Energy-Moment Ratio

Analysing the source parameters derived from instabilities occurring in systems with variable stiffness over a constant size range of interest, for equivalent energy instabilities:

Stiff System Instability Response : Higher Energy to Moment Ratio.

Soft System Instability Response : Lower Energy to Moment Ratio.

The terms ‘stiff’ and ‘soft’ refer to relative stiffnesses, i.e. relative abilities of the system to resist deformation with increasing load.

Thus the general hypothesis formulated from seismic observations of instabilities is:

$$(E_1/M_1)_{\text{stiff system}} > (E_1/M_1)_{\text{soft system}} \text{ for } E_1 = E_1 \text{ over a constant size range.}$$

Where:

E = radiated seismic energy derived from an instability (J)

M = seismic moment derived from an instability. (Nm)

E and M would be derived from the empirical E-M Relation (Log E – Log M plot).

The analogy formed through this hypothesis is that the stiffness of the surrounding system controls the ratio of energy to moment of resulting instabilities. Hence, for instabilities occurring in different systems with the same resulting energy released, a stiff system will act to restrict and clamp the resulting coseismic deformation generating an increased energy-moment ratio.

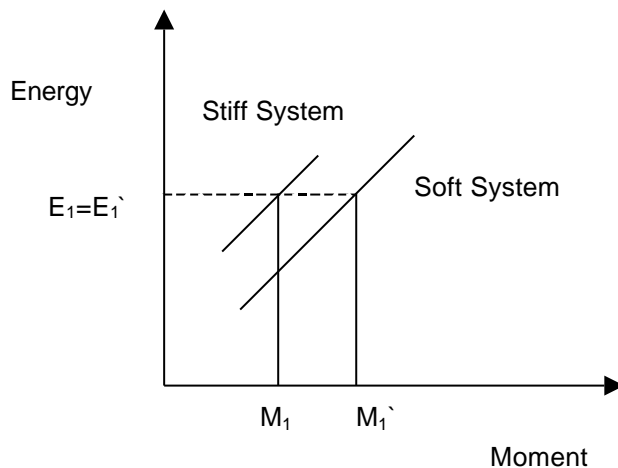


**Figure 4.2 Idealistic E-M relation – E-M Ratio Hypothesis.**

#### 4.1.3.2. Hypothesis 2 - Energy-Moment Relation Slope

Analysing the source parameters derived from instabilities occurring in systems with variable stiffness yields:

The Energy to Moment Relation of a stiff system increases at a greater rate with increasing energy than the Energy to Moment Relation of a soft system over the size range of interest (Figure 4.3).

$$[(E_2 - E_1)/(M_2 - M_1)]_{\text{stiff system}} > [(E_2' - E_1')/(M_2' - M_1')]_{\text{soft system}}$$

Where  $E_1 = E_1'$  and  $E_2 = E_2'$ .

E and M would be derived from the empirical E-M Relation

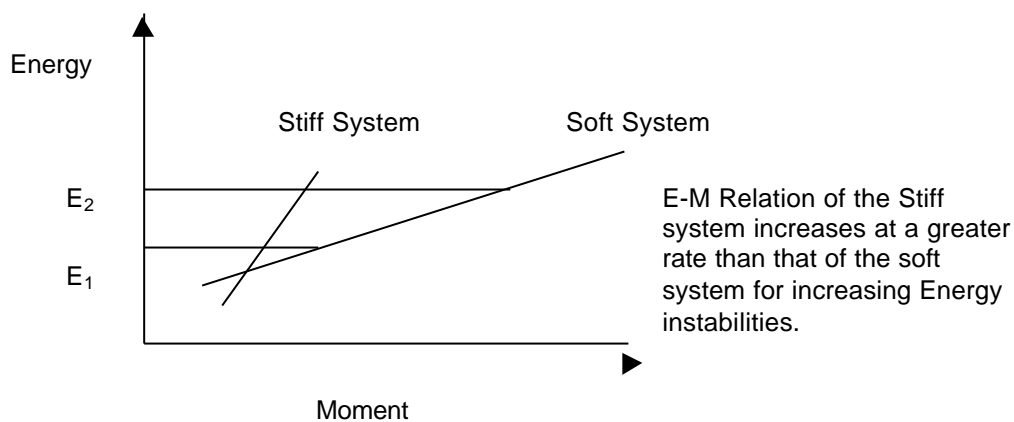


**Figure 4.3 Idealistic E-M relation – E-M Relation Slope Hypothesis.**

This is equivalent to the slope (d value) of the E-M Relation. A more informative method of analysing the above hypothesis is through utilising the concept of apparent stiffness (see glossary).

Apparent stiffness is dependent on both d and c. Thus the hypothesis formulated should be reduced to:

$$(K_{AS})_{stiff} > (K_{AS})_{soft}$$

The analogy formed is that the stiffness of the surrounding system controls the energy-moment relation derived from instabilities. For a stiff system, a large change in energy from the resulting instability will result in a relatively small increase in coseismic deformation due to the clamping affect of the surrounding system. However, in comparison, for instabilities occurring in a soft system, a small change in energy will result in a large increase in co-seismic deformation.

#### **4.1.4. Applied Analysis - Structure Stiffness**

In section 4.1.1-3 hypotheses were developed utilising the energy and moment source parameters derived from a combination of individual instabilities to indicate the system stiffness. This in combination with analysing the Gutenberg Richter cumulative frequency-magnitude relation b-value changes with system stiffness changes, present powerful design opportunities. The quantitative comparison of the overall system stiffness modulus (apparent stiffness) can be utilised for the optimal design of mine layouts.

However, limitations are still present as to the insight that can be gained into the system from the application of the above. When analysing a structure (a spatial window delineating a specific volume within the system) through an engineering design, the most important design parameter to address would be the relative degree of stability or instability of the structure. This type of analysis would need to be calibrated from and continually compared to the seismic measurements derived from the structure. Analysis of the E-M Relation and the Gutenberg-Richter frequency-magnitude relation will provide limited insight into the progressive degree of stability of a structure through time. Events occurring on an unstable structure within a system will present an E-M Relation with a relatively large Mmax and relatively low apparent stiffness (relatively low structure stiffness modulus).

#### **4.1.5. Hypothesis 3 – Applied Structure Stability Analysis**

A plot of energy index versus cumulative apparent volume progressing through time for a particular area (structure) is representative of a stress-strain curve derived from the analysis of the rockmass being loaded. Hence the modulus of the curve corresponds to the seismic stiffness modulus of the structure. Analysis of the modulus should yield:

- The point of peak strength of the structure being analysed (instability).
- The onset and degree of hardening prior to attaining the peak strength (local instabilities occurring within the structure).
- The degree of softening following the peak strength (instability) which should correlate to the occurrence of seismicity (the smaller the absolute value of the modulus in this regime, the more the structure flows and deforms).
- The peak strength of the structure, onset and degree of hardening and softening will be a function of the surrounding system stiffness.

In summary, an analysis of the stiffness modulus of a structure should yield an indication of the structures stability. If the structure being analysed engulfs the system, the analysis should be indicative of the system's degree of stability. When this is analysed in conjunction with the E-M Relation and the Gutenberg Richter frequency-magnitude relation, complete system and structure analyses can be formulated for calibration and comparison to engineering layout designs.

## 4.2. Modelled System Stiffness

### 4.2.1. Instability and System Stiffness – Theoretical Overview

*Bazant and Cedolin (1991, pg. 176)* state a general definition of stability such that a structure (or any system) is stable if a small change in the initial conditions (input) leads to a small change in the solution (output, response). Stiffness is defined (*Bazant and Cedolin, 1991, pg. 640*) as:

$$K_{ij} = \partial f_i / \partial q_j$$

Where:

$K_{ij}$  = components of the incremental tangential stiffness matrix.

$\partial f_i$  = the incremental small disturbing loads

$\partial q_j$  = the incremental small displacements

Hence stiffness includes both the reversible (elastic) and the irreversible (plasticity, damage) part of the deformation. Stiffness can therefore be defined as a measure of the system to resist deformation with increasing load.

*Bazant and Cedolin (1991, pg. 649)* go on to state that inelastic structures under a single controlled load are stable if the load deflection curve has a positive slope (hardening) and unstable if it has a negative slope (softening). This would equate to stiffness being greater or less than zero.

The critical states of stability can generally occur only if the stress is of the same order of magnitude as the tangential shear modulus of the material - materials undergoing a drastic reduction of tangential stiffness due to plasticity or damage (*Bazant and Cedolin, 1991, pg. 707*). Not all damage causes instability. If the tangential stiffness matrix is positive definite, in which case the stress-strain curve is rising and the material is said to exhibit strain hardening, damage causes no instability. When this matrix ceases to be positive definite, in which case the stress-strain curve is descending and the material is said to exhibit strain softening, instabilities and bifurcation's arise (*Bazant and Cedolin, 1991, pg. 829*).

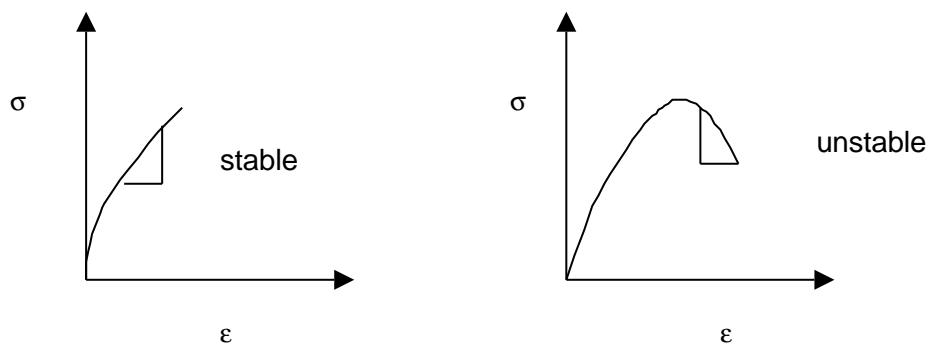


**Figure 4.4 Stable and Unstable System Response**

The slope of the stress-strain curve can be defined as the stiffness modulus:

$$K_{Mij} = d\sigma_{ij} / d\varepsilon_{ij}$$

Where:

$K_{Mij}$  = stiffness modulus matrix

$d\sigma_{ij}$  = rate of change of Cauchy stress tensor.

$d\varepsilon_{ij}$  = rate of change of total (elastic and plastic) strain tensor.

The stiffness modulus for a volume of rock  $V$  can then be defined as:

$$K_{Mij} = \int_V d\sigma_{ij} / d\varepsilon_{ij} dV$$

Hence,

$K_{Mij} > 0$  equates to strain hardening of the volume  $V$  (stable response).

$K_{Mij} < 0$  equates to strain softening of the volume  $V$  (unstable response).

Thus the stiffness modulus is defined as a measure of the system to resist deformation with increasing stress.

*Hobbs et al (1990, pg. 145)* outline a stability criterion proposed by *Hill (1958)* which states that the inner product of the next increment of stress with the next increment of strain should be positive for stable deformation. Hence the Hill criterion defines a body of rock under prescribed loads to be stable if over the volume,  $V$ , of the body:

$$\int_V d\sigma_{ij} \cdot d\varepsilon_{ij} dV > 0$$

Where:

$d\sigma_{ij}$  = rate of change of Cauchy stress tensor.

$d\varepsilon_{ij}$  = rate of change of total (elastic and plastic) strain tensor.

That is to say, a volume  $V$  of a body is stable if the sum of all the inner products of stress and strain increments through time over the volume  $V$  is positive. A quantitative assessment of the Hill Criterion and the Stiffness Modulus should also comparatively reflect the degree of hardening or softening prevalent within the system and hence the degree of relative stability or instability present (Figure 4.5).

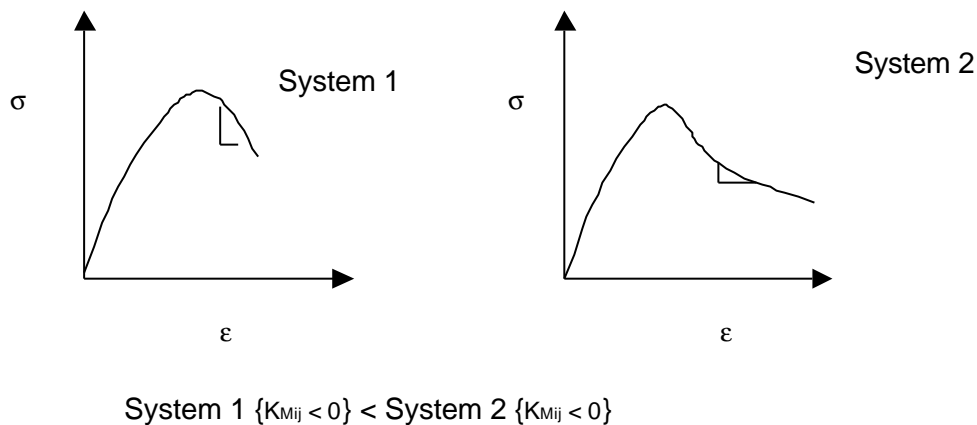


**Figure 4.5 Comparative degree of softening present within two systems**

In Figure 4.5, System 2 can be interpreted as exhibiting a higher degree of instability. This is characterised by reduced stiffness and hence increased deformation for a given negative stress increment.

Hence two design aspects could be practically applied. Firstly, applying the concepts outlined, to compare modelled stiffness to the results of seismic monitoring and establish a correlation between the two. Secondly, to use modelled system stiffness as a predictive tool, i.e. to establish how close a system is to instability through the application of either a dynamic impulse or a static load increment to the system, and then analyse the subsequent modelled system stiffness response.

#### 4.2.2. Applied System Stiffness – Large Geological Discontinuities

The concept of stability is essential for the understanding, interpretation and simulation of seismicity. This section outlines firstly the relationship between the mechanics of the simulation of seismicity utilising the asperity model on geological discontinuities and its relationship to system stiffness, and secondly the applied methods to extract estimates of system stiffness from the numerical analyses.

Unstable slip along a discontinuity surface is a function of interactions between the surrounding system, the loading mechanisms and the constitutive relations of the asperity. Use of the

asperity model for the simulation of seismicity along a discontinuity surface essentially approximates a two-dimensional problem, i.e. a thin structural weakness surrounded by a homogenous elastic rockmass.

The incorporation of the slip weakening constitutive relation accounts for the sudden loss in strength of the asperity surface, which is essential for the sudden release of energy and hence the simulation of seismicity. Mining induced stresses and viscoplastic loading of asperities derived from creeping gouge surrounding the asperity account for the loading mechanisms leading to the sudden failure of the asperity. The combined affect of all of the above throughout a volume  $V$  (or along a geological structure) relates to system stiffness – the continual gouge creep, mining and events of different sizes occurring at different times are controlled by, and subsequently alter the resultant stiffness of the system.

Simplistically, unstable slip can only occur if the slip weakening response of the asperity surface progresses at a greater rate than that of the surrounding loading system stiffness (*Dieterich, 1980*). If the loading system stiffness is high, it is possible to follow the slip weakening response of the asperity failure in a stable manner ( $\Delta K < 0$ , where  $\Delta K$  represents energy transferred to the surrounding rockmass), dissipating energy gradually through the fracturing process as per Figure 4.6 (*Rice, 1984*). For a low loading system stiffness, unstable slip results ( $\Delta K > 0$ ) as per Figure 4.7 (*Rice, 1984*). The combination of the low loading system stiffness and the slip weakening response results in excess energy being available to drive the resulting instability (the energy is not dissipated by the inelastic deformation of the asperity).

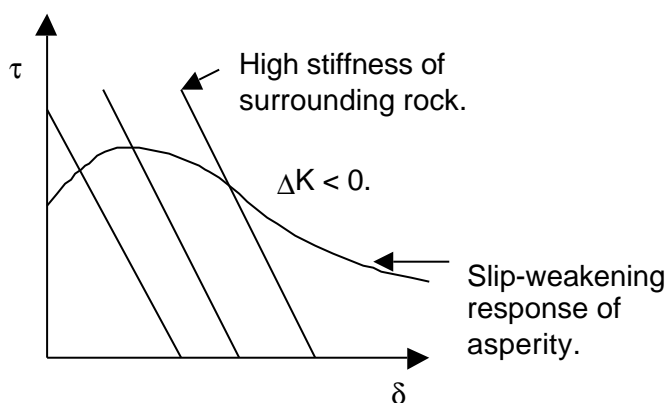


**Figure 4.6 Stable asperity failure with high loading stiffness of surrounding rock.**

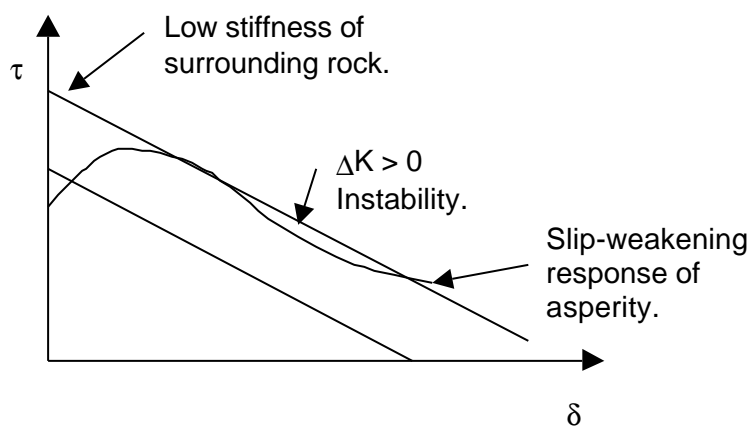


**Figure 4.7 Unstable asperity failure resulting from low loading stiffness of the surrounding rock.**

Figure 4.8 shows how differing system stiffness interacting with the asperity slip-weakening response results in different instability stiffness, and hence different resultant stress/strain change ratio's.

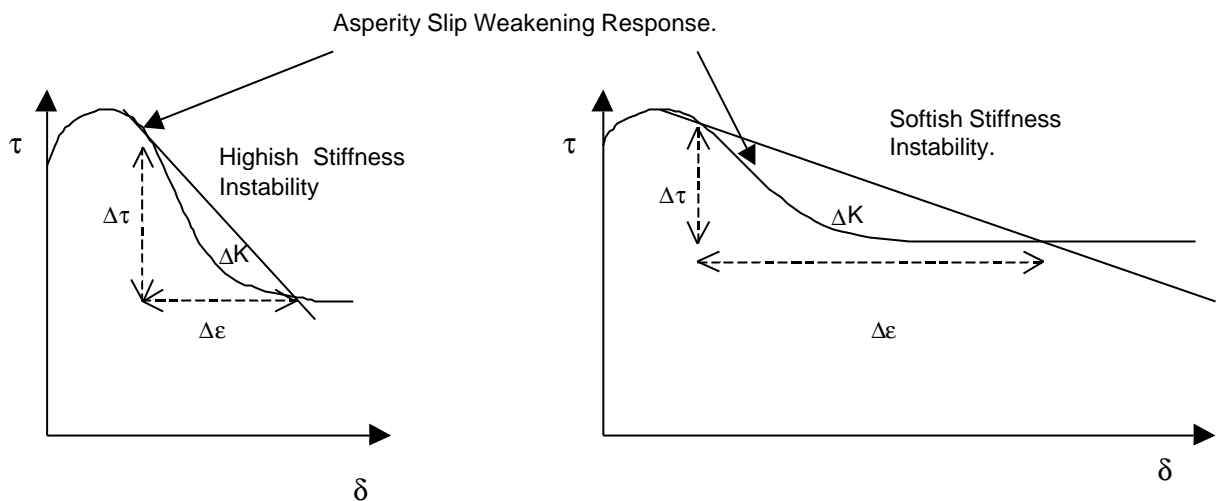


**Figure 4.8 Comparative Resultant Instability Stiffness.**

The detailed mechanics of the failure of the gouge, the gouges creep response, mining induced stresses and subsequent asperity failure (seismic event) are all interrelated and linked to the overall system stiffness. The analysis of the failure of a single asperity in terms of the concepts of the asperity model defined would include the following:

- Mining approaches the discontinuity.
- $K_M = \int_V d\sigma / d\epsilon dV$  where  $K_M$  = Structure Stiffness and  $V$  is a defined volume including a portion of the discontinuity surface surrounding an asperity (the extend of this volume will influence the interpretation of the results).
- At time  $t_0$  no failure has occurred in  $V$ ,  $K_M$  = elastic shear modulus of rock. Both the unfailed gouge and asperity gain shear stress.
- At time  $t_1$  the mining induced stresses exceed a portion of the gouge strength. The strength criterion is dependent on normal stress acting on the discontinuity surface and hence failure is controlled by the overall system stiffness.
- Damage occurs – gouge fails and starts to creep (the rate of creep is controlled by the amount of over stressing acting on the gouge). The creep front is extended.  $K_M$  reduces to a lower positive value (strain hardening). However, the unfailed portion of the gouge and asperity are still gaining stress at a faster rate than the creeping gouge relaxes and dissipates stress.
- Increased gouge failure occurs, mining increases, creep rate increases, viscoplastic loading and the mining induced stress loading on the asperity increases.  $K_M$  reduces further to a lower positive value (precursory deformation predicts instability).
- At time  $t_3$   $K_M = 0$  and Hill Stability Criterion = 0 signifying instability. The system is now at such a point that the stress gained by the system is equivalent to the stress dissipated by the system. Any stress/load increment subsequent to attaining this point will lead the structure being analysed into instability.
- Asperity fails (slip weakening response). The stress drop and strain increment over the asperity region are controlled by the system stiffness. In addition, as a result of the sudden asperity failure coseismic deformation spreads over the surrounding gouge, the extent and amount of which is controlled and driven by the surrounding system.  $K_M$  changes to a high negative value signifying the structure to be unstable.
- Thereafter further deformation occurs, the creep front extends, further mining occurs and  $K_M$  reduces to a low negative value signifying the structure to have attained a higher degree of instability and hence be easily deformable.



This argument could be extended to a large volume over the discontinuity surface, and be inclusive of a number of asperities with a heterogeneous strength distribution. The principles will essentially remain the same, with only the interactions becoming increasingly complex. It is important to remember that, for a large number of asperities with a heterogeneous strength distribution, failure (seismic events) will occur in the period of strain hardening prior to the structure becoming unstable. Structure instability merely indicates a fundamental change in the behaviour of the structure; i.e. the structure as a whole can no longer sustain higher stress levels, and loses stress with increasing deformation.

### 4.2.3. Numerical Methods

In order to incorporate the theoretical concepts outlined in section 4.2.1, and test the observed concepts from seismic monitoring outlined in section 4.1, methods of analysis were developed for the asperity model under viscoplastic displacement loading utilising boundary element code. At present all the analysis methods were adapted for the analysis of geological structures. The detailed theoretical aspects, validation of and implementation methodology of the asperity model into boundary element code are described in *Lachenicht (in prep.)*. However, a summary of the fundamental concepts incorporated around the asperity model are listed below.

Boundary Element Code:

- Complex three-dimensional layouts of case studies can be incorporated.
- Complex three-dimensional geological structures can be incorporated.
- Reduced run times facilitates the analysis of complex layout permutations.

The mechanics of the simulation of discrete seismic events:

- The asperity model.
- Viscoplastic displacement loading of asperities.
- A slip-function representing unstable asperity failure.
- Quasi-static analyses (inertial effects are ignored).

The mechanics of the simulation of seismicity:

- The incorporation of multiple asperities.
- Spatial heterogeneity of asperities.
- Strength heterogeneity of asperities.
- The occurrence of discrete seismic events through time.

The analysis of seismicity:

- Methods for the calculation of the energy and moment source parameters for simulated seismic events derived from the failure of single asperities.
- Methods and numerical code for the calculation of the energy and moment source parameters for simulated seismic events derived from the failure of single and multiple asperities.
- Methods for the calculation of the frequency-magnitude relation.
- Methods for the calculation of the average stress change versus cumulative deformation plots, associated stiffness moduli and stability criteria.

Incorporation of all of the above into a single tool allows for the analysis of the modelled system stiffness in order to corroborate the observed hypotheses. The general procedure for the back analysis of geological structures through numerical models and its integration with quantitative seismology is:

1. Build model layout, mining steps and geological structures.
2. Incorporate asperities, spatial and strength heterogeneity over the structures surface.
3. Incorporate initial parameter estimates from seismic and non-seismic observations.
4. Run the model for a period of time.
5. Analyse stress/strain/stiffness/stability derived from the numerical model.
6. Compare to the interpretations of seismic data and re-calibrate the model.
7. Run the model through time.
8. Analyse the resulting E-M relation, frequency-magnitude relation, and stiffness moduli.

9. Compare to the results of seismic monitoring.
10. Re-run with a new layout, asperity distribution and parameter values.

The basis of these concepts are initially applied in the numerical experiments undertaken in section 4.3. Section 5 outlines an engineering methodology built from the analysis tool to optimally design mine layouts.

### 4.3. Applied Modelled System Stiffness - Numerical Experiments

In sections 4.1.3 and 4.1.5, three hypotheses were proposed. The first two hypotheses relate the characteristics of resulting instabilities occurring within soft and stiff systems. The third hypothesis proposes a method to assess and compare the onset and degree of instability of both the system and structures existing within the system for varying system stiffnesses. Extending these ideas, simple comparative numerical models are utilised to determine whether the characteristics of the resulting modelled instabilities conform to the theoretical hypotheses derived from observations.

#### 4.3.1. Energy-Moment Ratio and Energy-Moment Relation Slope

The E-M Ratio and Relation Slope hypotheses are numerically tested through three idealistic experiments.

##### 4.3.1.1. Experiment 1

This experiment compares the modelled response of a creeping discontinuity within a system of variable stiffness. The experiment does not include asperities along the discontinuity surface. However, although no seismic events per se are simulated, the macro discontinuity creep/fracture response is emulated, forming the basis of more advanced experiments.

In order to ensure that the direct change in stiffness of the system is being compared, varying load increments are simulated within each system for identical time windows and extraction ratios. The application of varying load increments enables the response of each system to be calculated and compared. In order to ensure consistent results, identical load increment are applied between systems. Identical time windows ensure that the system stiffness of the two systems are different at the time of analysis, as stiffness changes through time.

The objective of the experiment is to test how two systems of different stiffness will comparatively react to varying load increments imposed along the discontinuity surface. The system response is gauged from the resultant failure recorded along the discontinuity surface. The experiment design is such that:

For a time period  $t_1$  to  $t_2$  within a stiff and soft system,

- No asperities are present on the discontinuity surface.
- Extraction ratios for each system are identical.
- Time  $t_{1(\text{soft system})} = t_{1(\text{stiff system})}$ .
- Discontinuity surface discretisation between the systems is constant.
- Constant high gouge viscosities are applied between systems limiting large-scale deformations.
- High/low in-situ stress normal to the discontinuity surface emulates the relative change in system stiffness.
- A constant variation of viscosity simulates the variable load increment applied to the system during a particular time window.
- Constant mining geometry and mining step increments are incorporated for both systems.

Table 4.1 lists the parameter assumptions utilised in experiment 1.

**Table 4.1 Experiment 1 Model Parameter Assumptions**

Experiment 1 Model Parameter Assumptions

Parameter	Value
Analysis Method	Creep Only
Time of Analysis	t+390 days
Gouge Peak Friction	30 degrees
Gouge Residual Friction	20 degrees
Gouge Peak Cohesion	0 MPa
Soft1 Gouge Viscosity Coefficient	1e3 MPa
Soft2 Gouge Viscosity Coefficient	386 MPa
Stiff1 Gouge Viscosity Coefficient	1e3 MPa
Stiff2 Gouge Viscosity Coefficient	386 MPa
Failure Criterion	Mohr Coulomb
Viscoplastic Flow Rule	Binghams
Model Time Step Increment	30 days
Mining Rate	12m/month
Mining Geometry	Idealistic
Soft System k-ratio normal to fault	0.4
Stiff System k-ratio normal to fault	0.6
Grid Block Area	225m <sup>2</sup>

The methodology utilised in the experiment is to firstly delineate the instability extent (fracture surface) resulting from each load increment applied during the analysis time window. Secondly, average stress/strain changes are calculated over the fracture extent and compared.

The detailed calculation procedure is:

1. Filter Safety Factor < 1 (fracture extent delineation).
2.  $\Delta \bar{\sigma} = \bar{\sigma}_{t+1} - \bar{\sigma}_t$   
Where:  
 $\Delta \bar{\sigma}$  = Average shear stress change over the fracture surface (Pa)  
 $\bar{\sigma}_{t+1}$  = Average shear stress at time t+1 over the fracture surface (Pa)  
 $\bar{\sigma}_t$  = Average shear stress at time t over the fracture surface (Pa)
3.  $\Delta \bar{u} = \bar{u}_{t+1} - \bar{u}_t$   
Where:  
 $\Delta \bar{u}$  = Average slip over the fracture surface (m)  
 $\bar{u}_{t+1}$  = Average deformation at time t+1 over the fracture surface (m)  
 $\bar{u}_t$  = Average deformation at time t over the fracture surface (m)
4. Modelled Stiffness Modulus =  $\Delta \bar{\sigma} / \Delta \bar{u}$  for the analysis time window t to t+1 (Pa/m)
5. Change of modelled stiffness = inferred from E-M Relation.
6. Instability Energy =  $\sum \frac{1}{2} \Delta \sigma_i \cdot \Delta u_i \cdot A_i$  (J).  
 $\Delta \sigma_i$  = shear stress change from time t to t+1 for each grid block (Pa).  
 $\Delta u_i$  = slip from time t to t+1 for each grid block (m).  
 $A_i$  = area of each grid block (m<sup>2</sup>).
7. Instability Moment =  $\mu \cdot \sum \Delta u_i \cdot A_i$  (Nm)  
 $\mu$  = Rigidity (3e10 Pa)  
 $\Delta u_i$  = slip from time t to t+1 for each grid block (m)  
 $A_i$  = area of each grid block (m<sup>2</sup>).

This enables the E-M Ratio and E-M Relation changes between systems to be compared.

Table 4.2 lists the comparative average stress/strain changes between systems for the analysis window t+390 days to t+420 days. Figure 4.9 shows the comparative average stress/strain change plot.

**Table 4.2 Comparative Modelled Instability Stiffness Results**

Comparative modelled instability average deformation and stiffness changes for varying average stress change.

Experiment	Average Stress Change MPa	Average Deformation Change m	Modelled Instability Stiffness Mpa/m
Soft1	-4.65E-01	6.01E-03	-77.28
Soft2	-5.63E-01	8.88E-03	-63.45
Stiff1	-2.27E+00	7.85E-03	-289.66
Stiff2	-4.22E+00	1.50E-02	-281.69

Time =+ 390 days.

Extraction Ratio = constant.

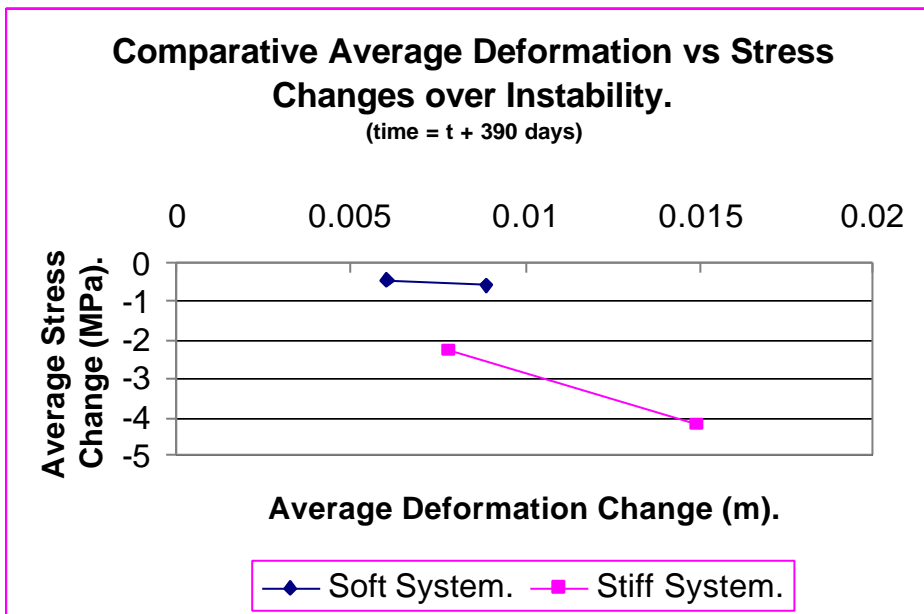


**Figure 4.9 Comparative Modelled Instability Stiffness Results**

Table 4.2 and Figure 4.9 show the stiff system to yield instabilities of higher stiffness moduli, with greater average stress/strain change increases between the load increments. This is indicative of the stiffer systems increased ability to resist deformation with increasing stress.

Table 4.3 and Figure 4.10 show the inferred E-M parameters and E-M Relation of the modelled instabilities (fractures) within each system.

**Table 4.3 Inferred E-M Relation Parameters**

Comparative modelled E-M Relation.

SYSTEM.	TOTAL ENERGY (J)	MOMENT (Nm).	SEISMIC ENERGY (J)	Emag	Mmag
soft1	1.47E+08	1.36E+13	1.47E+06	1.03	2.68
soft2	3.85E+08	3.16E+13	3.85E+06	1.25	2.92
stiff1	2.80E+07	7.42E+11	2.80E+05	0.65	1.84
stiff2	9.91E+07	1.42E+12	9.91E+05	0.94	2.03

Time =t+ 390 days.

Extraction Ratio = constant.

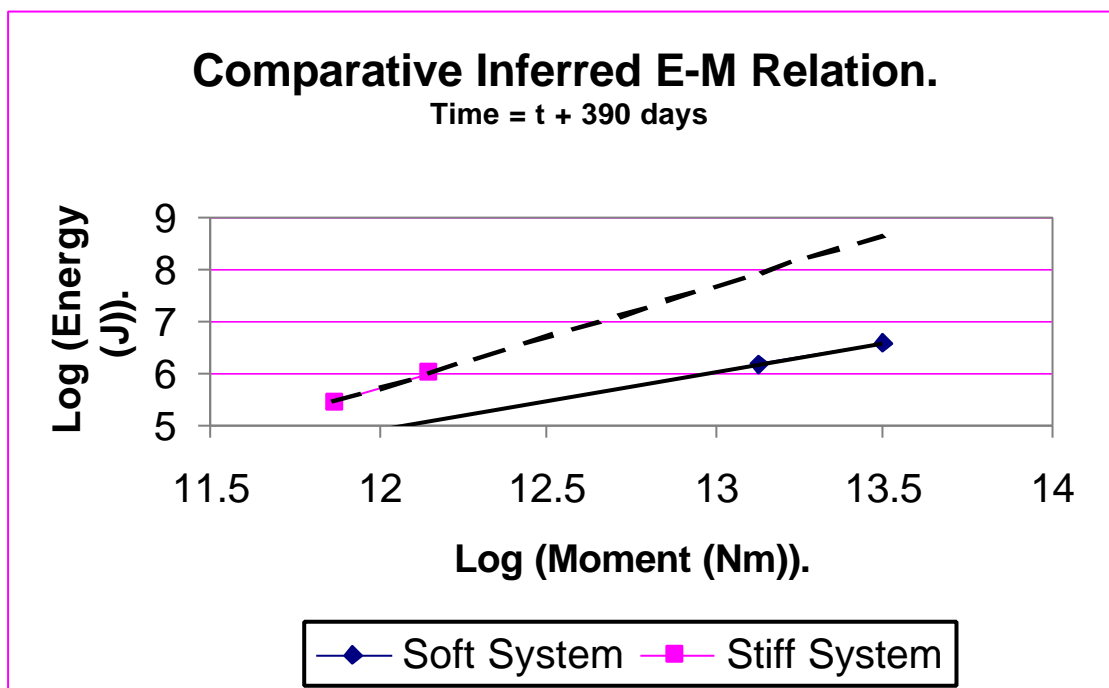


**Figure 4.10 Comparative Inferred E-M Relations**

The results are consistent with hypotheses 1 and 2. Both the E-M Ratios and E-M Relation change with increasing system stiffness. However, aspects of the experiment to be considered are:

- The effect in the experiment of the change in viscosity utilised to simulate the varying load increments.
- The effect of the simulation of discrete seismic events on the experiment results.

#### 4.3.1.2. Experiment 2

This experiment compares the modelled response of a creeping discontinuity within a system of variable stiffness with the inclusion of a single asperity.

In order to ensure that the direct change in stiffness of the system is being compared, varying stress drop asperities failing in identical time windows and extraction ratios are compared. However, the absence of the fractal distribution of asperity sizes and strengths negates the possibility of simulating similar event sizes between experiments.

For a stiff and a soft system, asperities with varying stress drops (varying energy instabilities) are allowed to fail in identical time windows and for identical extraction ratios. The only difference between the two systems being the normal stress acting on the geological structure emulating the system stiffness.

The objective of the experiment is to test how two different systems will comparatively react for different imposed load increments (stress drops) along the discontinuity surface. The load increments result from the failure of a single asperity within a constant time window. The system response is gauged through the resultant failure recorded along the discontinuity surface. The experiment design is such that:

For a time period  $t_1$  to  $t_2$  within a stiff and soft system,

- Peak strengths of the asperities are constant within each system. This forces the asperity failure to occur within a constant time window (stiffness changes with time).
- Stress drops of the asperities within each system varies – simulates varying load increments within the analysis time window.
- Asperities are arbitrarily located in the middle of the resultant ‘Excess Shear Stress’ zone on the discontinuity surface.
- Filters are run to enable the coseismic stress/deformation changes to be extracted from the analyses.
- Extraction ratios for each system are identical.
- Time  $t_{1(\text{soft system})} = t_{1(\text{stiff system})}$ .
- Discontinuity surface discretisation between systems is constant.
- A constant high gouge viscosity is applied between systems limiting large-scale deformations.
- High/low in-situ stress normal to the discontinuity surface corresponds to the relative change in system stiffness.
- Constant mining geometry and mining step increments are incorporated for both systems.

Table 4.4 lists the parameter assumptions utilised in experiment 2.

### **Table 4.4 Experiment 2 Model Parameter Assumptions**

Experiment 2 Model Parameter Assumptions

<b>Parameter</b>	<b>Value</b>
Analysis Method	Single Asperity
Time of Analysis	t+420 days
Gouge Peak Friction	30 degrees
Gouge Residual Friction	20 degrees
Gouge Peak Cohesion	0 MPa
Gouge Viscosity	2.59e15 Pa.sec
Soft System Asperity Peak Friction	60 degrees
Soft System Asperity Residual Friction	30,20,10 degrees
Stiff System Asperity Peak Friction	32.5 degrees
Stiff System Asperity Residual Friction	25,20,10 degrees
Asperity Cohesion	0 Mpa
Failure Criterion	Mohr Coulomb
Viscoplastic Flow Rule	Binghams
Model Time Step Increment	30 days
Mining Rate	12m/month
Mining Geometry	Idealistic
Soft System k-ratio normal to fault	0.4
Stiff System k-ratio normal to fault	0.6
Grid Block Area	225m <sup>2</sup>

The analysis methodology utilised is:

- The single asperity is located in the middle of the resultant 'Excess Shear Stress' zone.
- The residual strength of the asperity within each system is altered to allow the system response to varying load increments to be captured. From this different event sizes are simulated within each system allowing for an E-M Relation for that system and time window to be attained.
- The peak strength of the asperities for both systems is set to fail at time t+390-420 days enabling the comparative results to be consistent with variable system stiffnesses (system stiffness changes with time).
- Filters are run to extract the resultant co-seismic source parameters of each event.

The detailed calculation procedure applied is:

1. Filter coseismic slip >1mm (constrain experiment output).
2.  $\Delta\sigma_i = \sigma_i - \sigma_{(filter)_i}$  (Pa)  
 $\Delta\sigma_i$  = shear stress change from time t to t+1 for each grid block (Pa).  
 $\sigma_i$  = shear stress at time t+1 for each grid block (Pa).  
 $\sigma_{(filter)_i}$  = shear stress at time t+1 for each grid block from the filter analysis (Pa).
3.  $\Delta u_i = u_i - u_{(filter)_i}$  (m)  
 $\Delta u_i$  = slip from time t to t+1 for each grid block (m).  
 $u_i$  = deformation at time t+1 for each grid block (m).  
 $u_{(filter)_i}$  = deformation at time t+1 for each grid block from filter analysis (m).
4. Instability Energy =  $\sum \frac{1}{2} \Delta\sigma_i \cdot \Delta u_i \cdot A_i$  (i = asperity block only) (J)  
 $\Delta\sigma_i$  = shear stress change from time t to t+1 for each grid block (Pa).  
 $\Delta u_i$  = slip from time t to t+1 for each grid block (m).  
 $A_i$  = area of each grid block (m<sup>2</sup>).
5. Instability Moment =  $\mu \cdot \sum \Delta u_i \cdot A_i$  (Nm)  
 $\mu$  = Rigidity (3e10 Pa)  
 $\Delta u_i$  = slip from time t to t+1 for each grid block (m).  
 $A_i$  = area of each grid block (m<sup>2</sup>).
6. Change of modelled stiffness = inferred from E-M Relation.  
This enables a comparison to be made between the E-M Ratio and E-M Relation changes between systems.

Table 4.5 and Figure 4.11 show the calculated E-M parameters and E-M Relation of the modelled instabilities (seismic events) within each system. Table 4.6 lists the quantitative E-M ratios and E-M gradients between events and systems.

**Table 4.5 Calculated E-M Parameters derived from the Asperity Model.**

Comparative E-M Relation derived from the Asperity Model.

SYSTEM.	BLOCK AREA	STRESS DROP	TOTAL ENERGY	MOMENT	SEISMIC ENERGY	Emag	Mmag
	(m2)	(MPa)	(J)	(Nm)	(J)		
soft1	225	-45.30	4.83E+08	2.03E+13	4.83E+06	1.30	2.80
soft2	225	-39.84	3.73E+08	7.93E+12	3.73E+06	1.24	2.52
soft3	225	-33.63	2.66E+08	6.01E+11	2.66E+06	1.17	1.78
stiff1	225	-7.50	1.32E+07	1.06E+11	1.32E+05	0.48	1.28
stiff2	225	-12.00	3.38E+07	1.79E+11	3.38E+05	0.70	1.43
stiff3	225	-20.24	9.63E+07	3.23E+11	9.63E+05	0.94	1.60

Filter Applied : Deformation Change > 0.001m.

Time = t + 420 days.

Extraction Ratio = Constant.

**Table 4.6 Comparative quantitative E-M Ratio and Gradient between systems.**

SYSTEM	COMPARATIVE E-M RATIO.	COMPARATIVE E-M GRADIENT
soft1	2.38E-07	
soft2	4.71E-07	
soft3	4.43E-06	1.10E-07
stiff1	1.25E-06	
stiff2	1.89E-06	
stiff3	2.98E-06	1.00E-02

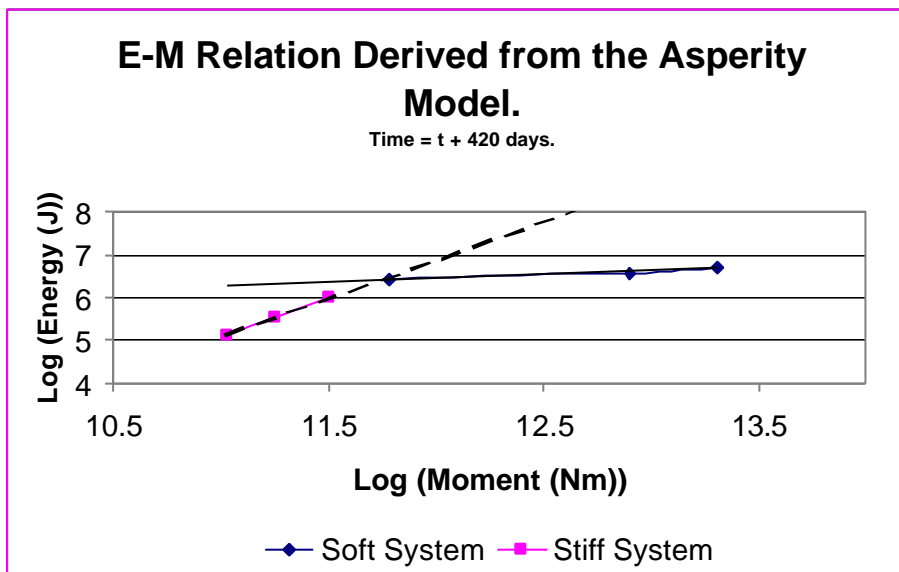


**Figure 4.11 E-M Relation derived from the asperity model**

Table 4.6 and Figure 4.11 show the resultant E-M Relation/slope to change significantly as a result of the increasing system stiffness in accordance with hypothesis 2. However, due to the experiment design, E-M Ratios between the systems are not comparable (significantly different event sizes). Aspects to be considered are:

- Hypothesis 1 is unable to be tested due to the fact that similar size events cannot be simulated between systems (time window constraint). Hence, to simulate the E-M Ratio changes, multiple asperities must be included in the analysis.
- The effect of the inclusion on the discontinuity surface of randomly placed multiple asperities with a heterogeneous strength distribution.

#### 4.3.1.3. Experiment 3

This experiment compares the modelled response of a creeping discontinuity through time, and increasing volumetric extraction (degrading system stiffness) with the inclusion of multiple asperities. The asperities are randomly located over the discontinuity surface and are assigned a heterogeneous strength distribution.

The objective of the experiment is to test how the modelled E-M Relation will change over a creeping discontinuity through time for a constantly increasing volumetric extraction, and hence degrading system stiffness. The experiment design is such that:

For time periods starting at  $t=t+210$ days and  $t=t+390$ days,



- Multiple asperities with a heterogeneous strength distribution are randomly placed over the discontinuity surface.
- Filters for the analysis time periods are run to enable the coseismic stress/deformation changes to be extracted from the analyses.
- A constant high gouge viscosity is applied limiting large-scale deformations.
- Constant mining step increments are utilised.

Table 4.7 lists the parameter assumptions utilised in experiment 3.

**Table 4.7 Experiment 3 Model Parameter Assumptions.**

Experiment 3 Model Parameter Assumptions

<b>Parameter</b>	<b>Value</b>
Analysis Method	Multiple Asperity
Time of Analysis	Varies - t+210 / t+390 days
Gouge Peak Friction	25 degrees
Gouge Residual Friction	20 degrees
Gouge Peak Cohesion	0 MPa
Gouge Viscosity	2.59e15 Pa.sec
Asperity Peak Friction	Heterogeneous Distribution
Asperity Residual Friction	20 degrees
Asperity Placement	Random Distribution
Strength Distribution	Power Law / alpha = 1.5
Asperity Cohesion	0 Mpa
Failure Criterion	Mohr Coulomb
Viscoplastic Flow Rule	Binghams
Model Time Step Increment	30 days
Mining Rate	12m/month
Mining Geometry	Idealistic
Mining Step	1 per time step
System k-ratio normal to fault	0.5
Grid Block Area	225m <sup>2</sup>

Table 4.8 lists the strength distribution parameter assumptions assigned to the asperities randomly placed over the discontinuity surface. The strength distribution utilises the cumulative power law distribution  $P(\Delta\tau > \Delta\tau') = (\Delta\tau/\Delta\tau_{\min})^{-\alpha}$  where  $\alpha = 1.5$ . Figure 4.12 shows the resultant distribution.

**Table 4.8 Asperity strength distribution parameter assumptions**

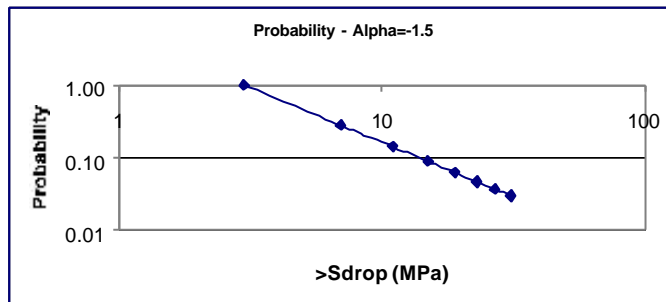
**Fault dimensions:**

1167.04,1200,-1805.12                      1167.04,-200,-1805.12  
 804.75,1200,-2800.51                      804.75,-200,-2800.51  
 Centre = 985.895,500,-2302.815  
 strike span = 1400m  
 Dip span = 1059m  
 15m grids = 93x71 grids = 6603 elements

P(>sdrop)	Number	Alpha=1.5 Probability	Total Fault Units	Cum Asp Numbers	Ind Asp Numbers
3.00	1.00	1.00	6603.00	6603.00	4750.42
7.00	2.33	0.28	6603.00	1852.58	912.13
11.00	3.67	0.14	6603.00	940.45	349.86
15.00	5.00	0.09	6603.00	590.59	176.31
19.00	6.33	0.06	6603.00	414.28	103.23
23.00	7.67	0.05	6603.00	311.05	66.50
27.00	9.00	0.04	6603.00	244.56	45.77
31.00	10.33	0.03	6603.00	198.78	198.78
					6603.00

P(>sdrop)	Number	Ind Percent	Tot Asp	%of Fault Asperities	Residual Friction	Fpeak Equivalent Sn=30MPa	Sdrop at
3.00	1.00	71.94			20	25	3.070123 creep blocks only
7.00	2.33	13.81	1653.79	25.05	20	30	6.401401 asperities
11.00	3.67	5.30			20	35	10.08712 asperities
15.00	5.00	2.67			20	40	14.25388 asperities
19.00	6.33	1.56			20	45	19.08089 asperities
23.00	7.67	1.01			20	50	24.8335 asperities
27.00	9.00	0.69			20	55	31.92533 asperities
31.00	10.33	3.01					Not Assigned

P(>sdrop)	alpha=-1.5
3	1.00
7	0.28
11	0.14
15	0.09
19	0.06
23	0.05
27	0.04
31	0.03



P(>sdrop)	alpha=-1.5
3	4750.423634
7	912.1297425
11	349.8563495
15	176.311409
19	103.2279916
23	66.49531798
27	45.77191568
31	198.7836399

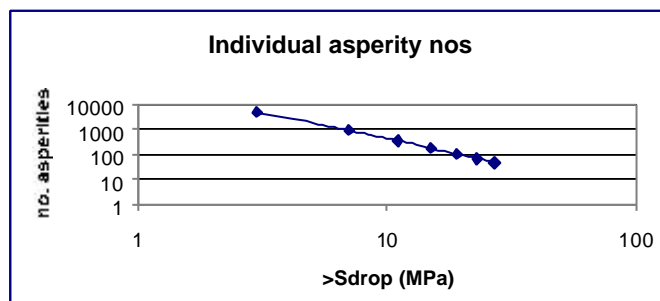


**Figure 4.12 Asperity strength distribution**

The experiment results are calculated in accordance with the methods outlined in Section 5. The methods are adopted to facilitate the source parameter derivation from large numbers of failing asperities (seismic events) with resulting overlapping coseismic deformations. A summary of the calculation procedure is:

1. Filter coseismic slip  $>0.1\text{mm}$  (constrain experiment output).
2.  $\Delta\sigma_i = \sigma_i - \sigma_{(\text{filter})i}$  (Pa)  
 $\Delta\sigma_i$  = shear stress change from time  $t$  to  $t+1$  for each grid block (Pa).  
 $\sigma_i$  = shear stress at time  $t+1$  for each grid block (Pa).  
 $\sigma_{(\text{filter})i}$  = shear stress at time  $t+1$  for each grid block from filter analysis (Pa).
3.  $\Delta u_i = u_i - u_{(\text{filter})i}$  (m)  
 $\Delta u_i$  = slip from time  $t$  to  $t+1$  for each grid block (m).  
 $u_i$  = deformation at time  $t+1$  for each grid block (m).  
 $u_{(\text{filter})i}$  = deformation at time  $t+1$  for each grid block from filter analysis (m).
4. Instability Energy =  $\sum \frac{1}{2} \Delta\sigma_i \cdot \Delta u_i \cdot A_i$  (asperity blocks failing in each seismic event) (J)  
 $\Delta\sigma_i$  = shear stress change from time  $t$  to  $t+1$  for each asperity grid block (Pa).  
 $\Delta u_i$  = slip from time  $t$  to  $t+1$  for each asperity grid block (m).  
 $A_i$  = area of each asperity grid block ( $\text{m}^2$ ).
5. Instability Moment =  $\Delta \sigma \cdot \Delta V$   
 $\Delta \sigma$  = average stress change over the instability (Pa)  
 $\Delta V$  = volume of co-seismic slip ( $\text{m}^3$ )
6. Change of modelled stiffness = inferred from E-M Relation.

Table 4.9 and Figure 4.13 show the E-M Relation calculated from the individual seismic events occurring in the two time periods analysed. Five events are analysed for each period, enabling the comparative E-M Relations to be formulated.

**Table 4.9 Calculated E-M Parameters derived from the asperity model.**

SYSTEM.	TOTAL	MOMENT	SEISMIC	Emag	Mmag	E/M Ratio
	ENERGY (J)	(Nm).	ENERGY (J)			
event 1 / time 280 days	1.79E+07	8.66E+10	1.79E+05	0.55	1.22	2.07E-06
event 2 / time 280 days	3.88E+06	3.71E+10	3.88E+04	0.20	0.97	1.05E-06
event 3 / time 280 days	1.38E+07	7.70E+10	1.38E+05	0.49	1.18	1.79E-06
event 4 / time 280 days	3.47E+06	2.65E+10	3.47E+04	0.18	0.87	1.31E-06
event 5 / time 280 days	1.29E+07	5.51E+10	1.29E+05	0.48	1.09	2.35E-06
event 1 / time 390 days	8.44E+07	1.29E+12	8.44E+05	0.91	2.00	6.54E-07
event 2 / time 390 days	1.67E+07	1.71E+11	1.67E+05	0.54	1.41	9.78E-07
event 3 / time 390 days	5.64E+07	7.83E+11	5.64E+05	0.81	1.85	7.20E-07
event 4 / time 390 days	1.36E+07	2.28E+11	1.36E+05	0.49	1.50	5.96E-07
event 5/ time 390 days	1.19E+08	9.89E+11	1.19E+06	0.98	1.92	1.20E-06

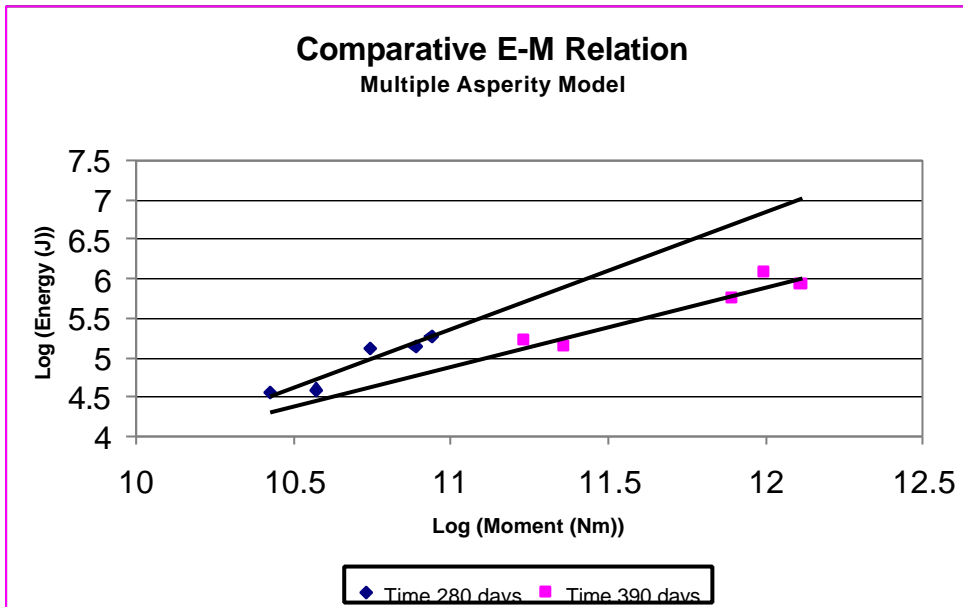


**Figure 4.13 E-M Relation derived from the asperity model with multiple asperities**

From figure 4.13 the analysis of five events for each time period is sufficient to show the experiment results to be consistent with hypotheses 1 and 2. Both the E-M Ratio and E-M Relation vary as a result of a change in system stiffness (increasing volumetric extraction).

### 4.3.2. Structure Stability Analysis

Idealistic experiments are designed to analyse initial numerical procedures to assess and compare the onset and degree of instability of structures within a system (hypothesis 3). In the simulations, unfiltered data derived from the full multiple asperity model of section 4.3.1.3 is utilised.

#### 4.3.2.1. Experiment 1

This experiment analyses a small spatial window (structure) delineated over a portion of the discontinuity surface through time. The window completely fails over the analysis time period.

Figure 4.14 shows the average shear stress of the asperities versus the cumulative average deformation occurring through time in the delineated analysis window.

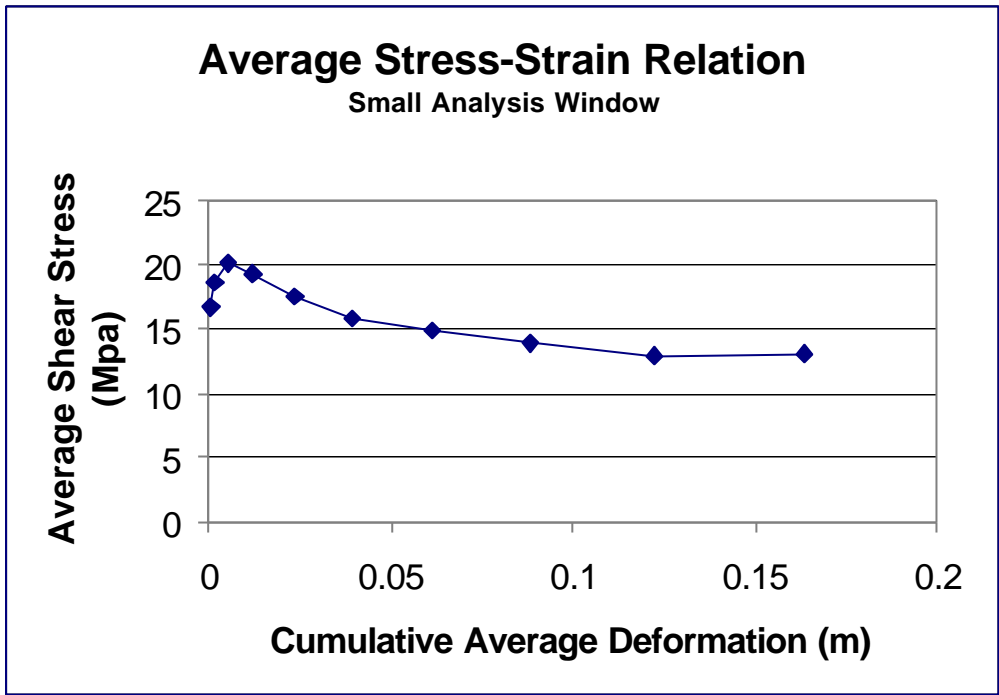


**Figure 4.14 Average Stress-Strain Relation derived from a small analysis window**

From Figure 4.14 an initial period of strain hardening can be noted (degrading positive stiffness modulus). This would be indicative of the structure moving towards instability. Subsequently the structure completely changes behaviour and becomes unstable, with the stiffness modulus moving from a high to a low negative value through time. The lower the negative stiffness modulus the more the unstable structure is deforming/flowing for a given negative average stress increment.

Figure 4.15 correlates the average stress-strain relation to the average cumulative energy released through time.

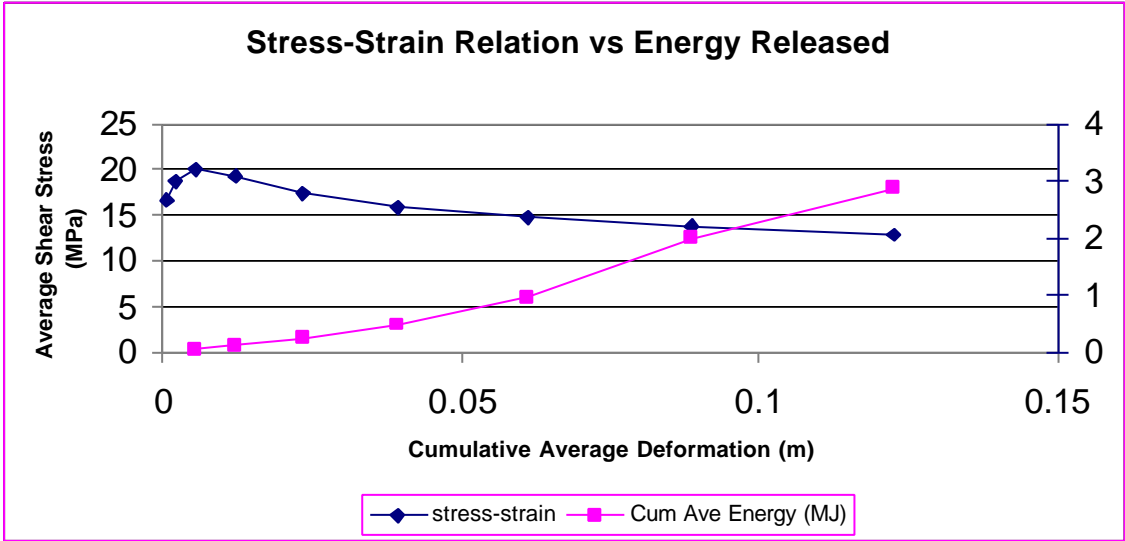


**Figure 4.15 Average Stress-Strain Relation versus average cumulative energy released through time**

In Figure 4.15 the increases in the average cumulative energy released correlate to the changes of the system stiffness modulus. This is consistent with hypothesis 3.

### 4.3.2.2. Experiment 2

This experiment analyses average Stress-Strain Relations derived from various spatial window sizes (structures) over the discontinuity surface through time. Figure 4.16 shows the average Stress-Strain Relation of a fine/small spatial window, and Figure 4.17 that of a large spatial window (encompasses the full discontinuity surface modelled).

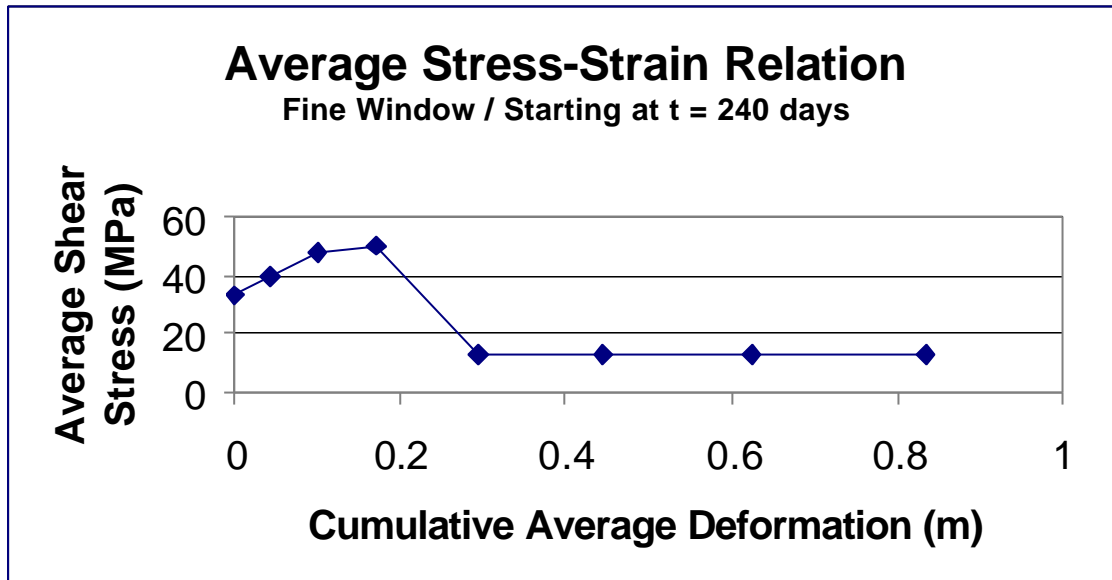


**Figure 4.16 Average Stress-Strain Relation derived from a small spatial window**

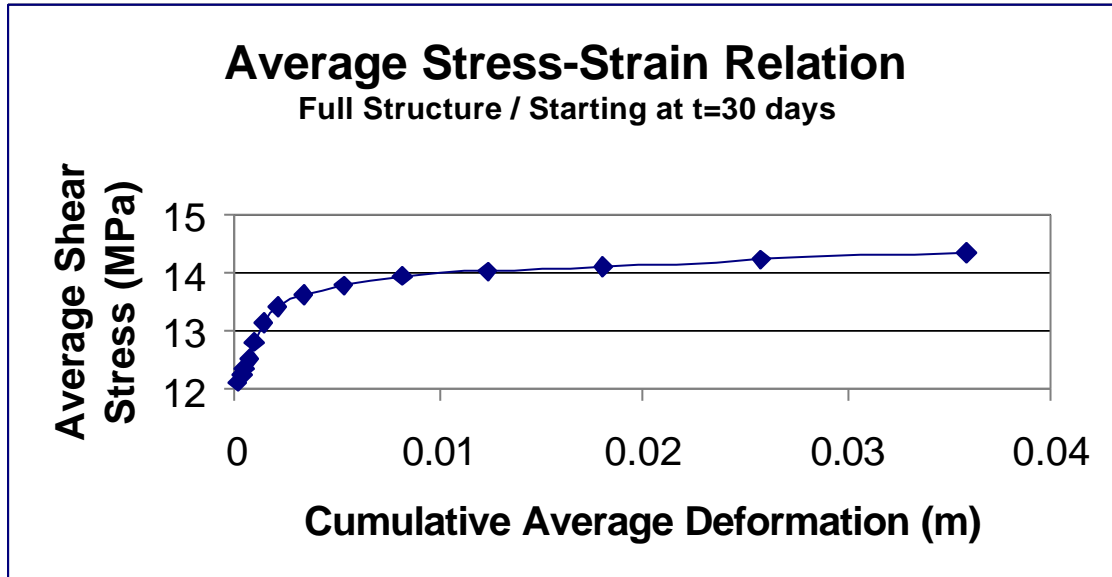


**Figure 4.17 Average Stress-Strain Relation derived from a large spatial window**

Figure 4.16 encompasses a single asperity, and shows strain hardening (positive stiffness modulus reduction), followed by the asperity failure (seismic event). Subsequent to this the discontinuity surface freely deforms with little stress change (no additional asperities present).

Experiment 1 (Figure 4.14) encompasses a number of asperities failing through time (medium size analysis window).

Figure 4.17 includes the whole discontinuity surface modelled. Strain hardening behaviour is shown (positive stiffness modulus reduction), but for the duration of the experiment the structure analysed (entire discontinuity) does not become unstable.

Figures 4.16, 4.14 and 4.17 highlight the influence of the coarseness of the analysis window on the subsequent results. A sufficiently large analysis window (structure) can be shown to be stable and exhibit a positive stiffness modulus. However, structures/volumes of varying degrees of instability can co-exist within this overall stable structure.

### 4.3.2.3. Experiment 3

This experiment analyses changes to the average stiffness modulus derived from the individual modelled instabilities occurring over the discontinuity surface through time.

Figure 4.18 shows a plot of the average instability stiffness modulus (negative stress increments) versus cumulative deformation. This is compared to the total energy released over each time interval. The graph shows the average instability stiffness modulus degrades with time. This stiffness degradation correlates to the increase in total energy released for each time interval. When the instability stiffness modulus is at its lowest level, the greatest amount of energy is released – consistent with a flowing/deforming discontinuity surface resulting in increased seismic activity (hypothesis 3).

Figure 4.19 shows the E-M Relation derived from the cumulative energy and moment source parameters of events occurring within each time period. Although the results are derived from unfiltered data, and the log-log plot of the E-M Relation is generated from cumulative data for each step, again the results are consistent with hypothesis 2 (degrading stiffness resulting from increased volumetric extraction).

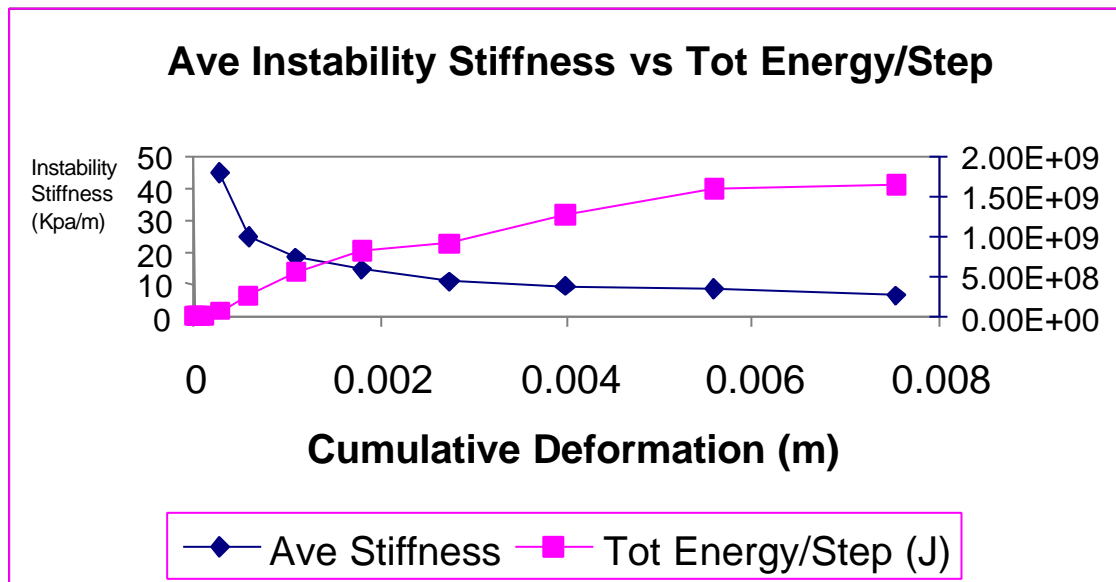
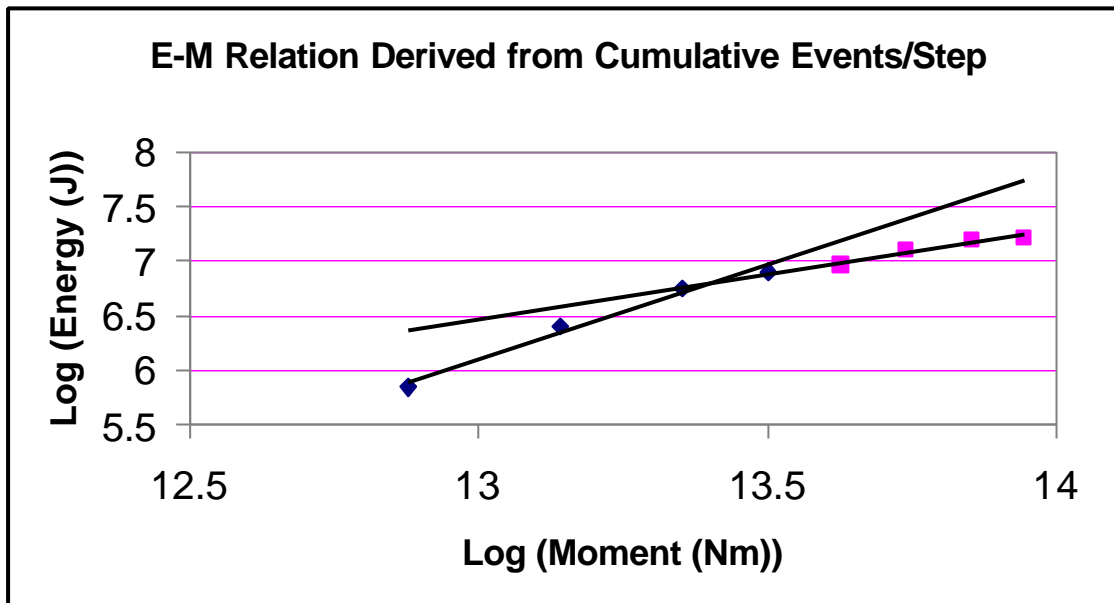


Figure 4.18 Average instability stiffness modulus analysis



**Figure 4.19 E-M Relation derived from cumulative events**

#### 4.4. Conclusions

Observations derived from seismic monitoring indicate both the E-M Ratio and E-M Relation derived from seismic monitoring to change as a result of system stiffness variations. This fundamental concept has important implications for the design and control of mine layouts, both from an observational and numerical modelling perspective. If changes to the response recorded from instabilities as a result of changing system stiffness can be emulated through numerical modelling, efficient mine layout design can be implemented and consistently reconciled to observed instability characteristics derived from seismic monitoring. This will facilitate for the initial integration of numerical modelling with seismic monitoring, and enable the implementation of design as you mine concepts.

Building on the physical observations, the fundamental theory behind system stiffness has been explored in this section. Physical observations are reconciled with the theory and numerical methods are proposed and correlated to the observations through simple idealistic experiments. The results of all the experiments are found to be consistent with the proposed hypotheses. Methods to assess the relative degree of instability of structures are also proposed and correlated to observations.

Finally, extending these results, engineering methods and guidelines to evaluate the seismic potential of mine layouts are formulated in section 5.



## 5. Mine layout design methodology

The unique observations and theoretical concepts developed in the project formed the basis for an improved mine layout design methodology. The methodology developed revolves around the evaluation of the mining induced seismic response associated with mine layouts utilising commercially available modelling tools. In order to implement the method, the designer must:

- delineate either a major geological structure or specific three-dimensional volumes within the rockmass which could be associated with a potential seismic hazard as a result of mining operations,
- incorporate the historic mining layout geometry and sequence into the numerical model,
- where applicable, incorporate the geological structure's three-dimensional geometry into the numerical model,
- delineate and analyse observed seismic events within the specified volume, or associated with the geological structure being analysed,
- undertake model calibration.

The model is calibrated when:

- quantitative deformation values occurring within the volume or along the structure roughly approximates observed deformation values,
- a degree of correspondence is attained between the modelled and observed contours of deformation within the volume or across the structure in both space and time.

Strength heterogeneity can be accommodated for within the rockmass or across the geological structure. The model calibration process ensures the model is emulating the macroscopic mechanical processes occurring along the structure.

Extension of the calibrated model permits the designer to evaluate the following key layout design parameters:

- mine layout (geometrical layout),
- regional/bracket pillars (position and size),
- mine layout sequencing,
- stoping width,
- support design (backfill),
- mining rate.

The design principles that must be applied to attain layout optimisation for a given extraction ratio are:

- the mine layout must result in the average modelled stiffness being maximised;
- the mine layout must limit the spatial variance of the modelled stiffness values around this maximum average. Hence, large gradients of stiffness are minimised as a result of a process of mine layout design optimisation;
- the mine layout must limit the temporal variance of the modelled stiffness values around this maximum average. Hence large gradients of stiffness through time are minimised as a result of a process of mine layout design optimisation.

No specific criterion need be imposed for the design process and adherence to the above design principles will result in the mine layout design being optimised (seismic potential minimised) for a given extraction ratio.

However, even after the mine layout design optimisation exercise is completed, the model must be continually re-calibrated as additional information becomes available. The method caters for the identification of critical parameter assumptions guiding the monitoring programme of the design-as-you-mine philosophy.

The mine layout design method has been extended around the evaluation of the seismic potential of geological structures through the incorporation of the asperity model. In addition to attaining an optimised layout through comparative analyses, the designer can extract a

statistical estimate of the future seismic potential of the geological structure from multiple runs of different random asperity distributions. Firstly, after the application of a detailed model calibration procedure, the engineering modelled design parameters that can now be analysed against alternative mine layouts are:

- spatial position of seismic activity,
- temporal occurrence of discrete seismic events,
- energy released through time and space,
- assessment of the stability of the structure and its relation to the structures seismic potential,
- E-M Relation,
- Gutenberg Richter frequency-magnitude relation.

Secondly, the applied design principles can be extended to include:

- the spatial and temporal occurrence of seismic events and resultant energy released must be carefully evaluated against that of the mining operations,
- the seismic hazard derived from the Gutenberg Richter frequency magnitude relation associated with mining operations must be minimised.

For effective implementation, the mine layout design methodology outlined above is embedded in a set of engineering guidelines. In general, the specific benefits of implementing engineering guidelines are:

- The designer optimally structures his design in accordance with industry accepted standards.
- As a result of the standard structure, aspects of previous designs can easily be incorporated into new designs (enabling a database to be established).
- Physical aspects requiring further investigation will be delineated, highlighting areas to improve or confirm the design.
- The resulting monitoring programme will be structured, and a means to integrate the monitoring results with the design optimisation process will be provided.
- Back analysis of successful or unsuccessful designs will be facilitated for.
- The structured output can be used to assist in quantifying risk.

An example of a stability investigation utilising engineering guidelines and encapsulating the mine layout design methodology is outlined below.

a) Objective:

Task:

**Define the volume of interest for the stability analysis.**

- Clear problem statement, including end goals and objectives of conducting numerical analyses.
- Refine as the modelling proceeds (recursive), and revise at project completion.

Action:

- Delineate the major geological structures within the system and with which the stability investigation will be concerned.
- Define the relevant time frame of the stability investigation for each structure.
  - Major structure through the shaft – life-of-mine.
  - Structure to be mined through – period of mining in the vicinity of the structure.

b) Scope of Work:

Task:

**Detailed list of points that the modelling exercise will test, and physical aspects to be included in the analysis.**

- The list of points must be specific and clearly stated.
- This will constitute the means by which the stated objective will be achieved.
- The extent and exact detail of the modelling must be included.

- All answers that are required from the modelling must be defined.
- The scope must be adequate to cover all the objectives listed.
- Refine as modelling proceeds (recursive).

Action:

- To optimise the designated stability parameters against the mine layout and sequencing in accordance with the design principles over specific delineated volumes.
- To gather and analyse physical observations over the system being analysed.
- To initially calibrate the model to correspond to recorded physical observations.
- To undertake initial analyses based on the calibrated model.
- To recalibrate the numerical models on a continual basis to physical observations through a design-as-you-mine monitoring programme.
- To assess stability of the structures on an ongoing basis and adapt the mine layout in accordance with this investigation.

c) Stability Parameters:

A stability parameter is the quantity with which the stability investigation will be concerned, and which characterises essentially the stability behaviour of the system. The state of the system can be measured on a comparative basis (degree of stability), or utilising a criterion, beyond which instability is defined to occur.

Task:

**Compile a list of stability parameters to be utilised.**

- Choice of stability parameters must be substantiated.
- The stability parameters must be relevant to the volume of interest.

Action:

- **Modelled System Stiffness (MSS)**
- Hill Stability Criterion
- Stress-Strain plots
- E-M Relation plots
- Frequency-Magnitude plots

The stability parameters can be analysed spatially over the structures within the volume of interest or quantitatively within windows defined over the structures. The results of these analyses can be directly compared to that of seismic/non-seismic observations.

d) List of Information:

Task:

**All known parameters to be utilised in the analyses must be included in the list.**

- Available plans
- Known geological structure
- Depth below surface.

e) Constraints:

Task:

**This will consist of a list of all limitations affecting the analysis.**

- The factors must be accompanied by an explanation as to why they constitute a constraint.
- Constraints will assist to determine the assumptions.
- Examples:
  - Time to do the job, cost, amount of data available.

f) Methods (Tools):

Task:

**Choice of modelling tool to be utilised.**

- Reasons must be included as to why the software package is appropriate to achieve the objectives.
- Include a broad outline of the software package.
- Model specific assumptions must be stated.
  - Elastic model, boundary element code, etc.
- Current limitations – all the limitations of the current modelling job must be stated and substantiated, e.g. rheological models will not be incorporated due to time constraint, and the results will be interpolated from experience.

Action:

- Method of analysis utilises a boundary element code (MAP3D) modelling explicit slip, thus facilitating for the accurate representation of layouts and geological structures within the numerical model.

g) Parameter Assumptions:

Task:

**All parameter assumptions to be utilised in the analysis must be included.**

- Appropriate reasons/references must be given for all values assigned to the parameter assumptions listed.
  - Elastic rock mass, friction, boundary conditions, viscosity etc.

h) Calibration:

Task:

*Calibration is the adaptation of the independent variables to obtain a match between the observed and simulated distribution or distributions of a dependent variable or variables (tuning the model). Two step calibrations can be implemented where:*

*Step 1 :*

*independent parameters of the model are adjusted to reproduce the first part of the data.*

*Step 2 :*

*model run and results compared with the second part of the data.*

**Guidelines:**

- Collect results of physical measurements / seismic source parameters to be utilised for model calibration.
- Adjust parameter assumptions to achieve calibration (iterative process).
- Final parameter assumptions used to achieve calibration must represent a physically 'reasonable' scenario, i.e. be consistent with industry accepted values, or past physical measurements of individual parameters.
- Reasons why specific parameters were changed to achieve calibration must be included.

Action:

- Build the mining layout, sequence and geological structures in the model.
- Delineate seismic data or other physical observations over the area and time frame of interest from the seismic database (if available).
- Analyse the seismic data and physical observations to establish model calibration data:
  - Spatial and temporal estimates of seismic viscosity over the structures.
  - Spatial and temporal estimates of inelastic deformation over the structure.
  - Spatial and temporal estimates of the E-M Relations observed.
  - Spatial and temporal estimates of the frequency-magnitude relations observed.
  - Any estimates of the physical structures properties from observations:

- Thickness; degree of hardness; contact description; dip and strike; in-situ stress orientations in close vicinity to the structures.
- The seismic data and physical observations must be analysed through time to undertake the two step calibration procedure.
- Run the model with initial parameter assumptions and compare the results to those derived from physical observations (visual comparison and quantitative analysis).
- Adjust the parameter assumptions, within reasonable limits, to achieve calibration (iterative process).

i) Sensitivity:

Task:

**Guidelines:**

- Sensitivity to be determined against the stability parameters.
- Test all parameter assumptions for sensitivity. This will include two tests consisting of  $\pm 10\%$  change to the original parameter value.

j) Critical Assumptions:

A parameter assumption can be defined to be critical (unstable) if a small change in the initial conditions (input) leads to a large change in the solution (stability parameter).

Task:

**Guidelines:**

- Critical assumptions are parameter assumptions that, when altered, exhibit sensitivity on the stability parameter within the calibrated model.
- Extract from the sensitivity tests, all parameter assumptions for which  $\pm 10\%$  change of the parameter causes a non-linear relationship generated from the stability parameters, and hence must be categorised as a critical assumption (critical in terms of stability).

*Sensitivity limits for critical assumptions:*

- *Non-linear relationship.*
- *Stability Parameter Sensitivity Result / Original Stability Parameter result  $>> 1$ .*
- *Build database.*
- *Back analyse to establish site specific limits e.g. 1.5.*
- Detailed sensitivity analyses must be conducted on all critical parameters in order to establish a clear understanding of the critical parameter variation effects within the calibrated model (e.g. delineate the effects a 30% change of the parameter will have on the model results - stability).
- All the critical assumptions, with attached detailed sensitivities, must be listed on a separate page.

k) Analysis Phase:

**Carry out, within the calibrated model, all analyses / aspects to be tested listed under Scope of Work.**

l) Interpretation / Recommendations:

Task:

**Interpret results of the Analysis Phase.**

- Formulate recommendations within the limits of the calibrated model.
- Use engineering knowledge, and clearly state reasons behind each recommendation.

Action:

- Apply the initial design principles to interpret the results.
- Optimise the layout and sequencing on an iterative basis within the calibrated model to achieve the design principles. The design parameters to be adjusted to comparatively attain an optimised layout are:
  - Mine layout (geometrical layout)
  - Mine sequencing
  - Stoping width
  - Support (backfill)
  - Mining rate
  - Pillars – regional/bracket pillars (position and size)

m) Monitoring Programme:

Task:

**Define monitoring programme to monitor for critical assumptions.**

- If a critical assumption is not monitored for, reasons why must be clearly stated.

Action:

- A general objective is to verify the critical assumptions of the numerical modelling.
- Evaluate the monitoring programme results on a routine basis (e.g. weekly). If drastic change to the system occurs (e.g. a large seismic event), results must be re-evaluated immediately. All the models will be re-evaluated in terms of the defined stability parameters.
- Measure the monitoring results against the critical assumptions sensitivity tables.
- If the sensitivity limits are exceeded, the result will affect the model stability, and the model must be re-calibrated incorporating the 'new information'.
- Updates to the project and the monitoring programme results must be recorded in the form of a database.

This will constitute a 'live' model incorporating new information, and continually optimising model and design results in the form of a recursive design.

## 6. Strong ground motion hazard modelling

### 6.1. Introduction

In the June 1998 mid-year report it was shown how ground motion hazard can be estimated from historical seismic hazard, knowledge of potential source geometry, and numerical modelling. Fundamental inputs into the calculation of PPV is the velocity of slip within the source. This slip velocity represents the maximum possible PPV that will occur, ignoring possible free-surface amplification effects at openings.

It was also described how seismic events, and the resultant ground motion, can be simulated using 'VMAP', a modelling tool based on the isochron method (GAP 211). A possible position for a large event was selected, for example on a fault known to be hazardous, and the source geometry was modelled from the dip and strike of the fault at that position. A number of parameters was assumed, in order to simulate an event of a certain magnitude. It was illustrated how the PPV could be visualised using 3D contours throughout a volume of interest.

It is a topic of study, for a given mining environment, to establish realistic parameters to be used in VMAP.

## 6.2. Slip velocity in a seismic source

The average slip velocity in a seismic source can be calculated simply as:

$$\bar{V}_{slip} = \bar{D} / t_r \quad (6.1)$$

where  $\bar{D}$  is the average slip (displacement), and  $t_r$  is the time during which slip occurs.

The average displacement  $\bar{D}$  can be estimated from the seismic moment for a planar source (Aki, 1966):

$$M_0 = mAD \quad (6.2)$$

where

$M_0$  = seismic moment,  
: = rigidity,  
A = source area

We make use of Brune's model, to estimate the radius of the source area. This model assumes a circular crack seismic event, with constant stress drop  $\sigma$ . The Brune radius is related to the seismic moment as follows:

$$r^3 = \frac{7M_0}{16\sigma} \quad (6.3)$$

The exact manner in which slip occurred at a particular point, can be very complicated, and is fully described by the so-called slip time history. For practical purposes, a 'ramp-like' slip time history model is used, assuming a constant slip velocity over a certain time period, with this time period called the rise time. Therefore, a rupture event on a fault surface can be characterised, amongst other parameters, by the rise time.

According to (Zollo, 1991), the rise time can be obtained from the acceleration waveform. If geophones are used to record seismic events, these velocity seismograms are differentiated to obtain the acceleration waveforms. The duration of the first swing (first half wavelength) of the P-arrival, should correspond to the rise time. This has been confirmed with through generating synthetic waveforms using the isochron method. Events are simulated with different rise times, and the far field acceleration waveforms are then analysed.

### 6.2.1. Distribution of displacement in a source

The average slip (displacement) can be used to calculate the average slip velocity. However, it is of interest to obtain the maximum slip velocity in a source, since this will be the upper limit of possible PPVs at positions away from the source. In this section we consider the distribution of displacement on the source surface. This will enable us to obtain the ratio of maximum displacement relative to average displacement. In practical terms, it means that the average slip velocity has to be multiplied by a certain factor, in order to estimate the maximum slip velocity.

The relative displacement at any position within the source can be described by a function, which is dependent on the position in the source. This function we term the displacement profile. In section 6.2.2 and 6.2.3 two displacement profiles are being described.

We consider the basic definition of average displacement, as used in Equation 6.2. In (Kostrov & Das, 1975), it is shown how Equation 6.2 is derived from the seismic moment tensor, if assumed that the fracture area is planar. In this definition, the average displacement  $\bar{D}$  was defined as the weighted average of displacement over the full source surface, viz.:

$$\bar{D} = \frac{1}{S_A} \int_S d(\vec{r}) d\vec{S} \quad (6.4)$$

where  $d(\vec{r})$  is the displacement on the fault surface at the vector position  $\vec{r}$ , and  $S_A$  is the source area. For a given function of  $d(\vec{r})$ , the value of the maximum relative to the average can be obtained.

In the present study a circular fault surface is assumed, with the displacement a function only of the radial distance from the hypocentre position. Two different types of fault mechanisms are investigated. These are, firstly, the static *circular-crack model*, already mentioned above as the Brune model. Secondly, an *asperity model* is studied, whereby more violent rupturing is expected at the centre of the asperity, giving a larger maximum displacement relative to the average.

## 6.2.2. Static circular-crack model

If a crack is loaded by an initial stress, and the stress drop is uniform over the fault surface, then the solution to static slip of this circular shear crack is given by:

$$D(r) = \frac{24}{7\mu} \frac{\Delta s}{m} (a^2 - r^2)^{1/2} \quad (6.5)$$

with  $r$  the radial distance from the centre of the crack  
 $a$  the radius of the fault  
 $\mu$  the rigidity of the elastic medium surrounding the crack

(Kanamori and Boschi, 1983)

This function is shown in Figure 6.1.

The average displacement (weighted according to the above function), is then obtained by integrating over the full surface, and dividing by  $\pi a^2$ , the surface area, and gives the following:

$$\bar{D} = \frac{16}{7\mu} \frac{\Delta s}{m} a \quad (6.6)$$

If we now take the ratio  $\bar{D} / D(0)$ , we find the factor 2/3, meaning that the maximum displacement is a factor 1.5 larger than the average displacement (note that this is independent on source parameters, it is solely a result of the displacement profile).

## 6.2.3. Asperity model

In this model a seismic event is caused by the failure of an isolated, highly stressed region of the fault. The rest of the fault surface that also slips, gives relatively low resistance to slip, and contributes little to the total stress drop (Kostrov & Das, 1975). In this model the stress drop is not uniform over the source. We denote the radius of the asperity by  $r$ , and the radius of the full source surface by  $R$ . When the central asperity breaks, a large displacement follows over the asperity region  $r$ . The dynamic slip then spreads out over the entire circular fault, causing relatively low displacement over that large region (between  $r$  and  $R$ ). It is expected from this model that the maximum displacement (in the asperity region) is very large relative to the average displacement.

In (Kostrov & Das, 1975) the seismic moment of an asperity model event ( $M_0^{asp}$ ) is derived as:

$$M_0^{asp} = 1.19 \frac{16}{7} \Delta s R^3 \left( \frac{r}{R} \right) \quad (6.7)$$



If the factor 1.19 is replaced by 1, we can ( $M_0^{cr}$ ) compare the moment for this model with that of the constant stress drop circular-crack model, as described in Section 6.2.2. This comparison is:

$$M_0^{asp} \approx M_0^{cr} \left( \frac{r}{R} \right) \quad (6.8)$$

For two events of the same source radius, the moment of the asperity model event is  $r/R$  times lower than that of the crack model event. From Equation 6.2 it follows that the average displacement is also lower. Since the source size is the same, the lower average displacement can only be explained by the shape of the displacement profile. The region towards the edge of the circular asperity, which is of larger area per radial increment, should therefore have relatively low displacement, in order to give the low overall average displacement. (Keep in mind Equation 6.4, showing the calculation of the weighted average displacement.)

Although the above discussion does not provide quantitative information towards the shape of the displacement profiles of the two models, it does suggest that for the asperity model, the maximum displacement over average displacement ratio should be larger than that of the crack model.

In order to gain some understanding of the shape of the displacement profile, a simple UDEC model was set up. A fault plane was modelled ahead of an opening. Since maximum shear stress on the fault would be present some distance below the opening, an asperity was modelled at that position. The modelled fault thus consisted of an asperity with high frictional strength, with the rest of the fault plane being weak. After initial equilibrium was reached, the asperity was allowed to fail, with resulting displacement along the fault. The difference in displacement after and before failure was evaluated, since we are interested in the coseismic displacement.

The above model geometry is shown in Figure 6.2, with some of the model parameters used given in the caption. The resulting displacement profile is shown along the entire fault length.

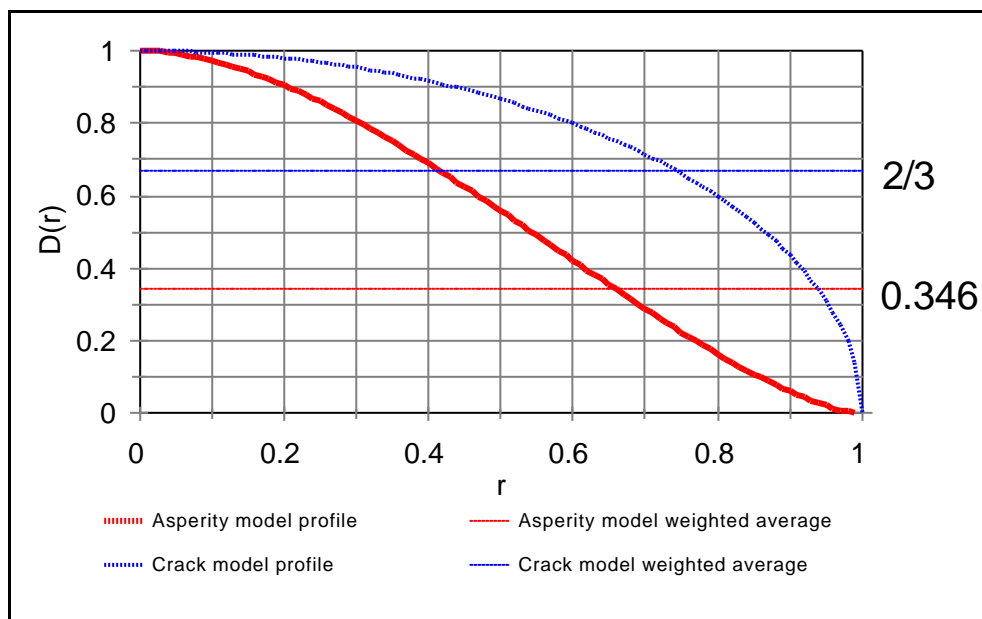


**Figure 6.1 Displacement profiles of the two models tested, shown with the weighted average displacements.**

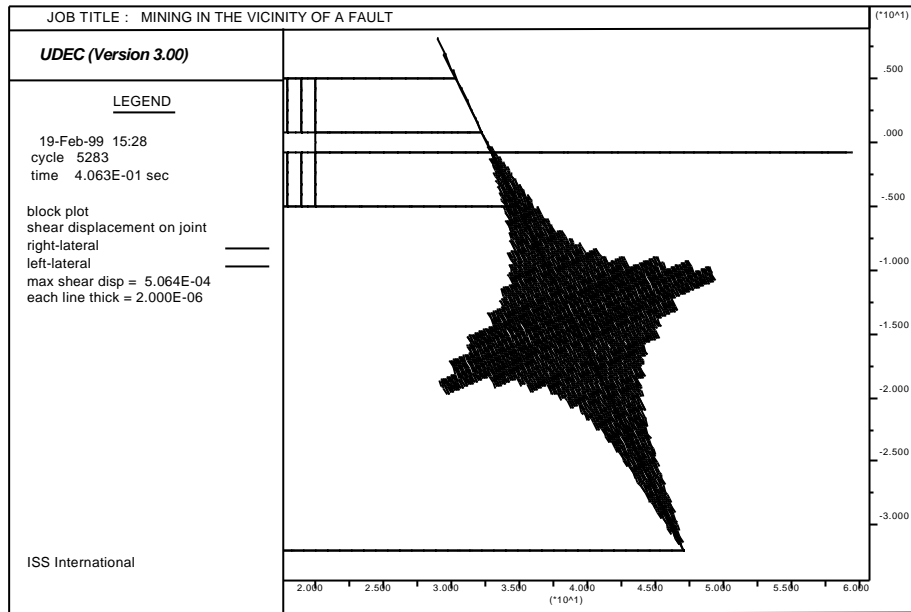


**Figure 6.2 UDEC modelling results. The displacement, due to coseismic slip, is shown along the fault plane. Note that the maximum displacement is only 0.5mm, over a fault length of 35m. However, the excavation is only 20m long, and at a horizontal distance of 12m from the fault. Of note here is the shape of the profile, which may be represented by a graph with the x-axis normalised to the source radius, and y-axis normalised to the maximum displacement.**

A displacement profile has been derived theoretically (Walsh & Watterson, 1987) from an elastic single slip event profile and a fault growth model. This profile is shown in Figure 6.1, and the function is as follows:

$$d(r) = 2\sqrt{\frac{(1-r)}{2} - r^2(1-r)} \quad (6.9)$$

The profile was shown to represent the displacement on a fault surface due to natural creep well.

In our case the profile is used to determine the displacement occurring during a mining induced slip event. Although this scenario differs to natural creep on a fault, we postulate that the displacement on a fault due to natural creep over long time periods, represents a worst case scenario. The displacement was allowed to increase, up to such a stage that no more creep was possible due to physical constraints imposed by the surrounding volume of rock. 'Worst case' means in this case the maximum possible displacement relative to the average displacement.

The average displacement is calculated from the above equation (using polar coordinates) as follows:

$$\bar{D} = \frac{\int \int r dr dq D(r, q)}{pR^2} \quad (6.10)$$

with  $D(r, 2)$  a general displacement profile as a function of the radius and azimuthal angle.

$$\therefore \bar{D} = 2p \int_0^1 d(r) r dr / p \quad (6.11)$$

with  $d(r)$  the displacement profile used here.  $r$  is normalised to the source radius.

This integral gives a value of 0.3458 for the average displacement, when the maximum of  $d(r)$  is unity. For a maximum different to unity, the average displacement must be divided by 0.3458, i.e., the following applies:

$$D_M = 2.9\bar{D} \quad (6.12)$$

Therefore, if the average displacement is obtained from the moment and source area, this value should be multiplied with 2.9 to get an estimate of the maximum displacement in the source.

#### **6.2.4. Asperity model vs. circular crack**

We offer the above two models as limiting cases for the maximum displacement over average displacement. The rupture mechanism of a seismic event will contain elements of both models. The larger events will usually be asperity failure type events, while circular crack events will represent fracturing ahead of mining excavations. The multiplication factor to obtain maximum displacement from average displacement, will therefore vary between the factors as quoted above, viz. 1.5 and 2.9. However, for the analysis to follow, we are concerned with the maximum possible slip velocity expected, and therefore the value based on the asperity model will be used.

### **6.3. Analysis of recorded seismic events**

It was mentioned that the rise time can be estimated from an acceleration waveform, by identifying the first 'swing' (half-wavelength) of the P-arrival. This has been done for a number of events of different magnitude. The waveforms were first 'rotated', to get one component aligned with the incoming wave. This waveform was then differentiated, to give the acceleration waveform.

We found that it is possible to identify the first swing of the P-arrival fairly easily, and hence read off the time duration of that. These times were noted, together with the source parameters. Events were selected to be within such a range from the sensors, that the far-field condition is satisfied. On some seismograms it was not possible to obtain a reliable reading of the rise time, and these were discarded. It was attempted to get readings from at least 3 seismograms of an event, from which the average could be calculated.

The average displacement (slip) is obtained from the moment and source area, which is in turn estimated from the Brune radius. From the slip and rise time the average slip velocity is calculated. The average slip velocity is multiplied by a factor according to the displacement profile (2.9 was used in this case).

#### **6.3.1. Slip velocity databases**

A system was set up whereby the above analysis can be done routinely. Tables 6.1 to 6.3 shows the data-sets analysed in the current study.

The data-sets are the following (Tables 6.1, 6.2 and 6.3 respectively):

- Database 1 (Welkom area) - Events larger than local magnitude 2.5 for 1992
- Database 2 (Far West Rand) - Events from 1998 and 1999
- Database 3 (Welkom area) - Events larger than magnitude 0 for 1997 and 1998

### 6.3.2. Relationship between stress drop and slip velocity

A linear relationship between slip velocity and stress drop can be derived for a static circular crack (McGarr 1991, Kostrov & Das, 1975, Kanamori & Boschi, 1983). The equation of slip velocity vs. stress drop, has zero intercept, with gradient the shear velocity divided by rigidity, i.e.

$$V_{slip} = \frac{b}{m} \Delta s \quad (6.13)$$

This has been tested on the data sets shown in Tables 6.1 to 6.3. Figures 6.4 to 6.6 shows the average slip velocity plotted against stress drop.

In Figure 6.3 a linear relationship can be seen up to a stress drop of approximately 50 bar, after which data is scattered. The same can be seen in Figure 6.5, up to a stress drop of approximately 10 bar. It appears therefore that a simple linear relationship cannot be observed over the full range of stress drops for these two data-sets.

The above can be explained, considering the probable complex behaviour during slip, especially for the larger events. For the small events, the mechanism can usually be approximated by a static circular crack model, as described in Section 6.2.2. In this case, the approximation of rise time being constant, will be appropriate. The single crack is responsible for the full stress drop. Note that the rise time is obtained from the first swing in the acceleration spectrum. However, for the larger events, this approximation will not be appropriate, since these events are generally complex, i.e. consisting of more than one subevent. The first swing represents the first subevent, while most of the energy associated with the maximum stress drop may radiate from a second or third subevent.

Figure 6.6 shows the results of Database 2. Apart from one outlier, there appears to be a linear relationship over the full range of stress drops. The gradient of the linear fit is 20.7. The linear relationship in this case is probably due to the particular mining environment, with its typical source mechanisms. The data is from the Far West Rand, where the stress is higher than for the other cases, due to the greater depth. The faults are also stiffer in general.

We need to estimate the rise time for the VMAP simulation to follow. In order to illustrate the approach followed, Equation 6.13 is used to estimate the gradient of the slip velocity vs. stress drop relationship. If a rigidity of  $3E10$  is assumed, and a shear wave velocity of 3500 m/s, the gradient is calculated as 12 (with slip velocity in [mm/s] and stress drop in [bar]).

**Table 6.1: Seismic database 1 (Welkom area), large events during 1992. The rise time was obtained from the duration of the first swing of the acceleration waveform, and the average displacement was obtained from the source area and seismic moment. The average displacement is multiplied with a factor according to the displacement profiles used, to obtain an estimate of the maximum slip velocity in the source.**

Local magnitude	Static stress drop [bar]	Av rise time [ms]	Average slip [mm]	Av Slip vel [mm/s]	Max Slip vel [mm/s]
3.9	196.43	39.33	101.03	2568.64	7449.06
2.8	41.85	18.00	16.98	943.14	2735.11
3.0	21.06	35.00	15.13	432.30	1253.66
3.2	153.73	25.33	44.76	1766.93	5124.11
2.6	10.97	21.33	4.14	194.27	563.38
2.8	99.92	15.50	13.04	841.45	2440.21
2.6	93.36	12.00	8.04	669.69	1942.09
2.6	43.13	17.33	9.96	574.66	1666.50
3.2	132.68	24.00	26.48	1103.32	3199.64
3.2	38.03	24.00	13.60	566.57	1643.06
2.5	17.33	25.71	6.47	251.46	729.23
3.2	57.06	29.00	19.11	659.02	1911.17
3.3	85.63	18.80	31.58	1679.57	4870.75
2.9	31.79	24.50	12.46	508.74	1475.35
2.6	51.27	16.40	5.04	307.52	891.82
2.8	27.06	21.00	10.52	501.08	1453.13
2.5	3.50	32.40	3.05	94.20	273.17
3.0	47.36	14.00	17.61	1257.73	3647.41
2.9	80.36	19.60	21.90	1117.43	3240.54
2.7	42.84	17.00	10.79	634.94	1841.32

**Table 6.2: Seismic database 2 (Far west rand), large events during 1998 and 1999. See Table 6.1 for more information.**

Local magnitude	Static stress drop [bar]	Av rise time [ms]	Average slip [mm]	Av Slip vel [mm/s]	Max Slip vel [mm/s]
1.7	184.61	9.50	10.05	1057.40	3066.45
1.7	8.75	14.50	2.95	203.20	589.27
2.4	12.97	35.50	6.77	190.67	552.94
1.7	8.13	19.37	1.89	97.80	283.62
2.5	25.46	26.75	9.52	355.91	1032.14
3.1	59.43	30.50	31.58	1035.25	3002.21
1.8	32.92	10.80	5.11	473.17	1372.21
3.2	123.12	19.89	49.93	2510.90	7281.60
2.1	65.67	8.93	11.61	1299.29	3767.95
2.6	26.44	25.21	12.48	495.07	1435.69
2.6	45.69	19.21	17.07	888.36	2576.24

**Table 6.3: Seismic database 3 (Welkom area), events during 1997 and 1998. See Table 6.1 for more information.**

Local magnitude	Static stress drop [bar]	Av rise time [ms]	Average slip [mm]	Av Slip vel [mm/s]	Max Slip vel [mm/s]
1.0	4.88	8.38	0.71	84.34	244.58
1.2	38.53	8.67	1.84	212.48	616.18
1.0	15.46	5.00	1.38	275.08	797.74
1.5	7.84	8.67	1.62	187.42	543.51
1.2	4.86	15.71	0.93	59.29	171.94
1.3	1.31	9.20	0.48	52.68	152.76
1.1	28.93	7.92	1.93	244.12	707.95
1.2	71.67	9.07	3.46	381.76	1107.10
1.1	22.11	6.00	1.76	293.71	851.76
2.2	6.17	14.70	2.92	198.83	576.60
2.8	8.79	5.84	1.30	222.06	643.97
1.2	2.62	7.83	0.68	86.80	251.71
2.0	2.23	20.24	1.46	72.30	209.67
1.1	3.05	14.08	0.63	44.65	129.47
2.8	21.35	26.13	24.06	920.95	2670.74
1.6	3.59	10.43	1.18	113.26	328.45
1.5	1.85	8.38	0.80	95.36	276.55
2.3	6.58	22.63	3.76	166.27	482.18
1.5	4.97	9.90	1.21	122.06	353.98
1.40	6.08	7.50	1.20	160.46	465.33
2.60	7.73	12.08	5.37	444.31	1288.49
1.80	4.88	13.40	1.67	124.35	360.63
2.30	10.07	17.92	3.99	222.42	645.02
1.60	5.68	11.47	1.57	136.71	396.47
1.60	22.15	11.28	1.77	156.49	453.83
2.60	23.30	17.83	21.51	1206.11	3497.73
1.60	25.00	15.38	3.03	196.94	571.12
1.7	8.76	10.58	2.23	210.57	610.67
0.1	4.07	5.33	0.26	49.44	143.38
0.8	11.22	6.19	0.50	81.20	235.47
0.0	2.23	6.13	0.15	24.60	71.35
0.7	0.81	12.34	0.19	15.07	43.70
0.5	4.07	5.68	0.41	71.97	208.71
1.1	21.92	7.88	1.11	140.46	407.34
1.4	20.90	6.14	2.39	389.83	1130.52
1.3	10.36	9.57	1.66	173.05	501.85
1.5	19.72	7.13	2.12	297.49	862.71
1.4	11.91	5.17	3.28	634.58	1840.28
1.1	13.17	10.38	1.25	119.95	347.86
1.8	8.47	21.08	2.71	128.58	372.89
2.0	12.25	12.50	4.13	330.10	957.29
1.4	4.76	9.50	1.18	123.91	359.35
1.0	4.61	7.92	0.79	99.71	289.15
1.3	22.17	7.56	2.08	275.48	798.88
1.4	2.97	12.30	0.91	74.36	215.66
1.2	33.25	6.26	1.89	301.05	873.04

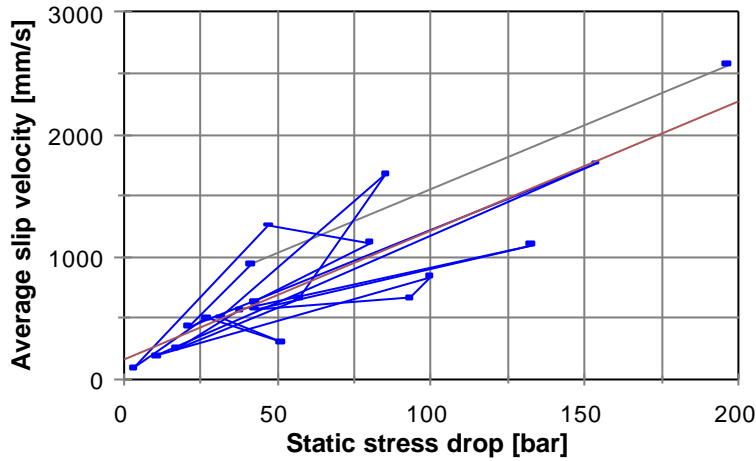


**Figure 6.3** Data from the Welkom Area (Table & Database 6.1). The gradient of the linear regression line is 10.5.

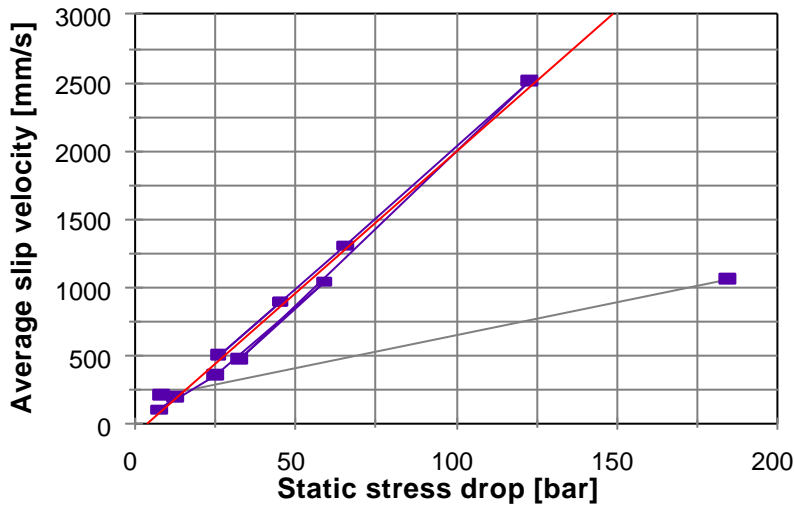


**Figure 6.4** Data from far West Rand (Table & Database 6.2). The gradient of the linear regression fit is 20.7.

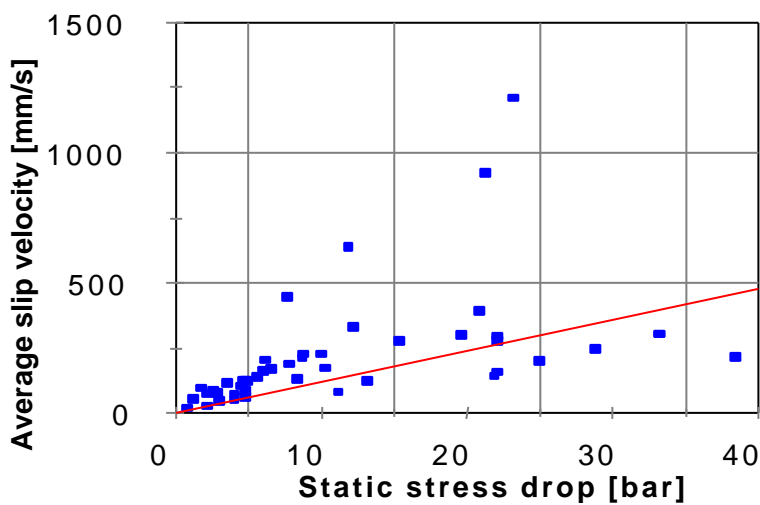


**Figure 6.5** Data from Welkom area (Database & Table 6.3). The gradient of the linear fit is 12.

## 6.4. VMAP event simulations

### 6.4.1. Simulation of PPV of a large event on a fault

A VMAP simulation is used here to estimate PPVs at distances from a source. A simple mining geometry is modelled, as shown in Figure 6.6. A rectangular fault of dimension 150 by 150 m, with a dip of 90 degrees, is modelled. This fault is allowed to slip, with constant rise time, as well as displacement along the rupture. PPVs are calculated for different groups of points, at the same orthogonal distance from the fault, but at different projected positions on the fault plane, to capture the variations in PPV due to the radiation pattern.

The full set of parameters used in the simulation are:

Rake [degs]	Rupture velocity [m/s]	slip velocity / stress drop gradient	rigidity	Displacement profile multiplication factor
90	2590	12	3E+10	2.9

Source area [m <sup>2</sup> ]	Moment magnitude	Stress drop [bar]	Average slip velocity [m/s]	Maximum slip velocity [m/s]	Displacement (slip) [m]	Rise time [msec]
22500	3	200	2.0	5.8	0.066	11.41

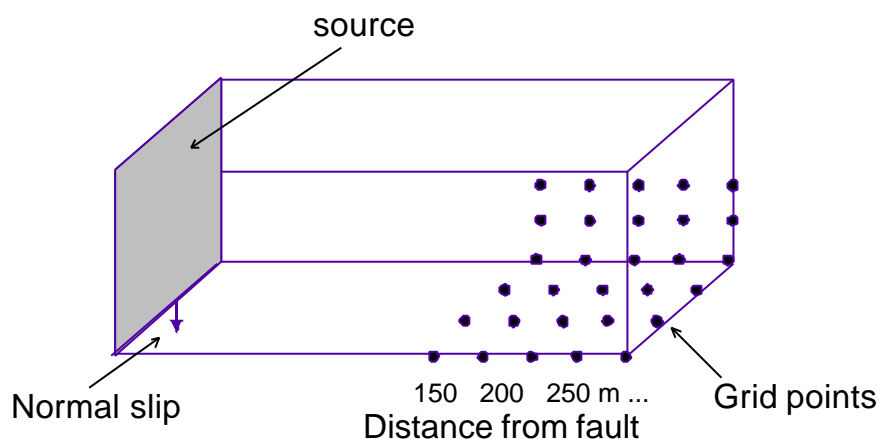


**Figure 6.6 Illustration of modelled source, showing grid points where PPVs were calculated relative to source plane.**

Figure 6.7 shows the PPVs simulated from VMAP, and it can be seen how the PPV drops at larger distances from the source. Since no assumptions are made of the initiation point relative to working places/development, the maximum PPV envelope should be taken as the worst case ground motion to be expected in the vicinity of the fault.



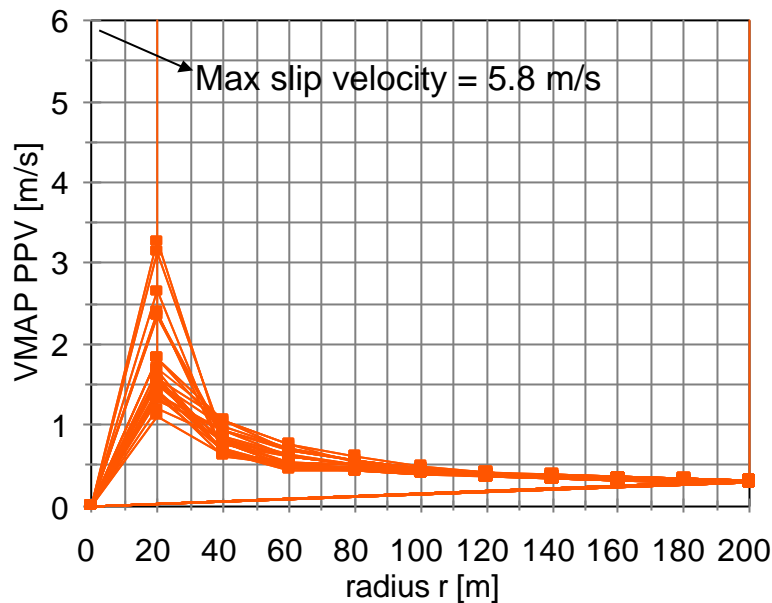


**Figure 6.7** Graph showing VMAP PPVs at distances from the source. Note: The maximum slip velocity represents the worst possible case. In terms of the model, the smallest value would be 3m/s and the rest of the graph would adapt accordingly.

#### 6.4.2. Simulation of event in an actual mining situation

In this section it is illustrated how the current method may be used in a real mining situation. A mining area was selected, where a longwall, lagging behind the two surrounding longwalls, was mined through a fault. A large event was simulated on the fault surface, and the resulting ground motion was calculated from VMAP.

From the mining layout it was possible to predict the size and position of a potential large event on the fault. From Gutenberg Richter hazard analysis,  $M_{max}$  was estimated, and a worst case stress drop was assumed. The slip direction (rake) could be estimated from the modelled shear stress. A constant rupture velocity and rise time was assumed, as well as displacement on the fault surface.

Following are the relevant parameters used in the simulation:

Source area [m <sup>2</sup> ]	Moment magnitude	Stress drop [bar]	Average slip velocity [m/s]	Maximum slip velocity [m/s]	Displacement (slip) [m]	Rise time [msec]
40000	3.5	250	2.5	7.3	0.2	28.9

In addition to ground motion simulation, it is also possible to incorporate stress modelling parameters into the simulation. In the current study, a simple elastic MAP3D model was set up, and the various stress values were calculated on different planes. These planes were then combined, to form a 3D grid of data points, from which isosurfaces of the stress components can be obtained.

Figure 6.8 shows the mining layout together with an isosurface of sigma 1 stress, at a value of 166 MPA. The rectangular fault along the bigger fault surface can also be seen. In Figure 6.9 then, various isosurfaces of PPV are shown, as indicated.

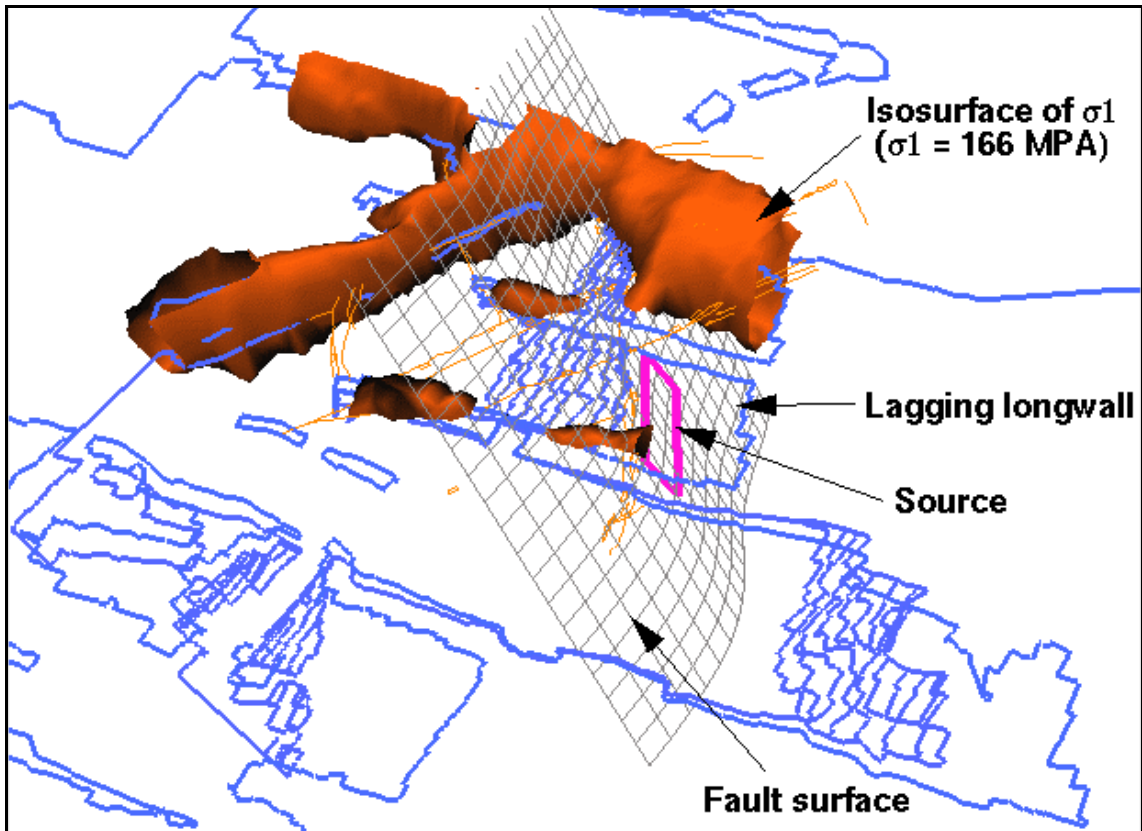


**Figure 6.8** General layout of area. An event of moment magnitude 3.5 was simulated at the position indicated by “Source”, to approximate an event caused by failure to the entire longwall. The isosurface of sigma 1 stress was obtained from an elastic MAP3D model.

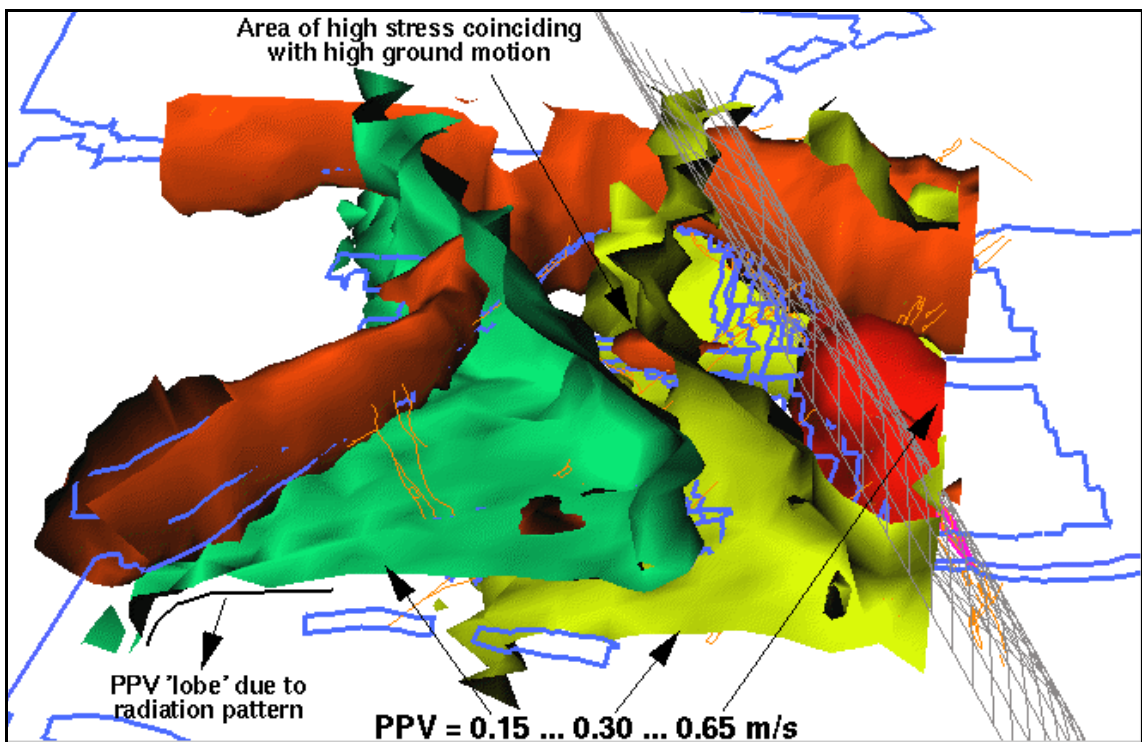


**Figure 6.9** Isosurface of PPVs as indicated. Areas of high damage potential can be identified where high stress coincides with high ground motion. The radiation pattern causes high ground motion in the footwall development area.

It is now possible to estimate possible damage to development, stopes, etc. This is done by considering areas of high stress together with areas which could be expected to experience a high degree of ground motion. In the current case it is of interest that, due to the radiation pattern, the footwall development experienced higher ground motion than the mining areas closer to the event. This can be seen from the 'PPV lobes' as indicated.

## 6.5. Ground motion hazard modelling: The isochron method

Peak particle velocity (PPV) at a given site can be predicted using isochron formalism and kinematic modelling of seismic sources. Traditionally this type of modelling has been carried out using finite difference/element methods. In such case a grid of point dislocations simulates the large (or extended) source. Further, the integrals over the fault surface are replaced by summations of all point sources, and the synthetic seismograms are calculated for each of the point sources using finite difference/element methods. These methods are computationally extremely expensive. Recently developed new ray-theory based wave propagation algorithms allow fast calculation of far-, intermediate- and near-field synthetics.

It has been shown (*Joyner and Spudich, 1994*) that for a uniform whole space the various terms in the Green's function can be transformed into sums of nondispersive pulses. In this case the contributions of the far-, intermediate- and near- fields can be calculated directly in the time domain, and the total wavefield can be represented as a sum of all above terms. Advantages of such an approach are obvious:

We can use isochron formalism, which proved to be very efficient for computing synthetic seismograms using far-field ray-theory Green's functions for finite fault radiation problems (*Bernard and Madariaga, 1984, Spudich and Frazer, 1984*), and still retain near and intermediate field contributions. The isochron integration technique proved to be helpful for gaining insight into the fine structure of the source processes and can explain many peculiarities of the near-source range waveform behaviour. Very complex seismic sources can be described and modelled without having to use complicated and time-consuming computations.

This algorithm for producing synthetic seismograms using isochron formalism is based on ray theory. It combines the isochron integration method in the vicinity of the source for computation of far, intermediate and near field contributions and the powerful recursive cell raytracing (or another type of wavefront construction waveform modelling) for far-field synthetics at some distance from the source. In the vicinity of the source, the geological medium is assumed to be homogeneous and isotropic, while for the far-field approximation almost any arbitrarily complex three-dimensional geological medium model can be used.

Below we briefly describe the algorithm and show some examples for the Haskell source model.

### 6.5.1. Algorithm for synthetic seismograms calculations using isochron method

#### 6.5.1.1. Input information

Used algorithm requires the following input information:

- Source plane dimensions and geometry: strike, dip, dimensions. Although in the following we consider only rectangular shape fault geometry, the extensions of the proposed algorithm to other source geometry configurations are rather straightforward.
- Rupture time distribution on the source plane. It must be specified on some two-dimensional grid along the fault surface. This is the grid on which the initial fault rectangle is subdivided for further calculations.
- We assume that the same "ramp-like" slip time history function is applicable for each point of the source plane:

$$\Delta u(\vec{r}_0, t) = \begin{cases} 0, & 0 < t < t_r(r_0) \\ (t - t_r) D_0 / t, & t_r(r_0) < t < t_r(r_0) + t \\ D_0, & t > t_r(r_0) + t \end{cases} \quad (6.14)$$

where  $\Delta u(\vec{r}_0, t)$  is the scalar slip function,  $D_0$  is the final dislocation at the point  $r_0$ ;  $t_r$  is the rupture time;  $t$  is the rise time. Generally, values of  $D_0$  and  $t$  may vary from point to point on the source surface, but initially we can assume that they are the same for all points. It must be pointed out that the time derivative of the scalar slip function shown above is a simple boxcar function, with amplitude equal to  $D_0/t$  and a width  $t$ .

- The effect of anelastic attenuation can be included by the convolution in the frequency domain of the Green's function with the constant Q attenuation function defined by (Carpenter, 1966):

$$Q(f, t^*) = \exp \left[ -p f \frac{t^*}{2} - i 2p f t^* \ln \left( \frac{f}{f_N} \right) \right], \quad (6.15)$$

where  $t^* = T_c/Q$ ,  $T_c$  is the body wave travel time,  $Q$  is the constant "quality factor",  $f$  is the frequency, and  $f_N$  - Nyquist frequency.

### 6.5.1.2. Ray theoretical strong ground motion modelling

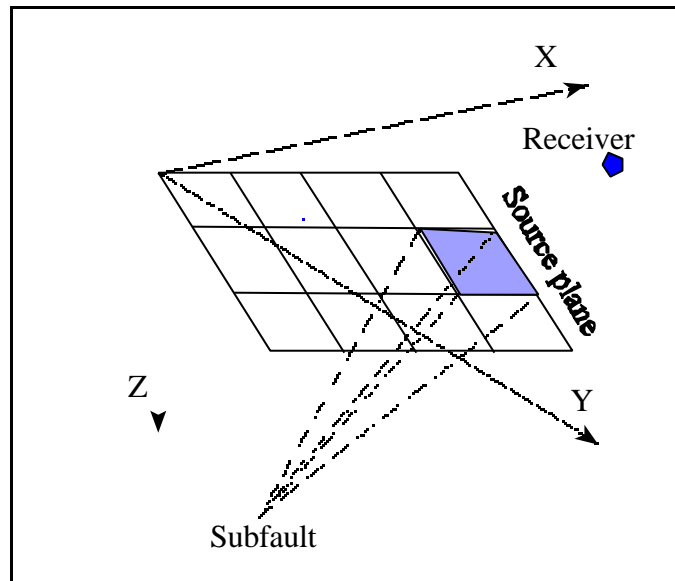


**Figure 6.10 Fault geometry and source parameterisation**

Now we will formulate initial conditions and outline the strategy of synthetic seismogram calculations.

- The source is divided into several equal size rectangular subfaults (Figure 6.10). The slip at each subfault is specified by the ramp-like function (6.14). Let us assume that the size of each elementary subfault is  $\Delta x$  by  $\Delta y$ , and  $M$  and  $N$  are the numbers of subfaults in the  $X$  and  $Y$  directions respectively.
- Modelling assumes that the rupture times, the final dislocation values and the rise times are specified for every grid point, i.e. at the subfault corners. For every receiver location it is necessary to calculate the travel-times from the receiver position to the subfault corners.
- Then isochron times can be obtained by summing rupture times and travel-times from the receiver to the subfault corners. For isotropic, homogeneous media simple Green's functions can be used. For more complicated geological media one can use wavefront construction/recursive cell ray-tracing methods. But this is only applicable to the far-field P and S waves contribution only. For the isotropic and homogeneous media and for the

receivers in the near- or/and intermediate field we can use simple (or relatively simple) relations from *Joyner and Spudich (1994)* which are discussed below. Once isochron times are known at the subfault corners, then the isochron times at any point of the subfault element ( $m, n$ ) are obtained by the interpolation formula (*Yoshida, 1986*):

$$t(x, y) = \frac{1}{\Delta x \Delta y} [(\Delta x - x)(\Delta y - y)T_{m,n} + (\Delta x - x)yT_{m,n+1} + (\Delta y - y)xT_{m+1,n} + xyT_{m+1,n+1}] \quad (6.16)$$

where  $T_{i,j}$ , ( $i = m, m + 1$ ;  $j = n, n + 1$ ) are the isochron times at the subfault corners.

- The subfault dimensions are considered to be small enough, so that the direction cosines and geometrical spreading do not vary over subfault surfaces, i.e. the Fraunhofer approximation is applied at the subfault scale. This implies that the propagation effects on pulses radiated from any point on the subfault are approximately the same and that they can be described by a representative subfault Green's function computed for the ray leaving the middle point. Then, using this approximation, we can write the representation integral for a discretized source plane:

$$u^c(r, t) = \sum_m n u_{m,n}^c(r, t), \quad (6.17)$$

$$\text{where } u_{m,n}^c(r, t) = G_{m,n}^{FF} \otimes \int_{\text{subfault}} \Delta u^{m,n}(r_0^{m,n}, t - T_c^{m,n}) d\Sigma \quad (6.18)$$

For a given time  $t$  and a boxcar slip velocity function (i.e. "ramp-like" slip function) the subfault regions  $S_0$ , where the slip velocity is not vanishing is bounded by isochrons  $L_t = x(t, y)$  and  $L_{t-t} = x(t - t, y)$  and the edges of the subfault.

- Once the isochrons have been calculated for a given position of the receiver we can determine the separate contributions of far-, intermediate- and near field using:

$$\begin{aligned} \frac{\partial^2 u^N(x, t)}{\partial t^2} &= \frac{m}{4pr} \left[ \int_{-\infty}^{+\infty} dt \frac{d}{dt} h(t - t) \left( \int_{t_a+t_r=t} dl \frac{D_0 t_a \mathbf{A}^N}{r^4 |\nabla t|} - \int_{t_b+t_r=t} dl \frac{D_0 t_b \mathbf{A}^N}{r^4 |\nabla t|} \right) + \int_{-\infty}^{+\infty} dt h(t - t) \left( \int_{t_a+t_r=t} dl \frac{D_0 \mathbf{A}^N}{r^4 |\nabla t|} - \int_{t_b+t_r=t} dl \frac{D_0 \mathbf{A}^N}{r^4 |\nabla t|} \right) \right] \\ \frac{\partial^2 u^{IP}(x, t)}{\partial t^2} &= \frac{m}{4pra^2} \int_{-\infty}^{+\infty} dt \frac{d^2}{dt^2} h(t - t) \int_{t_a+t_r=t} dl \frac{D_0 \mathbf{A}^{IP}}{r^2 |\nabla t|} \\ \frac{\partial^2 u^{IS}(x, t)}{\partial t^2} &= \frac{m}{4prb^2} \int_{-\infty}^{+\infty} dt \frac{d^2}{dt^2} h(t - t) \int_{t_b+t_r=t} dl \frac{D_0 \mathbf{A}^{IS}}{r^2 |\nabla t|} \\ \frac{\partial^2 u^{FP}(x, t)}{\partial t^2} &= \frac{m}{4pra^3} \int_{-\infty}^{+\infty} dt \frac{d^3}{dt^3} h(t - t) \int_{t_a+t_r=t} dl \frac{D_0 \mathbf{A}^{FP}}{r |\nabla t|} \\ \frac{\partial^2 u^{FS}(x, t)}{\partial t^2} &= \frac{m}{4prb^3} \int_{-\infty}^{+\infty} dt \frac{d^3}{dt^3} h(t - t) \int_{t_b+t_r=t} dl \frac{D_0 \mathbf{A}^{FS}}{r |\nabla t|} \end{aligned} \quad (6.19)$$

where  $u^N, u^{IP}, u^{IS}, u^{FP}, u^{FS}$  are the near, intermediate P, intermediate S, far P and far S field displacements respectively,  $A^N, A^{IP}, A^{IS}, A^{FP}, A^{FS}$  are the near, intermediate P, intermediate S, far P and far S radiation patterns,  $h(t - I)$  is the slip time history, which is assumed to be the same along the source surface, but normalised by its maximum value,  $D_0$  is the final dislocation, which may vary along the source surface,  $|\tilde{\nabla} t|$  is the gradient of  $J$ . The equations  $I = t + t_r$  and  $I = t_s + t_r$  describe a family of isochrons on the rupture surface. As becomes apparent from consideration of the system of equations (6.19) shown above, all of

the differential equations require integration along the P and/or S wave isochrons, but each with a different integrand value. It should also be pointed out that using the above approach, contributions of the near, intermediate and far fields could be computed separately for different types of waves, except the near field. The inner integral in system (6.19) is the integral along the isochrons, while the outer integral can easily be recognised as the convolution, which can be calculated using the Fast Fourier Transform algorithm. Using the frequency domain approach for the computation of convolution may also help to alleviate numerical problems arising from the discontinuity of the slip function model defined by equation (6.14), used in Haskell's model (In this case one could use the slip velocity function to calculate the Fourier Transform (FT) to obtain a value of  $\frac{\partial h(t)}{\partial t}$  and then in order to obtain the FT of  $h(t)$ , division in the frequency domain by  $i2Bf$  could be used for all  $f$  not equal to zero). After every individual component of acceleration is computed according to equation (6.19), then the total acceleration can be evaluated by simply summing all the terms:

$$\begin{aligned} \frac{\partial^2 u(x, t)}{\partial t^2} = & \frac{\partial^2 u^N(x, t)}{\partial t^2} + \frac{\partial^2 u^P(x, t)}{\partial t^2} + \frac{\partial^2 u^S(x, t)}{\partial t^2} \\ & + \frac{\partial^2 u^{FP}(x, t)}{\partial t^2} + \frac{\partial^2 u^{FS}(x, t)}{\partial t^2} \end{aligned} \quad (6.20)$$

Once the total acceleration seismogram is evaluated, then, by using a numerical integration procedure velocity and displacement seismograms can be obtained.

## 6.6. Conclusions

In this study it was attempted to obtain estimates of parameters required for VMAP. It was sought, in particular, to estimate the slip velocity in a seismic source. Towards this end, a technique was developed to measure the rise time of an event from seismograms. Furthermore, from an estimate of the source area, the average slip can be calculated, and this, together with the rise time, then gives the average slip velocity. The ratio of maximum slip velocity to average slip velocity, due to the distribution of slip along the source surface, was also considered. The maximum slip velocity of an event can be taken as the maximum possible PPV caused by the event (ignoring free surface effects).

It was then attempted to obtain an empirical relation between the slip velocity and the stress drop. Although this could not be done without ambiguity for the data sets analysed, it appeared that with more detailed study, it should be possible to obtain an empirical relation for a certain area. Once this has been done, the process can be reversed, in other words, from the stress drop (and source area), the rise time can be calculated, which is required as an input for VMAP.

VMAP proved to be a convenient and effective way to evaluate strong ground motion from hazardous structures. This is done by simulating an event at a position, and calculating the ground motion (peak particle velocities) in the surrounding area.

In the present study, a method is proposed method to estimate strong ground motion from possible large events. The method was demonstrated in two ways. Firstly, the magnitude of ground motion was estimated at distances away from a vertical source. If a worst case event is assumed, the simulation can be used to calculate the resulting ground velocity as a function of the distance from the source, and the model can thus be used to assist in stope support design. In the second case, an event was simulated on a hazardous fault. The ground velocity was visualised in 3D, and this provided useful information regarding possible damage throughout the volume modelled. The above was supplemented with 3D contours of sigma 1 stress (from an elastic MAP3D model), which pointed out highly stressed areas.

## 7. Case studies

### 7.1. Aspects of the seismic response to shaft pillar mining - case studies in the Welkom Gold Field

#### 7.1.1. Introduction

Several shaft pillars have lately been mined out in the Welkom gold field and a number still have to be mined. In this contribution, some of the experience gained by the seismic monitoring of the rockmass response is described. Three cases, all from Western Holdings Mine, are considered, namely shafts number 6, 2 and 4. The mining is complete in the first two cases and is more than half way in the case of the last.

The seismic response is described in terms of seismic time histories and statistical hazard parameters. In the time history analyses, cumulative apparent volume ( $EV_a$ ) and median energy index ( $E$ ) are used to compare the stress and strain histories of the pillars and to establish benchmark cases for future reference to shaft pillar mining under these conditions. These and other seismic parameters are defined in Appendix 1.

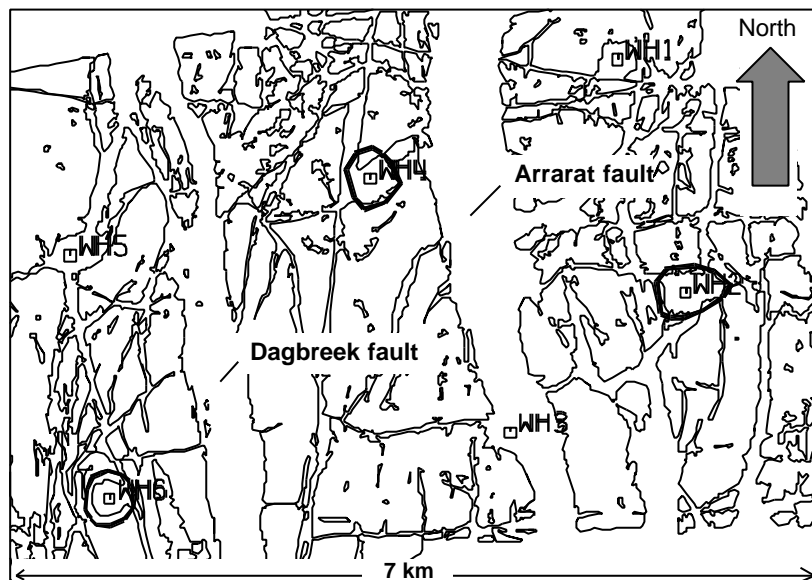


**Figure 7.1 Mining faces of a largely mined out part of Western Holdings Mine depict two major fault loss areas and six shaft pillars. Data for this study were selected from the three polygons shown around Shafts No. 2, 4 and 6.**

#### 7.1.2. Mining environment

The Basal Reef is the ore body in each case and the depth, reef dip and structural complexities are broadly similar. Figure 7.1 is a plan of a part of the mine, showing the shaft positions relative to regional mining faces, while more detail is given in Figures 7.8-7.10. Table 7.1 summarises some of the characteristic features of the shafts.



**Table 7.1 Some characteristics of the pillars of Shafts Number. 2, 4 and 6, Western Holdings Mine**

Shaft	Avg. depth [m]	Dip	Appr. area [m <sup>2</sup> ]	Structural features
6#	1300	15E	0.7E5	Fault bound in the east, minor fault, steeply dipping to the north, cuts through centre.
2#	950	25E	1.3E5	Major fault/dyke/sill bound on all sides, NS faulting through centre, structurally most complex.
4#	1430	16E	1.6E5	Pillar 'cut loose' from major dyke at western boundary, NE fault/dyke/horst zone cuts through centre.

The shafts were mined 'conventionally', i.e. from the inside out. The design was largely based on stress modelling. Backfill was used in part. More details of the shaft pillar mining is given in a compilation by *Lategan (1996)*.

### 7.1.3. Seismic time histories

In this section, the seismic histories of the shafts are described in terms of seismic event parameters cumulative apparent volume ( $E V_a$ ), apparent stress ( $F_A$ ) and energy index ( $EI$ ). The stress/strain history of Number. 6 Shaft, as inferred from seismicity, has been described as similar to that of a rock sample in a laboratory press (see *van Aswegen et al, 1997, p.226*): an initial period of 'strain hardening', characterised by relatively low seismic strain rate (as indicated by the slope of the  $E V_a$  curve) and high moving median energy index followed by 'softening', when the seismic strain rate increased significantly and the  $EI$  dropped. The shaft area reached a peak stress level around May 1993 before it dropped relatively sharply. The slope of the  $E V_a$  increased after May '93 and remained high till the end 1994 when mining was completed. Most of the largest seismic events occurred after May 1993.

For the purpose of the time history study, seismic data (and production data in the case of Number 2 and 4 Shafts) were selected from within the boundaries of the shaft pillars only, i.e. seismic events spatially associated with major structures outside the pillars were excluded (see Figures 7.8 – 7.10).

Time histories of  $E V_a$  and moving median  $EI$  for the three shafts considered here are shown in Figures 7.2, 7.3 and 7.4. The time scale for all these plots are the same apart for a two year time shift between Number 6 Shaft (1/1/90 - 28/5/95) compared to Number 2 and 4 (1/1/92 - 28/5/97).

Larger events are shown as vertical lines on the time history diagrams.

Note that the two shafts at which mining is complete (Number 6 and 2, Figures 7.2 and 7.3) show very similar time history patterns, i.e. the 'stress-strain' history described for Number 6 Shaft (see above) was repeated at Number 2 Shaft. Note also that, in comparison with the two mined out shafts, Number 4 Shaft is already in the high strain rate stage and has apparently passed its peak level of  $EI$ .

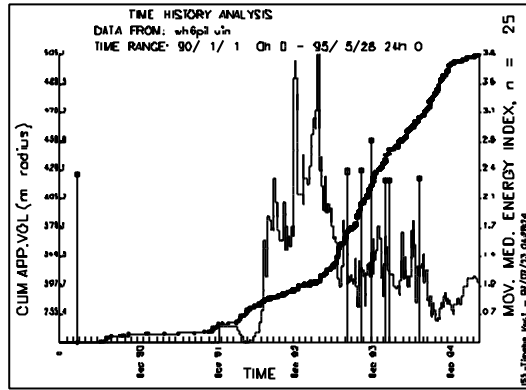


**Figure 7.2 Time history of  $GV_a$  and moving median  $EI$  for the period 1/1/90 to 28/5/95, WH6#.**

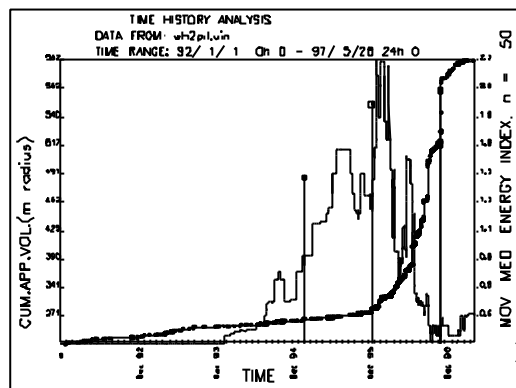


**Figure 7.3 Time history of  $GV_a$  and moving median  $EI$  for the period 1/1/92 to 28/5/97, WH2#.**

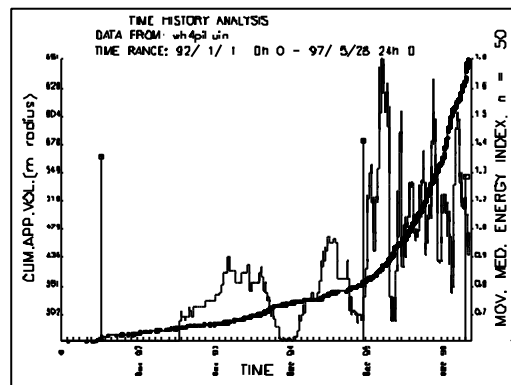


**Figure 7.4 Time history of  $GV_a$  and moving median  $EI$  for the period 1/1/92 to 28/5/97, WH4#.**

In Figures 7.2 to 7.4 the vertical scales are not fixed. The  $EI$  is based on local empirical  $E-M$  relations and cannot be compared between shafts.

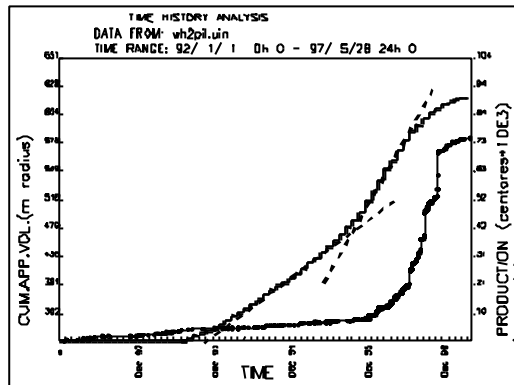


**Figure 7.5 Time history of cumulative production and cum.  $V_a$  for the No. 2 shaft pillar. The broken lines accentuate production rates for particular periods.**

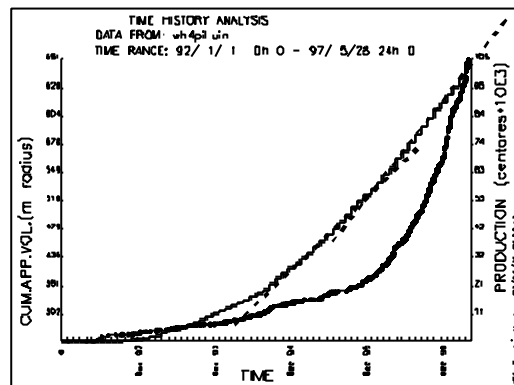


**Figure 7.6 Time history of cum.  $V_a$  and cumulative monthly production for WH4# during the period 1/1/92 to 28/5/97.**

The seismic strain rate should generally follow production rate. Figures 7.5 and 7.6 compare production rate and  $E V_a$  of Number 2 and 4 Shafts. In this case the vertical scales are held constant to show that, at Number 4 Shaft, a larger area has already been mined compared to the total at Number 2 Shaft, explaining the greater  $E V_a$  value. Note how the  $E V_a$  slope correlates with that of production at both shafts.

To further compare the seismicity at Numbers 2 and 4 shafts, the 'stress level' as indicated by the Apparent Stress Level for moment= $1E10$  N.m.  $\bar{s}_A < M^{10} >$  - see Appendix 1 where this term is introduced) was calculated for different time periods:

1. up to the end of 1993, both shafts, (for the background level prior to significant shaft pillar mining)
2. 1/12/95 - 31/5/95 for 2#, 1/07/96 - end for 4# to coincide with the periods of peak production (compare Figures 7.5 and 7.6)
3. 1/1/97 - end, both shafts, to compare the final stage of 2# with the late phase of 4#

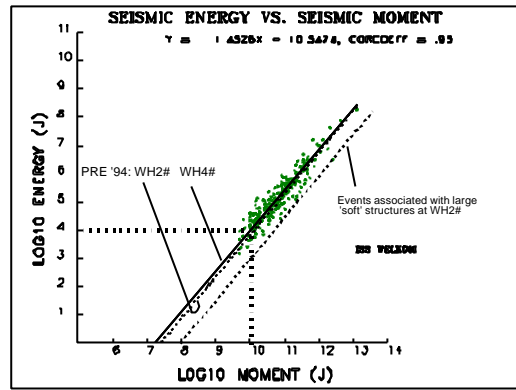


**Figure 7.7 Example of a  $\log(E)$  vs.  $\log(m)$  plot used to establish an empirical relation for the purpose of calculating Energy Index (EI) and Apparent Stress Level ( $\bar{s}_A < M^{10} >$ ). The broken line connecting a given  $\log(m)$  value to an appropriate  $\log(E)$  value through the empirical fit, demonstrates the latter concept.**

The E-M empirical fit for the first period at Number 4 Shaft is shown in Figure 7.7. The results of the calculations are given in Table 7.2. Note that, prior to the main pillar mining stages, this seismic stress indicator shows a higher value for 4# than for 2#. However, during the high production rate stage, the Apparent Stress Level at 2# is double that at 4#. During the dying stage of 2# the value has dropped some, but it still remained higher than at 4#. It was also noted that the seismic event size and apparent stress distribution at Number 2 Shaft was distinctly skew. The main population of seismic events define the empirical E-M relations on which the first row of Table 7.2 is based. A second population is characterised by low E/M values and a  $\bar{s}_A < M^{10} >$  value of 20 KPa (see Figure 7.7).

**Table 7.2 Apparent Stress Level, i.e. average apparent stress for  $\text{Log}(M)=10$  ( $\bar{s}_A < M^{10} >$ ) for different stages of mining at WH Numbers 2 and 4 Shafts. The units are KPa.**

	Pre pillar mining	During peak production	Final stage(2#)/ late stage(4#)
2#	21	40	35
4#	29	20	20

NOTE: Comparisons of  $\bar{s}_A < M^{10} >$  is less reliable along the rows than the columns since the seismic monitoring system has improved significantly through time - the way source parameters (like E and M) are calculated changed as a result.

#### 7.1.4. Seismic hazard

Seismic hazard is defined as the probability that a seismic event of given magnitude or greater will occur within a given time (seismic risk being the product of hazard and liability). The classical way of describing the magnitude distribution of seismic events and hence estimating seismic hazard is through the so-called Gutenberg-Richter analysis. The principle is simply that the sizes (magnitudes) of seismic events follow a fractal distribution. The number of events decrease exponentially with size. Describing this phenomenon for a given area is done through a cumulative frequency versus magnitude plot, such as shown in Figures 7.7 onwards. The Gutenberg-Richter relation has the form

$$\log En = a - bm,$$

where  $n$  is the number of events with magnitude  $m$  and greater. The negative sign is used in the relation so that the coefficient  $b$  is quoted as a positive value, i.e. the  $b$ -value. If the event

frequency increases, the value of  $a$  increases, if the proportion of larger relative to the smaller events increases, the  $b$ -value decreases. A  $b$ -value of 1.0 is considered 'normal'. Other parameters of concern are  $M_{max}$  (maximum magnitude) and  $M_{min}$  (minimum magnitude for which the data base is complete). Having established these coefficients for a given area/time, the seismic hazard can be calculated and presented in the form of probability and recurrence time tables. The methods used here are as proposed in Mendecki et al, 1995.

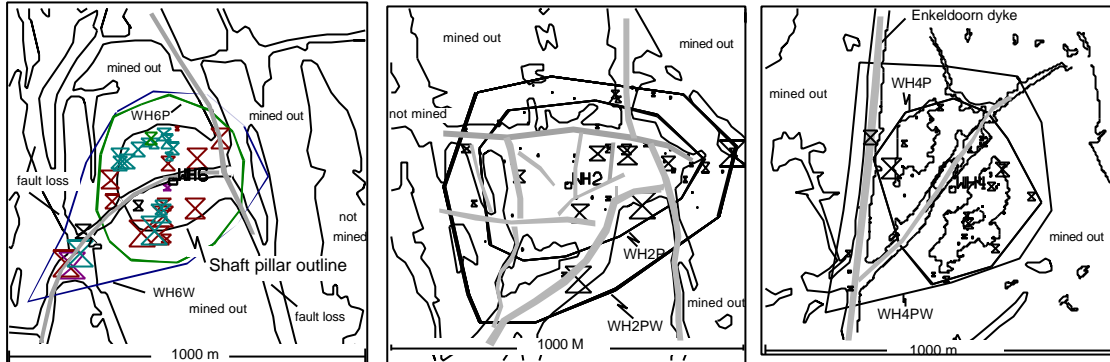


**Figure 7.8 (left) Important geological features, event selection polygons and some of the larger events recorded at WH6#. The mining faces are as they were prior to mining in the pillar.**

**Figure 7.9 (middle) Important geological features (schematic), event selection polygons and some of the larger events recorded at WH2#. The mining faces are as they were prior to mining the pillar.**

**Figure 7.10 (right) Important geological features, event selection polygons and some of the larger events recorded at WH4#. The mining faces are as they were at the approx. 60% extraction stage.**

Evidently, part of the rockmass response to pillar mining is the de-stabilisation of large geological structures immediately adjacent to the pillars. To capture this effect in the statistical analysis of the data, slightly larger polygons were chosen for event selection compared to those for the time history analyses. Figures 7.8, 7.9 and 7.10 are simplified plans of the shaft pillar areas, showing the most important geological features, the event selection polygons and some of the larger events which were recorded. For WH2# and WH4#, two time periods were chosen for inclusion here. The first period in each case represents the seismic pre-history in the immediate surrounds of the pillar as well as some of the preparatory mining of the pillars, in each case leading to the first local magnitude 2 event. The purpose was to see whether there was information in these statistics pertaining to the subsequent seismic response to pillar mining. In the case of WH2# the end date for this period was chosen to be end February 1995 while for WH4# the end of December 1995 was used - i.e. the times at which the maximum *change* in strain rate, as depicted by the slope of  $E V_a$  curve occurred. The second time period in each case was 1/11/96 - end June 1997 to capture the tail end of the WH2# production and to ensure compatibility of data in the light of recent changes in source parameter calculation methods. The results of the statistical analyses of the different data sets are given in Figures 7.11 – 7.15 and in Table 7.3. From these, some observations can be made. The size distributions of events at WH6# and WH4# are close to 'normal', with a  $b$ -value close to 1.0.

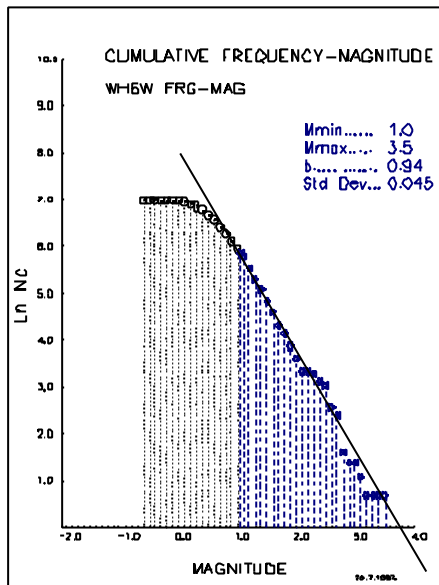


Figure 7.11 (left) Frequency-magnitude plot for seismic data from WH6 for the period Jan '90 – Mar. '95.

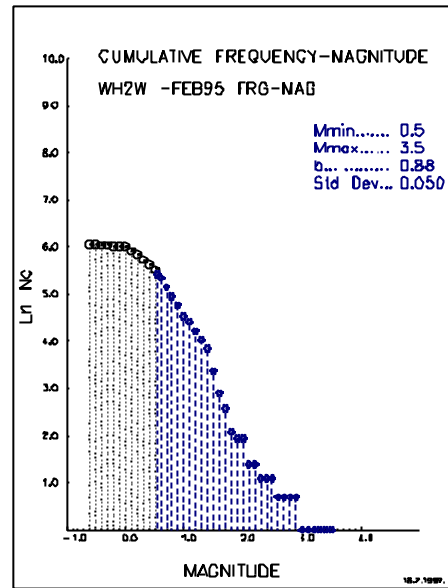


Figure 7.12 (right) Cumulative frequency-magnitude plot for WH2# for the period 1/1/90 till 28/2/95.

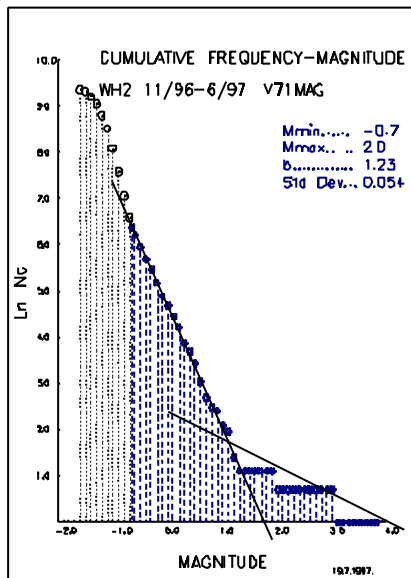


Figure 7.13 (left) Cumulative frequency-magnitude plot for WH2# for the period 1/11/96 – 30/6/97.

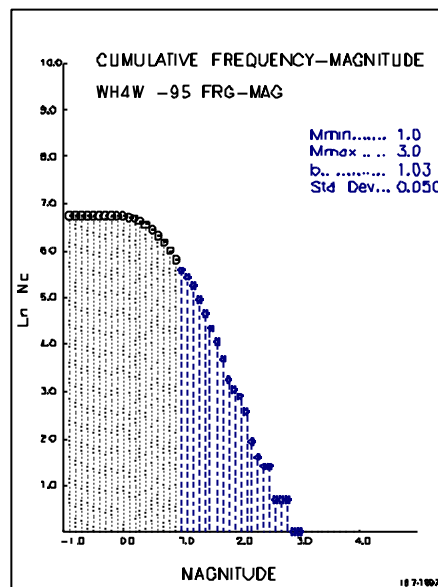
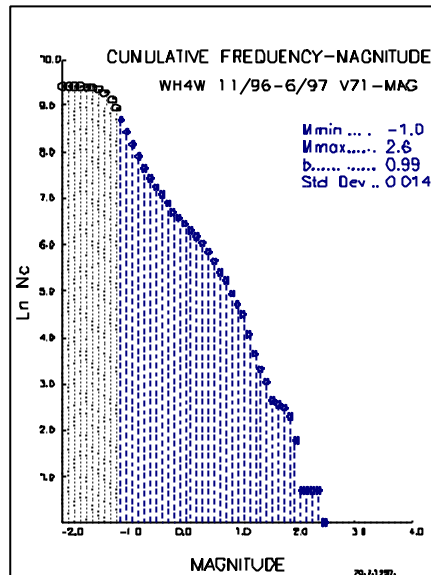


Figure 7.14 (right) Cumulative frequency-magnitude plot for WH4# for the period 1/1/90 – 31/12/95.



**Figure 7.15 Cumulative frequency-magnitude plot for WH4# for the period 1/11/96 – 30/6/97.**

**Table 7.3: b-values, recurrence times ( $R_t$ , in months) and probability of occurrence (within 1 month) for mag.m or larger events for stages: before main pillar mining stage (-B), late/final stage (-F) and total period (-T). F1 and F2 refer to the two populations of events at WH2#.**

	b	$R_t$ m2	P.m2	$R_t$ m3	P.m3
WH6-T	0.94	1.90	.41	21.0	.05
WH2-B	0.88	5.12	.18	58.5	.02
WH2-F2	0.44	2.89	.32	12.04	.09
WH2-F1	1.86	>99	.01	>99	0.0
WH4-B	1.03	3.14	.27	>99	.001
WH4-F	0.99	1.78	.43	>99	0.0

In the case of WH4, this remained the case after mining a large part of the shaft pillar (> 50%). In the case of WH2#, the b-value was initially low, but the response to the pillar extraction was the yielding of two populations of events, the larger events displaying a very low b-value, causing a concave downward bend of the cum. frequency-magnitude plot. A comparison of Figure 7.12 with Figure 7.13 shows that a tendency for the cum. frequency-magnitude plot to flatten with increase in magnitude, became accentuated during and after shaft pillar extraction.

### 7.1.5. Discussion and conclusions

The similarities in the stress-strain patterns as indicated by  $E V_A$  and median  $EI$ , namely an initial stage of increase in stress level and then a drop associated with increased strain rate, shows that this phenomenon, first described for WH6#, is generally to be expected during shaft pillar extraction. It is not surprising - the seismic source parameters merely reflect the expected variations in stress and strain rate associated with a rapidly decreasing pillar size. It does, however, provide a tool to monitor the timing of these variations.

The differences in stress level between WH2# and WH4# at different stages, as indicated by

$\bar{s}_A < M^{10} >$ , requires some consideration. Since WH2# is shallower, the initial lower value here is expected. The subsequent higher stress level is unexpected. It may result from a higher production rate at 2# - compare the slopes of the cumulative production curves in Figures 7.5 and 7.6.

The skew size distribution of seismic events at 2# could be explained by the response of geological structures to production. Larger events are generally associated with major faults or dykes while the smaller events are the direct response of the rockmass in general to the stress induced by stoping. Bi-modal event size distribution is not unknown in mines (e.g. *Kjiko et al, 1987*) and the explanations are generally the same. The relatively low E/M ratios of the larger events at WH2# (see Fig. 7) indicates a 'soft' nature for the larger structures. It suggests that it is the large faults, with known weak fault rock filling, that slip to yield the larger events rather than some of the stiffer dykes. Rockburst damage was associated with dykes (as observed after the largest event in Dec. 1996), but the low  $F_A$  of the events which caused the damage suggested relatively 'slow' tremors. The dyke bursting is explained as a local response to the dynamic loading caused by the large tremor.

At WH4#, the most prominent geological structure is the strong (compared to the surrounding quartzites) 30m wide Enkeldoorn dyke. In contrast, the most prominent geological structure at WH2# is a weak, large displacement fault. This probably exemplifies the general difference in geological structure between the two shafts as reflected at an early stage by the lower b-slope for the larger events prior to main pillar extraction at WH2# - compare Figs. 12 and 14. The potential seismic hazard posed by the Enkeldoorn dyke, a structure known as seismically active and initially forming the western boundary of the No. 4 shaft pillar, was largely neutralised by first mining a wide strip between it and the rest of the shaft pillar. This procedure does not eliminate further stress induced seismic events along the structure, but spatially separates this particular hazard from active mine workings (see Fig. 10)

Conclusions are summarised as follows:

Time history analysis of  $E V_a$  and moving median EI are useful to track the rockmass stress-strain behaviour during pillar mining.

Depending on the local geology and mining layouts, increased production rate can increase seismic risk by i) causing a higher stress level in the immediate surrounds of the ore body and ii) increase the frequency of larger events.

Statistical seismic hazard analysis (Gutenberg-Richter) at an early stage can indicate the probable nature of the rockmass response during pillar extraction.

## 7.2. System stiffness and source parameters, $E$ - $M$ relation

The ratio between the measured seismic energy of a given event and the average seismic energy,  $E$ , for the measured seismic moment, as given by the  $E$ - $M$  relation:  $\log E = c + d \log M$ , is the energy index (*van Aswegen and Butler, 1993*). To calculate EI for an event in a given area, one therefore needs to first find the appropriate E-M relation. This is regularly established by line fitting procedures on most rockburst prone gold mines in South Africa and several mines internationally.

### 7.2.1. Variable slopes in E-M relation: Observations

With the increasing sensitivity of seismic monitoring systems, the range of magnitudes of seismic events recorded increased and many mine wide seismic systems now record seismic events down to local magnitude -1 or (moment = 1 E7 Nm). It is frequently noticed that the slope  $d$  is not constant over the wider moment range. Specifically the slope tends to be steep below  $\log M 9$  and less steep for larger events. Figure 7.17 shows, for example, the E-M plot for



events recorded around the No. 5 Shaft pillar of Western Holdings mine in Welkom for the period 971031 to 971128 (the time period was limited here to minimise the electronic picture file size). Only a small portion of the pillar was mined during 1997 and generally only small events occurred. Some larger events were apparently the result of reactivation of faults and dykes in the mined out immediate surrounds, having been stress loaded by the regional mining of the past. As a result a distinct kink in the E-M relation is evident around  $\log M = 9$ .

Figure 7.17 is an E-M plot for the events greater than  $\log M 9.0$  during most of 1997, showing the results of an orthogonal fit through this data. Also shown are the empirical fits for two subsets of those events smaller than  $\log M 9.0$ , namely those with a higher than average ratio Energy\_S/Energy\_P and those with a lower than average ratio. The first point to note is that the larger events empirically define an E-M relation with a significantly lower slope than that shown by the smaller events. Of the two subsets of smaller events, those with a higher than average E\_S/E\_P ratio yield an E-M relation with a slightly steeper slope. Over the size range of interest here, these events radiate more energy for given moment than those events with a lower E\_S/E\_P ratio.

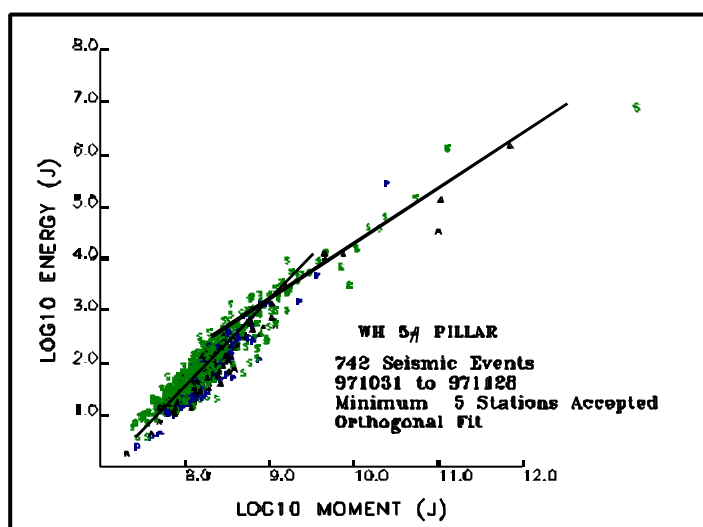


Figure 7.16

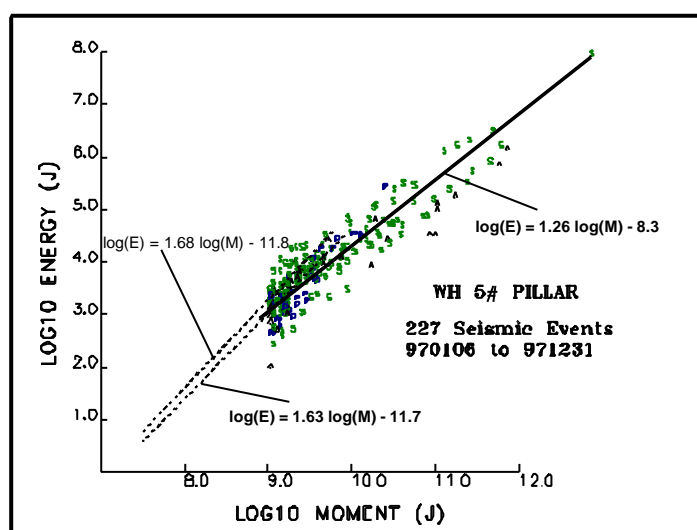
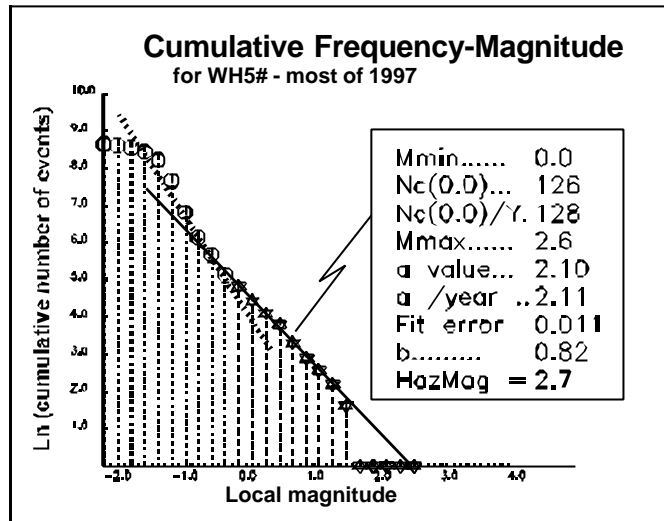


Figure 7.17



**Figure 7.18**

Figure 7.18 shows the size distribution and seismic hazard parameters for WH5# pillar area. The kink in the slope coincides with the change in slope in the  $E-M$  relation at Figure 7.17. While such bimodal size distribution of seismic events in mining has been observed elsewhere (e.g. *Kijko et al, 1987*) it has not been linked to the nature of seismic radiation and stress-strain relations of the system.

Since the physical significance of the change in  $E-M$  relation is of interest here, it needs to be established whether the phenomenon is not an artefact of the seismic monitoring instrumentation and data processing procedures. The behaviour of the 4.5Hz geophones generally used in the South African gold mining industry could be suspect at the high frequencies associated with the small events. Also, if the geophones are not grouted in properly, the boats within which they are mounted may resonate at high frequencies yielding artificial responses. A third problem could arise if the frequency dependence of  $Q$  is not taken into account during seismological processing.

In order to test the validity of variation in slope for a given data set, events from a small pillar which was well covered by a subnetwork of seismometers are examined. Figure 7.19 shows the plan view distribution of events within the pillar area.

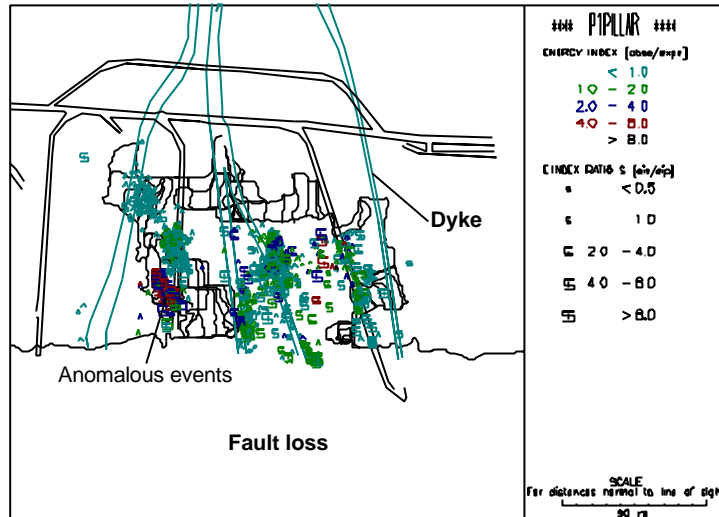


**Figure 7.19**

A particular cluster of events are anomalous both in terms of where they occur (well behind the stope face and relatively deep into the footwall of the mined out ore body) and in terms of source parameters (the E\_S/E\_P ratios of these events are generally higher than those in the rest of the pillar area). The local interpretation is that a strong (stiff) dyke structure in the footwall of the stope was activated by the general stress disturbance caused by the mining. Exactly the same seismometers recorded all events in the pillar and the anomalous events were processed in exactly the same way as the rest. It appears therefore that these the two populations of events differ in general source characteristics because of a difference in source mechanism, reflecting a difference in rock strength and or shear stress conditions in the source regions. The difference between the two populations show up clearly on an E-M plot (Figure 7.20). The anomalous events define a steeper E-M relation, with a limited magnitude range.

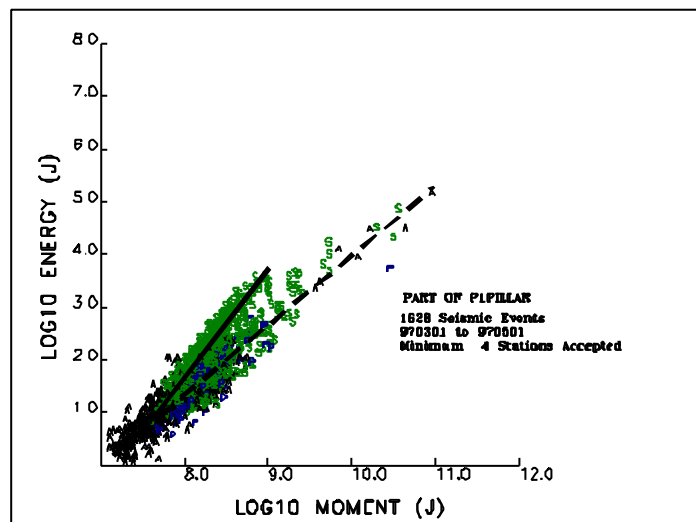


**Figure 7.20**

Where seismic events from normal stoping operations are mixed with events associated with the nearby development of tunnels, it is found the tunnel events define a steep E-M relation with a limited magnitude range while those events associated with the large stoped out area define

an E-M relation with a lower slope and a larger magnitude range. The phenomenon was again confirmed when output from the Japanese Kyoto University network at Western Deep Levels was tested. This network was accelerometer based, eliminating the possible artefacts that could be introduced by the 4.5Hz geophones common to most mines.

### 7.2.2. Variable slopes in E-M relations: Interpretation

The change in slope of the E-M relation indicates that the majority of the smaller events in the gold mines do represent a different population of seismic events than that represented by the larger events. Since seismic moment generally represents the amount of co-seismic strain at the source while the ratio E/M indicates the stress level at the source, the slope of the E-M relation could be compared to the slope of a stress/strain curve - the steeper slope would then represent a stiffer environment.

The larger events generally represent the failure of joints or other discontinuities under the influence of stoping induced stress changes. It is envisaged that the small events mostly represent fracturing in the volume of extreme stress concentration ahead of the stope faces. Although the events are small, they are characterised by relatively high E/M ratios. Where micro-seismic events associated with tunnel development and ledging are mixed with more regular types of events, the results of E-M analysis can be extreme. The 'system' in the immediate surrounds of small openings are more stiff than around large stopes.

The different environments should cause differences in seismic event mechanisms. The ratio of the energy radiated by the S-wave to that radiated by the P-wave is indicative of seismic source mechanism. The fundamental mechanism of a seismic event is that of simple shear. This is because the boundary conditions generally do not allow volume change. Simple shear (i.e. plane strain) does not involve volume change. The only situation where significant deviation from this mechanism is possible, is where at least one component of stress tend towards being tensile, i.e. where an opening is involved. Events close to an opening could therefore be expected to show lower than average E<sub>S</sub>/E<sub>P</sub> ratios, i.e. the spatial freedom would allow a 'pop' mechanism as opposed to the more common slip mechanism. Since rock is weak in tension, the rock fails before the stress level becomes very high. The 'pop' events can therefore be expected to exhibit low E/M ratios (see *van Aswegen and Meijer, 1993*). As an aside, we may therefor note that large events cannot have explosive mechanisms.

In conclusion the *d*-value defining the slope of the logE vs logM straight line fit, called the E-M relation, tends to correlate with the system stiffness - the stiffer the system the steeper the line and the higher the *d*-values. The E-M relation for the stiff system does not extend far into the large moment domain since it does not produce large events until its stiffness is degraded and the *d*-value drops. For a given slope an increase in the *c*-value of the E-M relation reflects an increase in stress - the apparent stress of a typical event with  $M = 1\text{Nm}$ , or  $m = -6$ , would be  $s_A(M = 1) = \text{rigidity} * 10^c$ .

### 7.3. Back analysis of a magnitude 4 event

In early May 1996 a magnitude 4 event occurred where a Carbon Leader Reef longwall breasted onto a fault zone at Western Deep Levels (Figure 7.21). No injuries occurred, but extensive damage was recorded in the stope. A first back analysis of the area was described in Appendix 8 of the year end report, 1997. Here the data is re-analysed after some re-processing of the seismic source parameters, the implementation of an improved methodology to calculate particular seismicity parameters (specifically apparent stress level is calculated with a fixed *d* value (see Glossary) and a different choice of the size of the moving time window for back analysis.

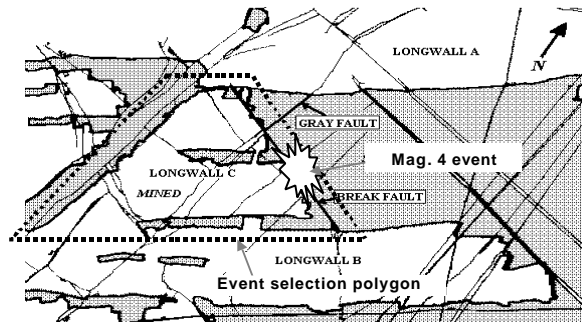


**Figure 7.21** The mining situation for the back analysis described in the text. Also shown is the polygon for event selection used for the analysis.

The back analysis the evaluation the Gutenberg-Richter  $a$  and  $b$  values for a four month moving time window starting in January 1994 up to the end of May 1996. The time window was stepped forward in one-month steps. For the calculation of the  $a$  and  $b$  values a simple procedure was followed: The value of  $M_{min}$  (minimum magnitude) was found through visual inspection of the cumulative frequency-magnitude histogram and  $b$  was then found through robust line fitting above  $M_{min}$  (Figure 7.23). For each of the selected time-subsets,  $d$  and  $c$  values of the E-M relation (Figure 7.24), the apparent stiffness and apparent stress level (for moment=10E10) were also calculated. The variation of  $b$  and  $d$  over time is shown in Figure 7.24. A reasonable correlation between the  $b$ -value and the  $d$ -slope is evident. This is consistent with the conclusion (van Aswegen and Mendecki, 1998, Mendecki et al., 1999) that stiffer systems (higher  $d$ -slope) limit both the frequency and the magnitude of intermediate and large events.

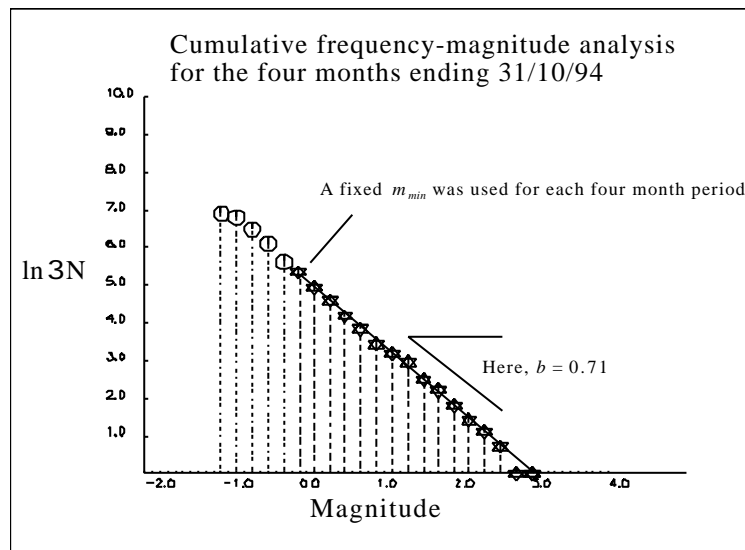


**Figure 7.22** An example Gutenberg-Richter plot for one of the 27 four month time periods (forward stepping by one month) analysed.

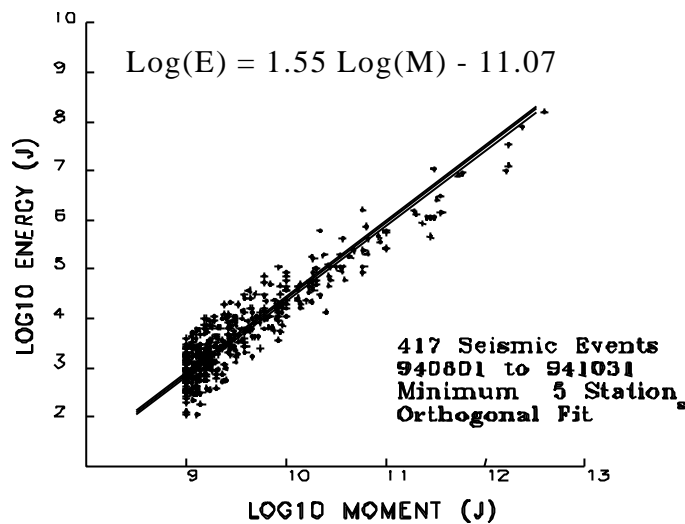


**Figure 7.23** An E-M plot for the same dataset reflected in Figure 3, except that all events < log(M)9.0 are filtered out – this was done for all the datasets analysed

The variation over time of apparent stress level and apparent stiffness is given in Figure 7.25. It is interesting to note that both these parameters show a steady decline over the last six months prior to the large event. The interpretation is that the system was softening due to progressive mining and resultant increase in mining span. The likelihood of a large event would be increased under such circumstances. Note that such an analysis is a far cry from temporal prediction. At best one could conclude that the potential for unstable deformation is increasing. It does show, in this case, that the system was losing stability.

This back analysis shows how traditional seismic hazard evaluation, combined with continuous evaluation of the E-M parameters, can be used to qualitatively evaluate the rockburst hazard.

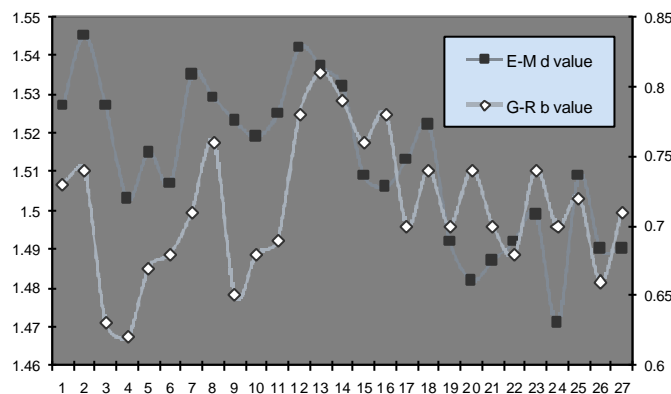


**Figure 7.24** The variation of the Gutenberg-Richter b value and the E-M d value over the 27 months prior to the large event. The b value varies between 0.62 and 0.84 while the d value varies between 1.46 and 1.55.

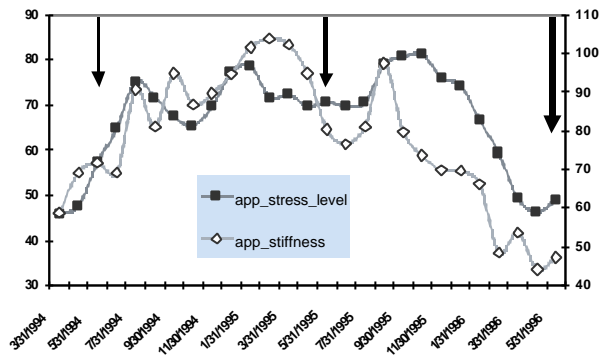


**Figure 7.25 The variation of apparent stress level (30 to 90 KPa) and apparent stiffness (40 to 110 MPa) for the 27 months prior to the large event. The arrows indicate the occurrence of events larger than  $\log(E)10$ , the last arrow reflecting the occurrence of the main event of interest here.**

## 7.4. The Seismic Response to Production

If a volume of rock,  $V_M$  is mined and if the altered stress and strain field can readjust to an equilibrium state through seismic deformation only, the sum of seismic moments ( $\Sigma M$ ) released within a given period of time would be proportional to the excavation closure, and in the long term

$$\Sigma M = G V_M \text{ (McGarr, 1976).}$$

In terms of potential seismic energy, the same concept can be re-stated as follows: The amount of strain energy stored when mining elastic rock is directly proportional to the volume of elastic convergence  $V_E$ . Because the rock is not linearly elastic, it is useful to add a proportionality constant to the above equation

$$\Sigma M = \gamma G V_M$$

*Milev et al. (1997)* found that  $\gamma$  varies between .3 and 1.0. The variation would likely correlate with variation in geotechnical area. The volume of elastic convergence can be modelled and was, for example, used by *van der Heever and O'Connor (1994)* for the planning of pillar mining. By monitoring the cumulative seismic moment and comparing it with numerical model prediction they could evaluate the potential of the system to yield a large event.

Thus, knowing  $\gamma$  would allow the prediction of the amount of seismic moment expected to be released for a given volume mined. It does not, however, provide information about the nature of the seismicity, e.g. few big events vs. many small ones. The principle, however, allows the option to continuously compare production rate and seismic strain rate. A significant deviation from a constant ratio could indicate an increase in seismic hazard, either because the seismic response is lagging behind (elastic strain energy could be building up) or the seismic response exceeds expectations (the system is unstable). In the first case (seismic response lower than expected) parameters like apparent stiffness and energy index could be used to judge whether the rockmass is indeed storing energy or whether it is simply too weak to yield significant seismic events.

For a given mine layout a particular step in elastic convergence would be directly proportional to the volume mined in that step. By normalising the seismic response to mining with the volume mined, we get a measure of the relation between the stored and the released energy. A particularly useful seismicity parameter which measures seismic strain is  $\Sigma V_A [m^3]$ . By dividing  $\Sigma V_A$  by  $\Sigma V_M$  (volume mined) we get a dimensionless number, or index, which is easy to routinely

calculate and can be used to monitor the seismic response to mining. We can refer to this ratio as the seismic response to mining index (*SRP*), i.e.

$$SRP = \Sigma V_A / \Sigma V_M$$

A weighted form of this index (locally known as REP index, *Amidzic and Murphy, 1997; Amidzic et al., 1999*) is defined as

$$SRP = Ne(\Sigma V_A / \Sigma V_M),$$

Where *Ne* is the number of events above a given cut-off value, typically magn. 1.0.

Over a given time a constant value of *SRP* would indicate a consistent release of energy, in keeping with the volume of elastic closure. A decrease from a constant value will indicate that more energy is stored than normal (generally undesirable). An increase would indicate that the system is starting to release energy at a faster rate than normal and that the system could become unstable. The following are example situations, which could cause deviations from a regular trend:

- the approach of mining to a geological discontinuity
- a change to an unsuitable mining configuration
- a change in the effectiveness of regional support (backfill, stabilising pillars)
- unknown residual stress ('tectonic')

In general, one would expect a change in the general trend of *SRP* to reflect a change in system stiffness. In *Amidzic et al (1999)* it is shown how, in one case where mining approach the last unlocked part of a fault zone, a high level of production was associated with an even higher level of seismicity, induced by fault zone proximity, resulting in sharply rising values of *SRP* prior to a magnitude 4.0 event. Subsequent changes in layout control and an improved support system (high percentage backfill carried very close to the advancing face) yielded equivalent production but much lower and constant *SRP*.



## 8. References

- Amidzic D. and Murphy S.K. 1997.** Evaluation and control of the seismic risk at Western Deep Levels Ltd.- East Mine. *SARES'97, 1<sup>st</sup> Southern African Rock Engineering Symposium*. Johannesburg, South Africa.
- Amidzic, D., Murphy, S.K. and van Aswegen G. 1999.** Case study of a large seismic event at a South African gold mine. *To be presented at ISRM 9<sup>th</sup> International Congress on Rock Mechanics*. Paris, France, September 1999.
- Bazant, Z.P. and Cedolin, L. 1991.** *Stability of Structures*, The Oxford Engineering Science Series, Oxford University Press, 1991, pg. 984.
- Bernard, P. and Madariaga, R. 1984.** A new asymptotic method for the modelling of near-field accelerograms, *Bulletin of the Seismological Society of America*, 74, pp.539-557.
- Birch, M.T.G. 1996.** Implications of fault populations studies for future mine planning at Freddie's Mine No. 1 and 4 shafts. *AAC 9th Annual Gold Division Geological Conference Proceedings*.
- Brown, F. 1995.** The application of power law theory to mine production planning. *AAC 8th Annual Gold Division Geological Conference Proceedings*.
- Carr, J.R. 1997.** Statistical self-affinity, fractal dimension, and geologic interpretation. *Engineering Geology*, vol.48, no.3-4, p. 269 - 298.
- De Beer, W. and Mendecki, A. J. 1998.** Seismology for rockburst prediction. *SIMRAC Mid-year Report, GAP409*. Pretoria: Department of Minerals and Energy.
- Dieterich, J.H. 1980.** Experimental and model study of fault constitutive properties. *Solid Earth Geophysics and Geotechnology. AMD*, vol. 42. Nemat Nasser (ed.). American Society of Mechanical Engineers, 1980, pp. 21-29.
- Dzhafarov, A. H. 1998.** Non-linear Seismology. *SIMRAC Final report, GAP 211*. Pretoria: Department of Minerals and Energy.
- Fraser, A. M. and Swinney, H. L. 1998.** Independent coordinates for strange attractors from mutual information. *Physical Review, A*, 33, 1134.
- Grossberger, P. Hegger, R., Kantz, H., Schaffrath, C. and Schreiber, T. 1993.** On noise reduction methods for chaotic data. *Chaos*, 3, 127.
- Hobbs, B.E., Muhlhaus, H.-B, and Ord, A. 1990.** Instability, softening and localisation of deformation. From Knipe, R.J. & Rutter, E.H. (eds), 1990. *Deformation Mechanisms, Rheology and Tectonics*, Geological Society Special Publication No. 54, pp. 143-165.
- Joyner W. B. and Spudich, P. 1994.** Including near-field terms in the isochron Integration method for the application to finite fault or Kirchoff boundary integral problems. *Bulletin of the Seismological Society of America*, 84, 4, 1260-1265.
- Kanamori, H. and Boschi, E. 1983.** *Earthquakes: Observation, theory and interpretation. Proceedings of the International School of Physics "Enrico Fermi"*. Varenna on Lake Como, Villa Monastero, 29<sup>th</sup> June – 9<sup>th</sup> July 1982. 608 pp.
- Kostov B. V. and Das S. 1975.** *Principles of earthquake source mechanics*. Cambridge University Press, 286pp.

**Kennel, M. B. and Abarbanel, H. D. I. 1995.** False neighbours and false strands: a reliable minimum embedding dimension algorithm. *INLS preprint*. University of California, San Diego.

**Kjiko, A., Drzezla, B. & Stankiewicz, T. 1987.** Bimodal character of the distribution of extreme seismic events in Polish mines. *Acta Geophys. Vol. 35*, 159-168.

**Lachenicht, R.J. in prep.** An analysis of the asperity model under viscoplastic displacement loading and its integration with quantitative seismology. MSc Dissertation, University of the Witwatersrand, Johannesburg.

**Lategan, J.C. 1996.** Final minutes of shaft pillar extraction review held at No. 1 Shaft canteen on 14 June 1996. Internal report, Western Holdings Mine, ref. WH226-96

**Lemaitre, J. and Chaboche, J.-L. 1994.** Mechanics of solid materials, Cambridge University Press, 1994, pg. 556.

**McGarr, A. 1976.** Seismic moments and volume change. *J. Geoph. Res.* 81, 1487-1494.

**McGarr, A. 1991.** Observations constraining near-source ground motion estimated from locally recorded seismograms. *Journal of Geophysical Research.* Vol. 96, No. B10, pp. 16 495-16508.

**McGarr, A. 1993.** Keynote address: Factors influencing the strong ground motion from mining induced tremors. (*In: Young (Ed). Rockbursts and seismicity in mines 93.* Balkema, Rotterdam.)

**Mendecki, A.J. (ed.) 1997.** Seismic monitoring in mines. London: Chapman and Hall, 262 pp.

**Mendecki, A. J. 1997.** Quantitative seismology and rockmass stability. (*In: Mendecki (Ed). Seismic monitoring in mines.* London: Chapman and Hall, p.178-219.)

**Mendecki, A. J. et al. 1995.** Seismology for Rockburst Prevention, Control and Prediction. *SIMRAC Final Project Report, GAP 017.* Pretoria: Department of Minerals and Energy.

**Mendecki, A. J. and van Aswegen, G. 1996, 1997.** Mine layout, geological features and seismic hazard. *SIMRAC Annual Report, GAP303.* Pretoria: Department of Minerals and Energy.

**Mendecki, A.J., van Aswegen, G. and Mountfort, P. 1999.** A Guide to Routine Seismic Monitoring in Mines. In: Ryder, J. and Jager, A. (Eds), A Handbook on Rock Engineering Practice for Tabular Hard Rock Mines, Creda Press, on behalf of SIMRAC (Safety in Mines Advisory Committee to the Department of Minerals and Energy of South Africa), Johannesburg, South Africa.

**Mendecki, A. J. and van Aswegen, G. 1996, 1997, 1998.** Mine layout, geological features and seismic hazard. *SIMRAC Mid-year Report, GAP303.* Pretoria: Department of Minerals and Energy.

**Mendecki A.J. and van Aswegen, G. 1998.** System stiffness and seismic characteristics – a case study. Abstracts of: International Workshop on Frontiers in Monitoring Science and Technology for Earthquake Environments, Tono Geoscience Centre, Toki and Kamioka, Japan, November 16-19, 1998.

**Milev, A. M., Spottiswoode, S. M. and Noble, K. R. 1995.** Mine induced seismicity at East Rand Property Mines. *Int. J. Rock Mech. Min. Sci. Abstr.* 32, p629-632.

**Ouillon, G. and Sornette, D. 1996.** Unbiased multifractal analysis: application to fault patterns. *Geoph. Res. Lett.*, vol. 23, no.23, p. 3409 - 3412.

- Pelletier, J.D., Malamud, B.D., Blodgett, T. and Turcotte, D.L. 1997.** Scale-invariance of soil moisture variability and its implications for the frequency-size distribution of landslides. *Engineering Geology*, vol. 48, no. 3-4, p. 255 - 268.
- Radu, S. and Mendecki, A.J. 1997.** Localisation measures for interactive seismic activity. (*In: Gibowicz, S. J. and Lasocki, S. Proceedings of 4<sup>th</sup> International Symposium on Rockbursts and Seismicity in Mines. Krakow, Poland, 11-14 August 1997.* Rotterdam: A. A. Balkema, p 197-200).
- Rice, J.R. 1984.** Shear instability in relation to the constitutive description of fault slip. *Proceedings of the 1<sup>st</sup> International Congress on Rockbursts and Seismicity in Mines. Johannesburg 1982.* N.C. Gay and E.H. Wainwright (eds.), pp. 57-62.
- Savage, J. C. 1994.** Empirical earthquake probabilities from observed recurrence intervals. *Bulletin - Seismological Society of America*, 84, 1, 219-221.
- Schreiber, T. and Richter, M. 1998.** Nonlinear projective filtering in a data stream. *Wuppertal preprint*.
- Spudich, P. and Frazer, L. N. 1984.** Use of ray theory to calculate high-frequency radiation from earthquake sources having spatially variable rupture velocity and stress drop. *Bulletin of the Seismological Society of America*, 74, pp.2061-2082.
- Van Aswegen, G. and Butler, A.G. 1993.** Application of quantitative seismology in SA gold mines. (*In Young P (Ed): Rockbursts and seismicity in mines.* Rotterdam: Balkema.)
- Van Aswegen, G. and Meijer, O. 1994.** The mechanisms of events around faults. 605-603. *Eurock 94: Rock Mechanics in Petroleum Engineering.* Rotterdam: Balkema, 972pp.
- Van Aswegen, G., Mendecki, A. J. & Funk, C. 1997.** Application of quantitative seismology in mines. (*In: Mendecki, A.J. Seismic Monitoring in Mines.* London: Chapman and Hall, p. 220-245)
- Van Aswegen, G. 1997.** Aspects of the seismic response to shaft pillar mining – case studies in the Welkom Gold Fields. *Proceedings of Shaft Pillar Extraction Seminar, Association of Mine Managers of South Africa.* Nov 1997.
- Van Aswegen, G. and Mendecki, A.J. 1998.** Mine layout, geological structures and seismic hazard – some new concepts. SIMRAC Symposium, Goldfields Training Centre, 24 November 1998. The South African Institute of Mining and Metallurgy, Johannesburg.
- Van Berkel, F. 1998.** Fractal Fault Population Analysis Program. 1998 version, with built-in help. Anglogold.
- Van der Heever P. K. and O'Connor, T. S. 1994.** The mining of a stressed deep-level shaft pillar. *XV th, 15<sup>th</sup> CMMI Congress.* Johannesburg: SAIMM. Vol. 1 p. 167-173.
- Walsh, J.J. and Watterson, J. 1987.** Distributions of cumulative displacement and seismic slip on a single normal fault surface. *J. Struct. Geol.*, vol. 9, no. 8, p. 1039-1046.
- Walsh, J.J. and Watterson, J. 1992.** Population of faults and fault displacements and their effects on estimates of fault-related extension. *J. Struct. Geol.*, vol. 14, no. 6, p. 701 - 712.

# Appendix

## Case study of a large seismic event at a South African gold mine Etude d'un événement sismique de grande envergure dans une mine d'or Sud Africaine Fallstudie eines Gebirgschlages in einer Suedafrikanischen Gold Mine

D. AMIDZIC, AngloGold – West Wits Operations, South Africa  
S.K. MURPHY, AngloGold – Western Deep Levels East Mine, South Africa  
G. van ASWEGEN, ISS International, South Africa

**ABSTRACT:** A seismic event of magnitude 4.0 occurred in Western Deep Levels East Mine on May 5, 1996. It caused extensive damage to the mining area. The event plotted below reef, at the intersection of the complex geology, ahead of actual mining. The mining area of interest is of great importance since the entire longwall is basically mining a large pillar caused by the extended mining of the mini-longwalls above and below. It will be shown that this seismic event changed the perception of the mining and rock engineering personnel concerning the negotiation of geological features and emphasized the importance of strict adherence to the recommended face configuration. All of this has resulted in a better understanding of the rock mass response to mining, support systems and an improved management of seismicity strategy.

**RÉSUMÉ:** Un incident sismique de magnitude 4.0 a eu lieu à Western Deep Levels le 5 Mai, 1996. Les dégâts étaient étendus dans la région minière. Le trace de l'événement a été fait sous la veine, à l'intersection de la "fault" zone, au-delà de l'exploitation. Cette région d'exploitation est de grande importance du fait que l'entiereté du "longwall" est en fait exploitée la plupart du temps cause par l'exploitation intensive des "mini-longwalls" dessus et dessous. Il sera démontré que cet incident sismique a changé la perception du personnel minier et des mécaniciens des roches concernant l'approche des caractéristiques. L'accent a aussi été mis sur l'importance d'adhérer strictement à la configuration de front recommandée. Tout ceci a abouti à une meilleure compréhension de la réaction des masses rocheuses à l'exploitation, les systèmes de support et une meilleure gestion de la stratégie sismique.

**ZUSAMMENFASSUNG:** Ein seismisches Beben der Stärke 4.0, ereignete sich in der WDL East Mine am 5. Mai 1996. Der Gebirgschlag verursachte erhebliche Schäden im Abbaubereich. Das Zentrum des Bebens lag vor der Abbaufrente, am Schnittpunkt der zweier Verschiebungszonen. Die betroffene Abbauzone ist von grosser Bedeutung, da die angrenzenden Vortriebe unter- und oberhalb in eine inselfoermige Lagerstaette vorstossen, die durch fruerehen intensiven Abbau verursacht wurde. Es wird gezeigt, wie das oben genannte Beben die Einschaeztung von Produktions- und Felsmechanikpersonal bezueglich des Vortriebes in geologisch gestoeerte Gebiete beeinflusste, und dass die strikte Einhaltung von Empfehlungen bezueglich Layout unbedingt notwendig ist. All dies fuehrte zu einem besseren Verstaendnis der Reaktion des Felsmasse zum Abbau, zu Stuetzmassnahmen und zu einer verbesserten Strategie zur Verhinderung von Gebirgschlaegen.

### 1 INTRODUCTION

Western Deep Levels, as one of the deepest gold mines in the world, is faced with a relatively high level of seismicity. The amelioration of the rockburst hazard is the single most important rock engineering task. In May 1996 a local magnitude 4 tremor occurred. There was no accident associated with the event, but it served as a catalyst for the development of new methods for the analysis of seismicity in mines and for a new stope support strategy.

Concepts and methods for the analysis of mining induced seismicity have developed rapidly over the past two decades since McGarr (1976) related seismic moment to the volume of elastic closure and Mendecki (1993,1997) brought mine seismology into the realms of rock mechanics and rheology. Some practical applications implemented in day to day operations in mines were described by Amidzic and Glazer (1995). Specific procedures for the analysis and interpretation of seismicity in South African gold mines are, however, by no means standardised. Methods described here may contribute in this regard.

In this paper we give an overview of the circumstances around – and nature of the large event. A back analysis of the seismicity around this event is used to explain a specific procedure to monitor the seismic rockmass response to the volume mined. We also show how the relation of radiated seismic energy to seismic moment can provide insight into system stiffness. We then describe the new stope support strategy for deep level tabular ore body mining, which has been successfully implemented for well over a year to date.

#### 1.2 Area of interest

Western Deep Levels (WDL) is approximately seventy kilometres southeast from Johannesburg at an elevation of about 1660m above sea level. WDL is part of the AngloGold West Wits operations and includes three mines: the East, South and West Mines. The area of the mine lease is approximately 45km<sup>2</sup>. The area is underlain by two tabular sub-parallel economic gold bearing reefs, the Ventersdorp Contact Reef (VCR) and the Carbon Leader Reef (CLR). The upper reef (VCR) lies between 1500m and 3000m below surface with the CLR approximately 900m deeper, both dip of approx. 21 degrees towards the south-southeast. WDL East Mine is currently mining the Carbon Leader Reef at depths between 2500m and 3700m below the surface.

#### 1.3 Mining method

The longwall mining method is used on WDL East Mine to mine the Carbon Leader Reef. With this method stoping on strike leads the development (follow-behind haulages), so that the latter can be protected from high stresses. This system however has three major drawbacks. 1) The absence of leading footwall and reef development precludes the accurate resolution of geological structures ahead of mining. 2) It is development intensive. 3) Off-reef (waste) mining is required in stopes when negotiating major faults or dykes which generally lie in a NE-SW direction.

#### 1.4 Mining history

The entire longwall C (area of interest – Figure 1) is basically mining a large pillar caused by the extended mining of the mini-longwalls above (A) and below (B). After a fire in 1987, the lower portion of the longwall C stood for approximately five years, while the lost production was made up by pushing the adjacent longwall, resulting in the creation of a highly stressed pillar – the area of interest here.

#### 1.5 Seismic system

The introduction of seismic monitoring networks in the early sixties yielded valuable insight into the origin and nature of seismic events and enabled more accurate estimates to be made of the energy content of these events. Seismic monitoring of the rock mass response to mining contributes to verifying mining layout design, to detecting potential instabilities and delineating new geology ahead of mining activity.

To improve the quality of the seismic database, a digital seismic network was installed in the early 90's. At present, twenty-three triaxial geophones are used to record seismic activity on the East Mine that covers an area of 16km<sup>2</sup>. A geophone records the velocity of ground motion due to transient seismic waves as an electrical signal. An analog to digital conversion (A/D) is performed on this output voltage and transmitted as time series data (seismograms) to the central site on surface. The processing software, which is built into the system, provides all the important physical parameters describing the seismic source: size, seismic moment, emitted energy, static and dynamic stress drops, as well as the parameters describing ground motions, maximum amplitude, energy, power and duration of strong ground motion. Currently, the East Mine seismic system is recording in excess of 1000 seismic events per day, in the local magnitude range of -2 to 4.

## 2 THE EVENT

### 2.1 Mining scenario

The area of interest was being extracted by two mini-longwalls (upper and lower) separated by a stabilising pillar. The complex geology in this area, where two fault systems strike 90 degrees to each other ahead of the two mini-longwalls, required that the Rock Engineering Department evaluate the most favourable face shape for each of the mini longwalls mining through these geological features. One of the problems encountered was that the best configuration for negotiating one of the structures was the worst for the other, due to the orientation of the fault systems to the longwalls (Butler, 1996).

By May 1996, the entire upper mini-longwall and a major portion of the mining faces in the lower mini-longwall were in a configuration practically parallel to the fault zone. The stress concentration ahead of the stope face thus coincided with the fault zone which greatly increased the potential for major seismic activity.

### 2.2 The seismic event

The seismic event that occurred in WDL East Mine on May 5, 1996 at 03h12 was recorded with 15 seismic stations and source parameters are as follows (Amidzic, 1996):

Local Magnitude	4.0
Moment (log) – (Nm)	13.9
Energy (log) – (J)	10.8
Stress Drop – (Mpa)	27
Source size - (m)	95

The location of the event was ahead of the lower mini-longwall C. The event was located some 70m below reef, at the intersection of the Break fault zone and another 0.6 m throw unnamed fault. The back analysis of seismic activity in the longwall shows clustering of the seismic events in the top abutment and along the Break fault zone one week before the major event. Subsequent increased seismic activity rates at the top abutment and the bottom pillar indicate load transfer to these respective areas.

Estimated source size of the seismic event is correlating well with the underground observations, where the event caused extensive damage to nine panels, over total length of 270m.

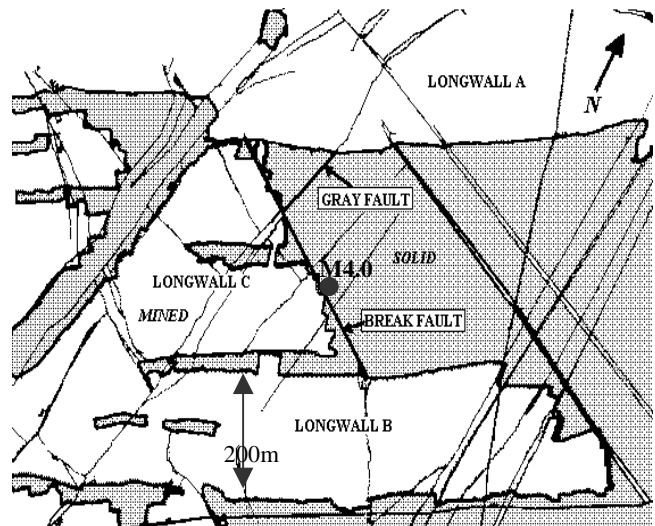


Figure 1. Mining plan of the area of interest (longwall C) with the geology and the location of the M4.0 event

## 3 BACK ANALYSIS WITH NEW CONCEPTS

### 3.1 The Seismic Response to Production

During 1996, an attempt was made on WDL East Shaft to investigate the relation between seismicity and production in order to improve the usage of seismic data, and to help access seismic hazard. The rock in the volume to be mined is under the action of the pre-existing (virgin) stresses prior its extraction. Once mining operations take place, local stress concentration adjacent to mine openings add to the already stored elastic strain energy in the rock mass. The total induced strain energy together with the strain energy due to tectonic forces provides the source of the energy released during a rockburst (Budavari 1983, Cook 1965). The amount of strain energy stored when mining elastic rock is directly proportional to the volume of elastic convergence  $V_e$  and:

$$\Sigma M = \gamma G \Delta V_e$$

where  $\Sigma M$  is the sum of seismic moment,  $G$  is rigidity and  $\gamma$  a factor between .3 and 1 (Milev et al., 1997; see also McGarr, 1976, for original work). This concept was used by van den Heefer and Connor (1994) for the planning of pillar mining. By monitoring the cumulative seismic moment and comparing it with numerical model prediction they could evaluate the potential of the system to yield a large event.

For a given mine layout a particular step in elastic convergence would be directly proportional to the volume mined in that step. Thus, although is impossible to directly measure the amount of energy entering the system due to mining, it is possible to

measure a parameter which would be directly proportional, i.e. the volume mined. The elastic strain energy released from the system in the form of seismicity is measured routinely with the seismic system. By normalising the seismic response to mining with the volume mined, we get a measure of the relation between the stored and the released energy. The seismic response to mining index (*SRP* – locally known as REP index, Amidzic and Murphy, 1997) is defined as

$$SRP = Ne * \frac{Va}{Vm}$$

where *Ne* is the number of events greater than a chosen cutoff magnitude, *Va* is the apparent volume of each event and *Vm* is the volume mined. We choose the cutoff magnitude such that those events responsible for 99% of the seismic energy released are taken into account (see Table 1). Apparent volume (Mendecki, 1997) is defined as moment divided by apparent stress (see below) and is considered a measure of the volume of coseismic, non-elastic deformation.

Table 1. Energy distribution per magnitude range.

Magnitude range	0 - 1	1 - 2	2 - 3	3 - 4
Energy released (GJ)	0.065	0.54	2.7	6.96
Percentage (%)	0.6	5.3	26.2	68.0

Over a given time a constant value of *SRP* would indicate a consistent release of energy, in keeping with the volume of elastic closure. A decrease from a constant value will indicate that more energy is stored than normal (generally undesirable). An increase would indicate that the system is starting to release energy at a faster rate than normal and that the system could become unstable. The following are example situations which could cause deviations from a regular trend:

- the approach of mining to a geological discontinuity
- a change to an unsuitable mining configuration
- a change in the effectiveness of regional support (backfill, stabilising pillars)
- unknown residual stress ('tectonic')

In general, one would expect a change in the general trend of *SRP* to reflect a change in system stiffness. On East Mine, prior to the major seismic event of M4.0, a high level of production in the area of interest was accompanied by the even higher level of the seismicity, induced by fault zone proximity, resulting in higher values for the *SRP* index (Figure 2).

After few months of low production, due to the extensive damage, a high level of production was achieved again, but now with the low level of induced seismicity (low *SRP* index). Mining away from the fault zone, but with improved rock engineering layout and stope support as well, has resulted in a significant reduction in the seismic hazard.

### 3.2 Seismic hazard and E-M parameters

As part of the back analysis, the seismic behaviour prior to the large event was quantified in terms of the standard seismic hazard parameters as well as some new parameters being researched in the S.A. gold mining industry. Details are described elsewhere (van Aswegen, 1997a, 1997b, Van Aswegen and Mendecki, 1998) but brief descriptions of the parameters are given below.

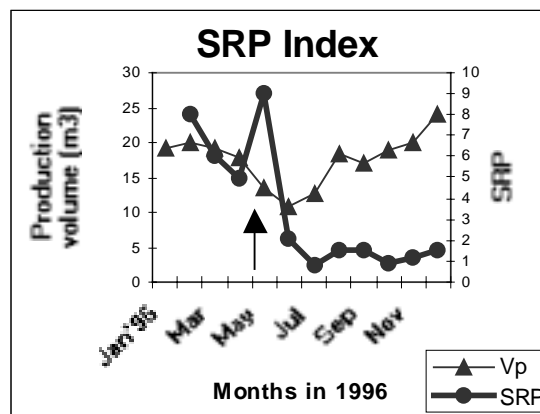


Figure 2. *SRP* Index and production volumes during 1996. The peak in *SRP* was caused by the large event (arrow) in May and the numerous aftershocks

Seismic hazard for a given area is defined as the probability of occurrence of a seismic event, equal to or exceeding a specified level, within a given period of time. Seismologists base the statistical estimation of probabilities on a model of the size distribution of tremors. According to the model (with numerous detail modifications), seismic event sizes follow a simple power law, called the Gutenberg-Richter relation:

$$\log N(\geq m) = a - bm,$$

where  $N(\geq m)$  is the expected number of events not smaller than magnitude  $m$ ,  $a$  and  $b$  are constant. The  $a$  value is the log of the number of events  $\geq$  magnitude 0.0. For fixed  $a$ , the number of larger events, i.e. the hazard, increase with a decrease in  $b$ . For a given data set, the  $a$  and  $b$  values then characterises the seismic hazard associated with the data.

On the S.A. mines, 'magnitude' is calculated from seismic moment  $M$  and radiated seismic energy  $E$ .

Another model describes the scaling relation between seismic moment and radiated seismic energy:

$$\text{Log} E = d \text{log} M + c$$

This is referred to as the E-M relation. The fact that  $d$  is generally greater than 1 is consistent with the observation that apparent stress

$$\sigma_A = GE/M \quad [\text{Pa}]$$

increases with magnitude. A magnitude independent indicator of the stress state at the seismic source is the energy index,  $EI$ , i.e. the ratio  $E$  of a given event to the typical  $E$  for the associated  $M$  derived from the local E-M relation. (Van Aswegen and Butler, 1993). For a given slope  $d$ , the constant  $c$  would indicate the level of stress (from all events in the data set) in the same way as the  $EI$  does for a single event. Therefore, apparent stress level is defined as

$$[\sigma_{AL}(c)]_{d,M \text{ constant}} = (G/M)10^{(c + d \text{log} M)}$$

It is a useful engineering parameter for the comparison of stress variation in space or time. By choosing the fixed  $M$  as the average for the data set,  $\sigma_{AL}$  would be equivalent to the average apparent stress. Intuitively it is easier to grasp the difference in stress level expressed in terms of say KPa. than in terms of a dimensionless constant  $c$  which varies around -10. The fixed  $d$  for purposes of calculating  $\sigma_{AL}$  is the average value over a given time or space span.

In quantitative seismology the seismic stress and seismic strain for a given volume  $\Delta V$  and over a given time  $\Delta t$  are defined as

$$\sigma_s = 2G\Sigma E / \Sigma M; \epsilon_s = \Sigma M / (2G\Delta V),$$

and the seismic stiffness modulus as

$$K_S = \sigma_s / \epsilon_s \text{ [Pa]}.$$

$K_S$  measures the ability of the system to resist seismic deformation with increasing stress (Mendecki et. al, 1999).

The slope ( $d$  value) of the E-M relation has been found to vary with the Gutenberg-Richter  $b$  value and the variation in both was interpreted as an indicator of system stiffness (Van Aswegen and Mendecki, 1998). The notion is thus that the  $d$  slope would decrease with system stiffness. Apparent stiffness is therefore defined as

$$K_{AS}(d,c) = G(E_2 - E_1)/(M_2 - M_1)$$

where  $E_2$  and  $E_1$  are the typical values of  $E$  for the two values of  $M$ ,  $M_2$  and  $M_1$ . As in the case of  $\sigma_{AL}$ , the units are Pa. For  $K_{AS}$  we choose a moment range  $M_2, M_1$  which spans the bulk of the data. Since  $K_{AS}$  then depends on both  $d$  and  $c$ , it should be more informative than quoting  $d$  only.

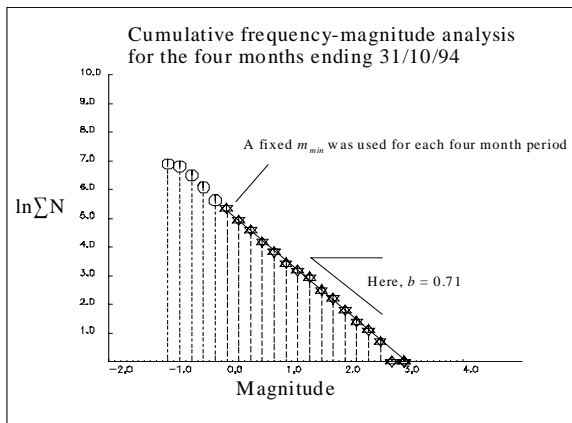


Figure 3. An example Gutenberg-Richter plot for one of the 27 four month time periods (forward stepping by one month) analysed.

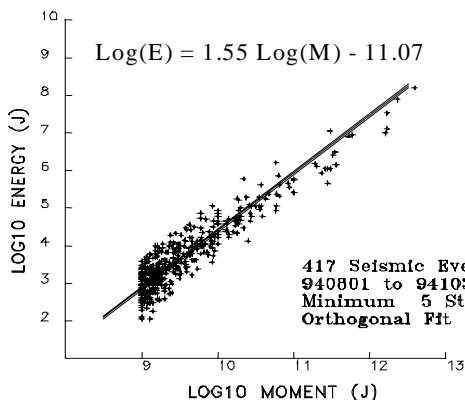


Figure 4. An E-M plot for the same dataset reflected in Fig. 3, except that all events  $< \log(M)9.0$  are filtered out – this was done for all the datasets analysed

The back analysis of the seismic data around the working place of interest here included the evaluation the Gutenberg-Richter  $a$  and  $b$  values for a four month moving time window starting in January 1994 up to the end of May 1996. The time window was stepped forward in one-month steps. For the calculation of the  $a$  and  $b$  values a simple procedure was followed: The value of  $m_{min}$  (minimum magnitude) was found through visual inspection of the cumulative frequency-magnitude histogram and  $b$  was then found through robust line fitting above  $m_{min}$  (Figure 3). For each of the selected time-subsets,  $d$  and  $c$  values of the E-M relation (Figure 4), the apparent stiffness and apparent stress level (for moment=10E10) were also calculated.

The variation of  $b$  and  $d$  over time is shown in Figure 5. A reasonable correlation between the  $b$ -value and the  $d$ -slope is evident. This is consistent with the conclusion (van Aswegen and Mendecki, 1998, Mendecki et al.,1999) that stiffer systems (higher  $d$ -slope) limit both the frequency and the magnitude of intermediate and large events.

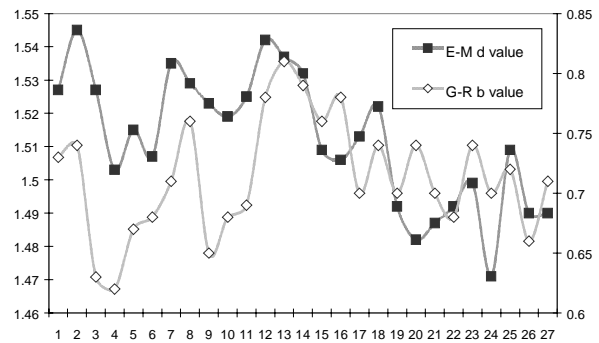


Figure 5. The variation of the Gutenberg-Richter  $b$  value and the E-M  $d$  value over the 27 months prior to the large event. The  $b$  value varies between 0.62 and 0.84 while the  $d$  value varies between 1.46 and 1.55.

The variation over time of apparent stress level and apparent stiffness is given in Figure 6. It is interesting to note that both these parameters show a steady decline over the last six months prior to the large event. The interpretation is that the system was softening due to progressive mining and resultant increase in mining span. The likelihood of a large event would be increased under such circumstances. Note that such an analysis is a far cry from temporal prediction. At best one could conclude that the potential for unstable deformation is increasing. It does show, in this case, that the system was loosing stability.

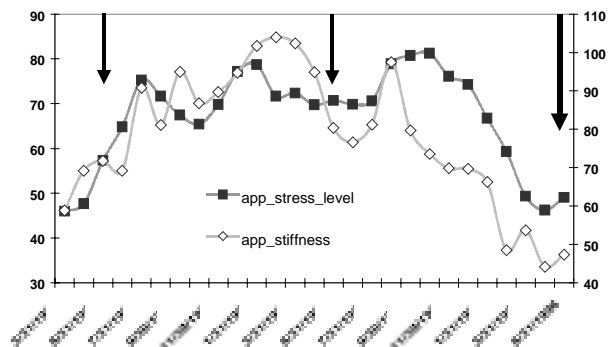


Figure 6. The variation of apparent stress level (30 to 90 KPa) and apparent stiffness (40 to 110 MPa) for the 27 months prior to the large event. The arrows indicate the occurrence of events larger than  $\log(E)10$ , the last arrow reflecting the occurrence of the main event of interest here.

This back analysis shows how traditional seismic hazard evaluation, combined with continuous evaluation of the E-M parameters, can be used to qualitatively evaluate the rockburst

#### 4 ROCK ENGINEERING ASPECTS

Following the analysis of this event, a major thrust was instituted to re-assess the current mining sequences and the validity of all the longwall-mining strategies at East Shaft. An important commitment was made by management to rectify all situations where non-adherence to the required mining strategies and face shape configurations was taking place.

In addition, during the back analysis of the rock engineering aspects of this event, it was found that the support systems that were in use at that time were inadequate in limiting the damage that result from this event.

##### 4.1 Change in seismic management strategy

The approach to seismic management on this shaft has been changed to include the SRP index in the mine design and planning process to provide pro-active information concerning the reaction of rockmass to the mining operations. This is accomplished by maintaining an intimate contact between the rock-engineering department, the mining department and other service departments on a day to day basis.

The SRP index, when used with an in depth knowledge of the area and sound rock engineering principles, has proven to be a reliable tool, which assists greatly with the monitoring and the design of mining strategies for individual mining areas.

##### 4.2 Change in support strategy

At the time of the major event, either a backfill/rapid yielding hydraulic props or a pack support system provided protection in the stoping panels. The pack support system was being used in areas where the geological features were being negotiated. This resulted in less than the planned 60% of the mined area being backfilled. During the seismic event 9 of the 11 panels in the longwall were damaged to the extent that access to some of the panels was only re-established after 6 weeks in certain cases.

Difficulties encountered were:- 1. Backfill being installed too far from the face with the RYH props support system and the fact that ground control problems were being experienced with this system. 2. The RYH props were susceptible to maintenance problems and the blast out rate of these props was high. 3. A pack support system was being used when bad ground conditions were intersected. It appears that the major failure that occurred during the event can be attributed to the above difficulties.

In a effort to increase the amount of backfill being installed, the rapid yield hydraulic prop and the pack support systems were replaced with a prestressed elongate/backfill support system as shown in Figure 7 which is now being used successfully at East Mine. (Amidzic and Murphy 1997)

It has been found that the integrity of the stope-hanging wall has improved due to the following:

- The prestressed elongates are not removed, which eliminates cyclic loading and unloading of the hanging wall, maintaining high areal coverage. This has been confirmed by FLAC. modeling. (Leach 1997).
- The maximum distance to the face of the backfill was reduced from 5.8m (R.Y.H. Prop system) to 4.5m effectively reducing the unsupported hanging wall beam.
- When these elongates are enclosed in backfill it's load carrying abilities increase and the yieldability of the elongate is enhanced. The hanging wall area where the

backfill support resistance is still too low is supported with these prestressed elongates.

- The prestressed elongates combined with backfill provides a much stiffer support than a pack support system.

Use of this support system has resulted in the percentage of the mined area backfilled increasing significantly since the introduction of this support system.

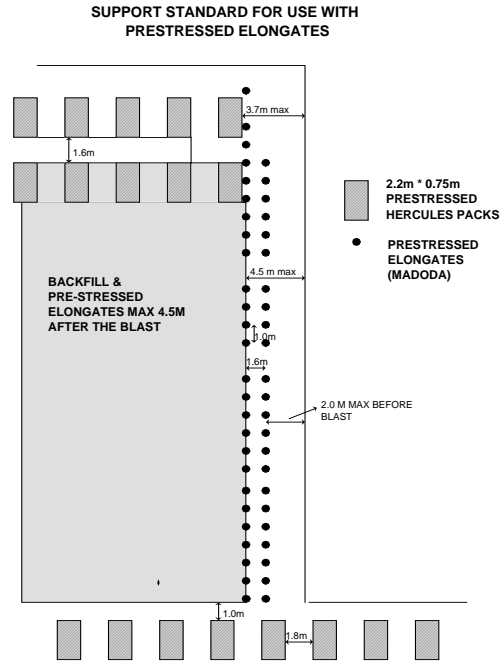


Figure 7. Prestressed elongate support system.

#### 5 DISCUSSION:

The back analysis, of this seismic event and the rock engineering aspects concerning the area where the event occurred, has provided valuable input in to the continued improvement of seismic management and support design at East Mine Western Deep Levels.

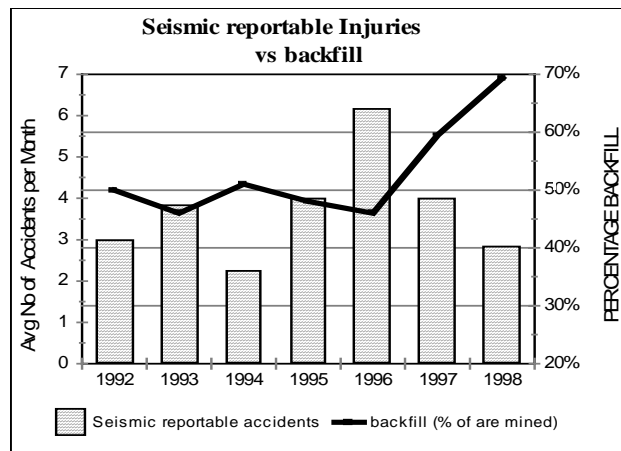


Figure 8. Seismic reportable injuries at East Mine and percentage of area filled vs. time.



In Figure 8, it can be seen that the increase in percentage of the mined area being backfilled, the introduction of elongates and the improvement in the seismic management strategy has resulted in a significant reduction in reportable accidents associated with seismic activity.

## 6 CONCLUSIONS

The occurrence of the major seismic event of M4.0 at WDL East Mine changed the overall approach to the management of seismicity at East Mine, resulting in increased safety and improved production. Specifically the monitoring of the seismic response to production (SRP) is already entrenched as a procedure for the assessment of the potential for unstable rockmass behaviour in the medium term. Together with apparent stress level ( $\sigma_{AL}$ ) and apparent stiffness ( $K_{AS}$ ) the methods for the analysis and interpretation of quantitative seismology have reached a new level of sophistication.

The introduction of a pre-stressed elongate/backfill support system has proven very successful in increasing the percentage backfill placed. This, in turn, improved the general conditions of the working places and minimised the effect of larger tremors, resulting in a proven lowering of the number of injuries to the work force.

## 7 ACKNOWLEDGMENTS

The authors would like to thank the management of AngloGold as well as the Safety in Mines Research Advisory Committee to the Department of Minerals and Energy of South Africa (SIMRAC) for permission to publish this paper.

## 8 REFERENCES

- Amidzic D, Glazer S.N. 1995. Space prediction of seismic events at Vaal Reefs Gold Mine, *SAGA Conference, Victoria Falls, Zimbabwe*.
- Amidzic D. 1996. Back analysis of the seismic event M4.0 on May 5, 1996. *Int. Report., AngloGold-West Wits Operations*.
- Amidzic D. and Murphy S.K. 1997. Evaluation and control of the seismic risk at Western Deep Levels Ltd.- East Mine. *SARES'97, 1<sup>st</sup> Southern African Rock Engineering Symposium*, Johannesburg, South Africa.
- Budavari, S. 1983. *Rock Mechanics in Mining Practice*. The South African Institute of Mining and Metallurgy, Johannesburg, Johannesburg.
- Butler, A.G. 1996. East Mine magnitude 4.0, *Int. Report, AngloGold – West Wits Operation*.
- Cook, N.G.W., Hoek, E., Pretorius, J.P.G, Ortlep, W.D. and Salamon, M.D.G. 1965. *Rock mechanics applied to the study of rockbursts*. SAIMM, Johannesburg
- McGarr, A., 1976. Seismic moments and volume change”, *J. Geoph. Res.*, 81, 1487-1494.
- Mendecki A.J., 1997. Quantitative Seismology and Rockmass Stability. In: Mendecki, A. J (Ed). *Seismic Monitoring in Mines*. Chapman & Hall, London, 1997, p178-219.
- Mendecki A.J., van Aswegen, G. and Mountfort, P. 1999. A Guide to Routine Seismic Monitoring in Mines. In: Ryder, J. and Jager, A. (Eds), *A Handbook on Rock Engineering Practice for Tabular Hard Rock Mines*, Creda Press, on behalf of SIMRAC (Safety in Mines Research Advisory Committee to the Department of Minerals and Energy of South Africa), Johannesburg, South Africa.

- Mendecki A.J., van Aswegen, G. 1998. System stiffness and seismic characteristics – a case study. *Abstracts of: International Workshop on Frontiers in Monitoring Science and Technology for Earthquake Environments*, Tono Geosience Centre, Toki and Kamioka, Japan, November 16-19, 1998.
- Leach, A.R. (1997), A comparison of hydraulic props with pre-stressed timber elongates when used as stope support. Report to AngloGold, Itasca Africa (Pty) Ltd.
- Milev, A.M., Spottiswoode, S.M. and Noble, K.R. (1995). Mine induced seismicity at East Rand Property Mines. *Int.J.Rock Mech.Min.Sci.Abstr.*, 32, 629-632
- van Aswegen, G. and Butler, A.G., 1993. Application of quantitative seismology in SA gold mines. In: Young(Ed): *Rockbursts and seismicity in mines*, 1993., Balkema, Rotterdam.
- van Aswegen .G., 1997a. Aspects of the seismic response to shaft pillar mining - can studies in the Welkom Gold Field. *Proceedings of Shaft Pillar Extraction Seminar, Association of Mine Managers of South Africa*. Nov. 1997.
- van Aswegen, G. and Mendecki, A.J. 1998. Mine layout, geological structures and seismic hazard – some new concepts. *SIMRAC Symposium, Goldfields Training Centre, 24 November 1998*. The South African Institute of Mining and Metallurgy, Johannesburg.
- van der Heever, P.K. and Connor, T.S. 1994. The mining of a stressed deep level shaft pillar, XVtn, 15<sup>th</sup> CMMA Congress, SAIMM, Johannesburg.